

RHODES UNIVERSITY
Where leaders learn

Exploring Intensity Mapping Techniques Via Simulations

Author:

Theophilus ANSAH-NARH

Supervisors:

Prof. Filipe B. ABDALLA

Prof. Oleg M. SMIRNOV

Dr. Khan M. B. ASAD

A thesis submitted in fulfillment of the requirements

for the degree of Doctor of Philosophy

in the

Centre for Radio Astronomy Techniques & Technologies
Department of Physics and Electronics

November 7, 2017

Declaration of Authorship

I, Theophilus ANSAH-NARH, declare that this thesis titled, “Exploring Intensity Mapping Techniques Via Simulations” and the work presented in it are my own. I confirm that:

- This work was done wholly or mainly while in candidature for a research degree at this University.
- Where any part of this thesis has previously been submitted for a degree or any other qualification at this University or any other institution, this has been clearly stated.
- Where I have consulted the published work of others, this is always clearly attributed.
- Where I have quoted from the work of others, the source is always given. With the exception of such quotations, this thesis is entirely my own work.
- I have acknowledged all main sources of help.
- Where the thesis is based on work done by myself jointly with others, I have made clear exactly what was done by others and what I have contributed myself.

Signed:

Date:

“Thanks to my solid academic training, today I can write hundreds of words on virtually any topic without possessing a shred of information, which is how I got a good job in journalism.”

Dave Barry

Abstract

Intensity mapping is a new observational technique which takes auto-correlations and low resolution images of the sky and attempts to map the distribution of large scale diffuse neutral hydrogen (HI) structure without actually localizing individual galaxies. This allows smaller and cheaper telescopes without long baselines such as KAT-7 to be used in such experiments, hence increasing the science output in tracing the Cosmic structure. The technique is however, limited by leakage due to gain errors and imperfect feeds which ultimately, contaminate the low frequency radio observation. Thus, the leakage cause a portion of the complex linear polarisation to find its way into Stokes *I* making it difficult to measure the overall intensity of the cosmological signal. The key focus of this paper, is to study the effects of the primary beam response in intensity mapping , as it modulates the intensity as a function of sky position. This has to be overcome in order to make such an experiment work to the best of its capabilities. To achieve this, we model the KAT-7 dish as a collection of dipoles and use that to produce fully polarised notional beams. We then corrupt them by introducing gain and phase errors and dipole orientation errors. We then observe what comes out of these simulations in terms of foregrounds that have leaked from intensity to polarisation. We also employ realistic beams of VLA in our simulations to measure the error we make when using notional beams. Our results show that, the amount of foregrounds that have leaked from intensity to polarisation is estimated at $\simeq 10^{-04}\%$ for using both notional beams of KAT-7 and holography measured beams of VLA. It is estimated at $\simeq 10^{-02}\%$ when we use the cassbeams of VLA. Therefore, the error we make in power spectrum estimation when we assume a notional beam whilst the foregrounds are actually convolved with cassbeams is $\simeq 0.0099\%$.

Acknowledgements

I would like to express my deepest appreciation for Stratos Idreos, who has guided and mentored me over the last one year on this project. His inspiration and feedback have been invaluable for carrying out the research. Without his persistent help this thesis would not have been possible. I would also like to thanks the members of the DASlab and especially Manos Athanassoulis and Abdul Wasay for their help. They have helped me tremendously with countless reviews and with the directions of the research. In addition, I would thank Chris Rycroft for helping me understand the randomized SVD and other numerical techniques through AM 205 lectures and the final project. Finally, I would thanks my family, classmates, and some very special friends who have made this journey to finishing this thesis possible. This thesis is the culmination of the efforts of many individuals to whom I owe my most sincere appreciation. First of all I would like to thank my supervisors: Dr. E. N. N. Nortey who doubles as the head of department and my main supervisor, especially for the passion he brings to everything he does and for his great knowledge in Mathematics and Statistics, and Dr. Kwabena Doku-Amponsah for his expertise in Probability and for the patience he had in advising me. Sincere gratitude is also extended to Dr. F. O. Mettle who is a member of the supervisory committee. I would like to thank everybody who was directly involved in the realization of this project, particularly to Mr. Ayirepaga Akogo, Miss Frimpongmaa Opoku Patricia, Mr. Christian Oko Niikoi, Miss Saviour Adams, Miss Patricia Agyepong, Miss Vivian Apetorgbor and Miss Agnes Nassie for helping me during the printing of questionnaires and data collection. Many individuals, even if in a less technical way, have been and are of vital importance for me throughout this research experience. My entire classmates deserve the best recognition. Gabby, Dennis, Willie, Pat, Lewis, Benedict, Baaba, Webster and the others have been wonderful companions throughout the study period, from 2011 - 2013. I would like to thank my family, Mr. Francis D. Narh (father), Mrs. Salome Nortey (mother), Samuel Annor Narh (brother), Esther Amatsu Narh and Christiana Koryoonmaatso Narh (sisters) for their love and trust. Without them this accomplishment would have been unachievable. We also acknowledge use of the HEALPix software (<http://healpix.sourceforge.net>) and FFP6 simulations generated using the Planck sky model <http://wiki.cosmos.esa.int/planckpla/index.php/> The authors gratefully acknowledge Lynn Baker, Mel Wright and David DeBoer for helpful discussions regarding the analysis

and interpretation of these data. We are grateful to Jeff Baars, Chris Fraley, Clifford F. Mass and J. McLean Sloughter for discussions and providing code and data.

Contents

Declaration of Authorship	i
Abstract	iii
Acknowledgements	iv
Contents	vi
List of Figures	x
List of Tables	xvi
List of Abbreviations	xvii
Physical Constants	xix
List of Symbols	xx
1 INTRODUCTION	1
1.1 The Origin of the Hydrogen 21-cm Line	1
1.2 HI Intensity Mapping	3
1.3 Significance of Intensity Mapping Techniques	5
1.4 Problem Identification	6
1.5 Research Objective	7
1.6 Delimitation	8
1.7 Rationale and Motivation	8
1.8 Thesis Outline	9
2 RADIO ANTENNAS AND SUPER-SYNTHESIS TECHNIQUE	11
2.1 Introduction	11

2.2	Antenna Parameters	13
2.2.1	Field Regions	13
2.2.2	Radiation Patterns	15
2.2.3	Beamwidth	16
2.2.4	Radiation Intensity	17
2.2.5	Radiation Patterns Types	17
2.2.6	Gain	18
2.3	EM Wave Polarisation	18
2.3.1	Derivation of the Stokes Polarisation Parameters	20
2.4	Antenna Arrays	23
2.4.1	Mathematical Formulation of Antenna Array	24
2.4.2	Beamforming	25
2.4.3	Types of Radio Arrays	26
2.4.3.1	Phased-Array Feeds	26
2.4.3.2	Transiting Arrays	27
2.4.3.3	Aperture Arrays	28
2.5	Super-Synthesis Technique	29
2.5.1	Construction of Radio Images	29
2.5.2	Correlator Super-synthesis Arrays	32
2.5.3	The Van Cittert-Zernike Equation	32
2.5.4	Filling the u,v Plane with Visibilities	35
3	FOREGROUND	39
3.1	Introduction	39
3.2	Galactic Foreground	40
3.2.1	Synchrotron	42
3.2.2	Free-free	45
3.2.3	Thermal dust	46
3.3	Component Separation Methods	48
3.3.1	Component Separation in the Pixel Domain	50
3.3.1.1	<i>Template Fitting</i>	50
3.3.1.2	<i>Internal Linear Combination</i>	51

3.3.1.3	<i>FastICA</i>	53
3.3.1.4	<i>Correlated Component Analysis</i>	53
4	INVESTIGATING INTENSITY MAPPING OBSERVATION WITH REALISTIC PRIMARY BEAM DISTORTION	55
4.1	Primary Beam Modelling	55
4.2	OSKAR Beam Model	57
4.2.1	Jones and Mueller matrices	62
4.2.1.1	Derivation of Mueller Matrix	65
4.2.2	Primary Beam Perturbation	69
4.3	Simulation	73
4.3.1	Full-sky Convolution	74
4.3.2	Angular Power Spectrum	76
4.4	Results and Analysis	79
4.5	Conclusions	86
5	EFFECTS OF HI INTENSITY MAPPING WITH MeerKAT	88
5.1	Introduction	88
5.2	Mathematical Basis of Zernike Moments	89
5.2.1	Orthonormality	92
5.3	Methodology	92
5.4	Results and Discussion	98
6	INVESTIGATING INTENSITY MAPPING EXPERIMENTS WITH SKA1-MID PRIMARY BEAMS	101
6.1	EM Simulations	101
7	CONCLUSIONS	103
Bibliography		104
A	OSKAR BEAMPATTERN AND FOREGROUND SIMULATIONS	119
A.1	Ray Tracing Technique	119
A.2	Modelled and measured beams	120
A.3	Measured Full-sky maps	121

A.4	Error Estimation in the Power Spectrum	123
B	Zernike Polynomials Model	124
B.1	Settings for OSKAR applications	125

List of Figures

1.1	<i>When the electron flips its spin, the atom emits a photon with a wavelength of 21-cm</i>	2
1.2	<i>The Properties of Electromagnetic Radiation</i>	3
1.3	<i>Simulated fluctuations in the brightness temperature of 21-cm emission from galaxies. Red indicates over-density and blue under-density.</i>	5
1.4	<i>Structure of the thesis</i>	9
2.1	<i>The different field regions of an antenna.</i>	14
2.2	<i>The different field regions of an antenna.</i>	15
2.3	<i>(a) Antenna pattern lobes in polar coordinates. (b) Antenna pattern lobes in linear power scale.</i>	16
2.4	<i>Graphical representation of antenna radiation properties. From left: shows the Isotropic patterns, middle: presents the Omni Directional Radiation Pattern and right: Directional pattern.</i>	17
2.5	<i>Relation of instantaneous electric-field vector E to polarisation ellipse</i>	18
2.6	<i>Wide gain in FoV enabled by PAFs. Right-centre: APERTIF installed at the focus of a WSRT telescope. Extreme right: PAFs installed on ASKAP (courtesy CSIRO).</i>	26
2.7	<i>Transiting Arrays:- PAPER (top-left), LWA (bottom-left), Medicina Northern Cross (top-right) and MWA (bottom-right).</i>	28
2.8	<i>Aperture Array:- LOFAR.</i>	29
2.9	<i>SKA-2 Dense Aperture Arrays precursor telescope.</i>	29
2.10	<i>(a) A distant radio astronomical source illuminates a dish antenna with parallel rays. (b) Electric field distributions of a source on the great sphere and antenna aperture on the aperture plane</i>	30

2.11	<i>The principle of super synthesis.</i> (a) <i>An interferometer rotates with the Earth rotation</i> (b) <i>Observing a radio source towards celestial North Pole.</i> (c) <i>Observing a radio source along the celestial equator.</i> (d) <i>Observing a radio source along a celestial latitude in between.</i>	31
2.12	<i>Geometry of a radio source and a simple interferometer.</i> (a) <i>An observed radio source with intensity distribution $I(l, m)$ using a simple two element radio interferometer.</i> (b) <i>Lower the elevation angle of the radio source the larger the value of w.</i>	33
2.13	<i>Locus on the u, v plane..</i> (a) <i>Locus of the ellipse on u, v plane for a baseline with $Z_\lambda \neq 0$ observing a radio source at declination δ_0.</i> (b) <i>Different declinations for different cases.</i>	36
2.14	<i>Filling the $u-v$ plane with visibilities.</i> (a) <i>The KAT-7 configuration.</i> (b) <i>The $u-v$ plane coverage of a 4h period of observation obtained from a source at the phase centre.</i>	37
2.15	<i>: 1.86 GHz KAT-7 radio contours of the A 550 cluster overlaid on the X-ray XMM-Newton images as an example of target that does not show any diffuse radio emission corresponding to the cluster centre. The image is not corrected by the primary beam. The vertical white bar indicates a 800kpc size..</i>	38
3.1	<i>Temperature distribution of the CMB on the sky as measured by the COBE satellite.</i>	41
3.2	<i>Different spectra of foreground emission components in the GHz range as measured by WMAP.</i>	42
3.3	<i>408 MHz Full-Sky Map.</i>	44
3.4	<i>A Full-Sky Hα Map.</i>	46
3.5	<i>Planck 857 GHz Full-Sky Map Tracing the Radiation from Thermal Dust.</i>	48
4.1	<i>(a) The “flat-top Gaussian” radial distribution of dipole positions, mimicking a realistic aperture illumination where the dipoles get less dense towards the edge of the dish and (b) the resulting 2D dipole distribution with a mask applied to mimic aperture blockage ensures effective illumination and avoids tapering off.</i>	60

4.2 Jones matrix representation of the KAT-7-like beams produced by OSKAR and shown at 1 GHz: (a) real part (b) imaginary part. The intensity of the imaginary parts increases with fewer dipoles and becomes very less when more dipoles are used.	61
4.3 Histogram plots of the imaginary components in Fig. 4.2 showing the distribution of inaccuracies on the KAT-7 dish-like surface.	62
4.4 Mueller matrix representations of full polarisation beams produced at 1 GHz	72
4.5 1000 MHz full-sky synchrotron maps simulated by using m -mode formalism. These synchrotron maps characterize the full-sky polarisation maps for our low resolution simulated observations and are presented here in the mollweide projection form defined by equatorial coordinates in terms of Stokes parameters I, Q, U and V	74
4.6 Convolved full-sky polarisation maps using the non-distorted OSKAR beams. For example, we used the m_{II} beam in Fig. 4.4a to convolve Stokes I in Fig. 4.5 and produce the convolved map $I \rightarrow I$, then we used m_{QI} beam to convolve Stokes Q to obtain the convolved map $Q \rightarrow I$, also, using the m_{UI} beam to convolve Stokes U we produced the convolved map $U \rightarrow I$. The other convolved maps are produced in the same manner using their respective beams.	78
4.7 Systematic errors of full-sky maps produced by computing the relative error between the absolute of the convolved true sky maps and the corrupted sky maps due to gain and phase error beams.	80
4.8 The top and middle maps depict the measured foregrounds of Stokes I, Q and U for using the non-distorted and the gain and phase error full polarisation beams respectively. The bottom maps are the corresponding errors in I, Q and U	80

4.9	<i>Convolved angular power spectra estimation of foreground maps.</i> First row: Shows Stokes I spectra plots for using simulated beams (Fig. 4.9a and 4.9b) and holography measured beams (Fig. 4.9c). Second row: Displays Stokes Q spectra plots for using simulated beams (Fig. 4.9d and 4.9e) and holography measured beams (Fig. 4.9f). Third row: Displays Stokes U spectra plots for using simulated beams (Fig. 4.9g and 4.9h) and holography measured beams (Fig. 4.9i).	82
4.10	<i>Comparing polarisation leakages when there is no beam correction with correcting the beam errors in Stokes I:</i> (a) Quantifies the amount of leakages into Stokes I which is caused by both measured (holography) and modelled (OSKAR) beams. The solid circular spectrum is the simulated 21-cm brightness temperature described by Alonso, Ferreira, and Santos (2014) at a $z \approx 0.67$. The solid thin spectrum ($ Q + iU _T$), is the leakage in I when the true modelled beams in Fig. 4.4a are used. The dashed spectra plots ($ Q + iU _{GP}$, $ Q + iU _{XY}$, $ Q + iU _{JVLA}$) are the leakages in I when we use modelled beams with gain, phase and dipole displacement and holography measured beams respectively. (b) These spectra plots show the estimate of the 21-cm signal when we correct for the errors in Stokes I beam.	83
4.11	<i>These are the spectra plots of the systematic errors in Fig. 4.7. The notations GP and XY in the legends denote the residuals for gain-phase and dipole orientation errors in the OSKAR beams, that of HB depicts the errors in the holography beams. These errors are then used to estimate the imperfections in the simulation by computing the expected value of the standard deviations of the sampling distributions of the residual maps to produce Table A.1.</i>	85
5.1	<i>Expansion of eight orthogonal radial polynomial $R_n^{ m }(\rho)$ plots. Here, the value of unity can be obtained at the outer edge, since $R_n^{ m }(1) = 1$.</i>	90
5.2	<i>Representation of basis patterns of Zernike moments $Z_n^m(\rho, \theta)$ of order 10, plotted on a unit circle.</i>	91
5.3	<i>Representation of basis patterns of Zernike moments $Z_n^m(\rho, \theta)$ of order 10, plotted on a unit circle.</i>	93

5.4	<i>Fully polarised distorted primary beams of KAT-7. (a) Due to gain and phase errors. (b) Due to dipole orientation errors.</i>	94
5.5	<i>Representation of basis patterns of Zernike moments $Z_n^m(\rho, \theta)$ of order 10, plotted on a unit circle.</i>	95
5.6	<i>Fully polarised distorted primary beams of KAT-7. (a) Due to gain and phase errors. (b) Due to dipole orientation errors.</i>	96
5.7	<i>Representation of basis patterns of Zernike moments $Z_n^m(\rho, \theta)$ of order 10, plotted on a unit circle.</i>	97
5.8	<i>Representation of basis patterns of Zernike moments $Z_n^m(\rho, \theta)$ of order 10, plotted on a unit circle.</i>	98
5.9	<i>Measured Stokes I, Q and U for using non-distorted and distorted dipole orientation error OSKAR beams with corresponding errors terms.</i>	99
5.10	<i>Measured Stokes I, Q and U for using non-distorted and distorted dipole orientation error OSKAR beams with corresponding errors terms.</i>	99
5.11	<i>Measured Stokes I, Q and U for using non-distorted and distorted dipole orientation error OSKAR beams with corresponding errors terms.</i>	100
A.1	<i>Fully polarised distorted primary beams of KAT-7. (a) Due to gain and phase errors. (b) Due to dipole orientation errors.</i>	120
A.2	<i>1 GHz holography measured Mueller beams of JVLA. (a) Antenna 5. (b) Antenna 6.</i>	121
A.3	<i>Convolved full-sky polarisation maps using the corrupted primary beams in Fig. A.1a. Here also, we used the m_{II} beam in Fig. A.1a to convolve Stokes I in Fig. 4.5 and produce the convolved map $I \rightarrow I$, then we used m_{QI} beam to convolve Stokes Q to obtain the convolved map $Q \rightarrow I$, also, using the m_{UI} beam to convolve Stokes U we produce the convolved map $U \rightarrow I$. The same approach is repeated to obtain (in row 2) $I \rightarrow Q$, $Q \rightarrow Q$, $Q \rightarrow U$ and (in row 3) $I \rightarrow U$, $Q \rightarrow U$, $U \rightarrow U$ by using the corresponding beams m_{IQ}, m_{QQ}, m_{UQ} and m_{IU}, m_{QU}, m_{UU}.</i>	122
A.4	<i>Measured Stokes I, Q and U for using non-distorted and distorted dipole orientation error OSKAR beams with corresponding errors terms.</i>	123

A.5 <i>Measured Stokes I, Q and U for holography measured beams of JVLA with corresponding errors terms.</i>	123
B.1 <i>Measured Stokes I, Q and U for using non-distorted and distorted dipole orientation error OSKAR beams with corresponding errors terms.</i>	125
B.2 <i>Measured Stokes I, Q and U for using non-distorted and distorted dipole orientation error OSKAR beams with corresponding errors terms.</i>	126
B.3 <i>Measured Stokes I, Q and U for using non-distorted and distorted dipole orientation error OSKAR beams with corresponding errors terms.</i>	127

List of Tables

2.1 Radio Frequency Bands	13
3.1 Measured Spectral Indices at Different Frequency Bands	43
5.1 Relationship between single and double index schemes to third order.	92
A.1 Error introduced in the power spectrum estimation	123

List of Abbreviations

2dF	2-degree-Field
6dF	6-degree-Field
AF	Array Factor
APERTIF	APERture Tile In Focus
ASKAP	Australian Square Kilometre Array Pathfinder
BINGO	Baryon acoustic oscillations In Neutral Gas Observations
BOSS	Baryon Oscillation Spectroscopic Survey
BSS	Blind Source Separation
CDF	Cumulative Distribution Function
CHIME	Canadian Hydrogen Intensity Mapping Experiment
CMB	Cosmic Microwave Background
COBE	COsmic Background Explorer
CSIRO	Commonwealth Scientific and Industrial Research Organization
DDA	Dense Aperture Array
DD	Direction Dependent
DI	Direction Indeependent
DGSE	Diffuse Galactic Synchrotron Emission
EM	ElectroMagnetic
EVLA	Expanded Very Large Array
FFT	Fast Fourier Transform
FAST	Five-hundred-meter Aperture Spherical Radio Telescope
FNBW	First Null Beam Width
FoV	Field-of-View
GBT	Green Bank Telescope
GMRT	Giant Metre wave Radio Telescope

GRASP	General Reflector Antenna Software Package
HBA	High-Band Antennas
HEALPix	Hierarchical Equal Area iso Latitude Pixelation
HIRAX	Hydrogen Intensity and Real-time Analysis eXperiment
HPBW	Half Power Beam Width
ICA	Independent Component Analysis
ILC	Internal Linear Combination
IEEE	Institute of Electrical and Electronics Engineers
IGM	InterGalactic Medium
IM	Intensity Mapping
ISM	InterStellar Medium
KAT	Karoo Array Telescope
LOFAR	LOw-Frequency ARray
NRAO	National Radio Astronomy Observatory
PAF	Phased-Array Feed
PAH	Polycyclic Aromatic Hydrocarbon
RF	Radio Frequency
RFI	Radio Frequency Interference
SDSS	Sloan Digital Sky Survey
SKA	Square Kilometre Array
SNR	Signal-to-Noise Ratio
VLA	Very Large Array
WMAP	Wilkinson Microwave Anisotropy Probe
WSRT	Westerbork Synthesis Radio Telescope

Physical Constants

Speed of Light $c_0 = 2.997\,924\,58 \times 10^8 \text{ m s}^{-1}$ (exact)

Constant Name *Symbol* = *ConstantValue* with units

List of Symbols

a distance m
 P power W (J s^{-1})

For/Dedicated to/To my...

Chapter 1

INTRODUCTION

Overview

This Chapter introduces us to the general background of the research by briefly discussing the “spin-flip” line of neutral hydrogen, with a rest wavelength of 21-cm and then moves on to discuss the significance of intensity mapping experiments. The research problems, key objectives, justification and the entire structure of the thesis are also outlined.

1.1 The Origin of the Hydrogen 21-cm Line

Despite the fact that space is very empty and there is a great distance between the stars in the Milky Way, the gap between these stars consists of dust and a very diffuse medium of gas of which astronomers refer to this baryonic as *interstellar medium* (ISM). This ISM is made up of neutral hydrogen gas (HI), molecular gas (also known as H₂), ionised gas (H_{II}) and dust grains (Duffy et al. 2012). A large portion of the mass of the ISM in the Milky Way is in the form of warm ($10^3 - 10^4$)K and cool (50 – 100)K atomic HI gas (Bolonkin 2017; Knee and Brunt 2001). The cold atomic HI gas can emit a particular wavelength of radio energy from a slight energy change in the hydrogen atoms (Landdeck et al. 2017). That is, the electron and proton spins of a hydrogen atom in the ground state may point either in the

same or opposite directions such that, the same spin state has slightly more energy than the oppose spin state. The energy difference (“ hyperfine splitting”) is 60 millionths of the energy between the ground state and the first excited state, making the state with the same spins unstable. When the hydrogen atom flips between the same-spin state to the anti-parallel state as shown in Fig. 1.1, it emits electromagnetic (EM) radiation with a frequency of approximately 142.406 MHz corresponding to a wavelength of 21-cm. This wavelength or frequency falls within the microwave radio region of the electromagnetic spectrum as displayed in Fig. 1.2 by (Miller 1998) and therefore, using large radio telescopes, radio astronomers can observe the 21-cm line even in a very distant spiral galaxies. Most often, when the observation is done, it’s line is not sharp. This is because, a spiral galaxy rotates in such a way that, if it is marginally edge-on to our line of sight, a portion of the HI regions move away from us whilst others move towards us. This *Doppler effect* broadens the 21-cm line into a double peak. It redshifts the radiation from the regions that move away from us and blueshifts the vice versa. When the rotation of the galaxy becomes faster, the line broadening also increases. Radio observations of the 21-cm line can measure the value of the rotational velocity of a spiral galaxy. In addition, the 21-cm emission line from HI is an extremely useful tool for studying gas in the ISM of external galaxies and tracing the large scale distribution of galaxies in the universe (López et al. 2017) since HI is detectable in most spiral galaxies and in some elliptical galaxies. An in-depth explanation to this section can be obtained from Burke and Graham-Smith (2009), Ciardi and Madau (2003), Madau, Meiksin, and Rees (1997), and Webb (1999).

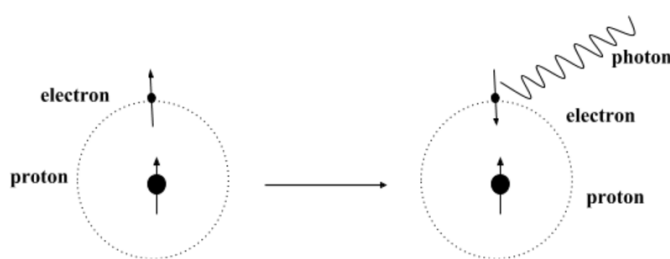


Figure 1.1: When the electron flips its spin, the atom emits a photon with a wavelength of 21-cm

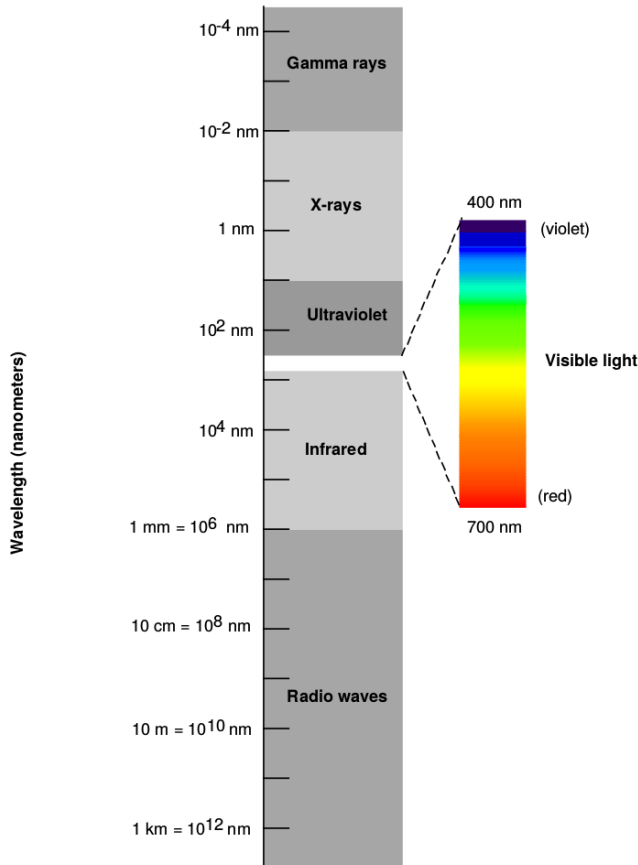


Figure 1.2: The Properties of Electromagnetic Radiation

1.2 HI Intensity Mapping

Over the past two decades, the galaxy redshift surveys use optical spectroscopy such as 2-degree-Field (2dF¹) (Cole et al. 2005; Colless et al. 2003), 6-degree-Field (6dF²) (Beutler et al. 2011), WiggleZ³ (Blake et al. 2011), Baryon Oscillation Spectroscopic Survey (BOSS⁴) (Anderson et al. 2012) and Sloan Digital Sky Survey (SDSS⁵) (Percival et al. 2010; Sadeh, Feng, and Lahav 2015) to specifically observe millions of individual galaxies, determine each redshift and use these to estimate the power spectrum for each (Peterson et al. 2009; Santiago et al. 1996; Santiago et al. 1995). An inference can therefore be made about the acoustic scale, by considering a simple biasing between the galaxy density field and that of the underlying matter density. As discussed extensively by Peterson et al. (2009) and Smoot and Debono (2017), using the 21-cm line of neutral hydrogen, a massive-scale structure of

¹<http://www.2dfgrs.net/>

²<http://www-wfau.roe.ac.uk/6dFGS/>

³<http://wigglez.swin.edu.au/site/>

⁴<http://www.sdss3.org/surveys/boss.php>

⁵<http://www.sdss.org/>

the Universe can be mapped in 3D to observe the full-sky across the redshift range from 0 to 5. This is achievable by studying specific intensity with resolution $\sim 10Mpc$ instead of the usual galaxy redshift survey. At high redshift, it normally requires very large collecting areas which is the main motivation to design the Square Kilometre Array (SKA) to perform this. Radio telescopes with apertures $\sim 100m$ have sufficient surface brightness sensitivity to detect HI at high redshift if they have a filled or close to filled aperture, but they will preferentially detect objects of angular size comparable to their resolution which will typically be clusters.

Meanwhile, the recent understanding of 21-cm *Intensity Mapping* (IM) (Camera et al. 2014; Chang et al. 2008; Santos et al. 2015b; Wolz et al. 2015; Wolz et al. 2014) in radio astronomy, is to use the full intensity field $T(f, \theta, \phi)$ in terms of frequency f and sky position (θ, ϕ) to measure the power spectrum directly, without actually localizing the individual galaxies. Thus, in IM experiment, the 21-cm emissions are considered as a diffuse source without attempting to detect individual objects as shown in Fig. 1.3. The average signal is expected to be $\sim 100\mu K$ on degree scales with the bandwidth of \sim few MHz (Battye et al. 2012), with order one fluctuation. This involves a meticulous subtraction of the continuum emission from our own Galaxy and extragalactic sources whereby, the continuum emission is expected to be spectrally smooth as compared to the 21-cm emission. Therefore, radio telescopes used in IM experiment require a resolution and sensitivity sufficient enough to measure the large scale structure and especially the Baryon Acoustic Oscillation (BAO) wavelengths. Section 1.3 briefly discusses the importance of IM observational techniques and some of the current radio instruments purposely designed to perform this kind of experiment.

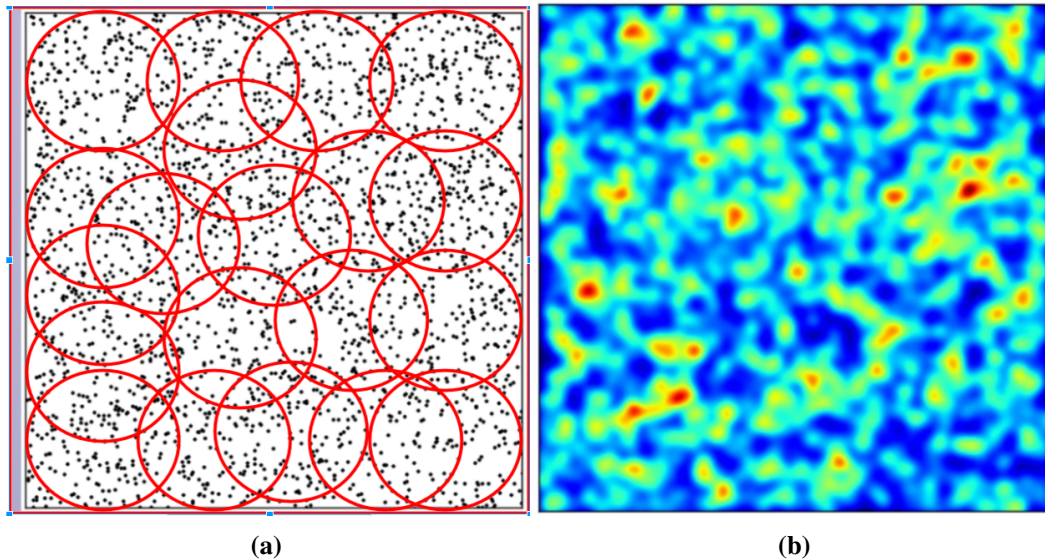


Figure 1.3: Simulated fluctuations in the brightness temperature of 21-cm emission from galaxies. Red indicates over-density and blue under-density.

1.3 Significance of Intensity Mapping Techniques

IM technique has the advantage of not resolving sources but instead measure all the intensity originating from a region and also, include radiation from faint sources and from the diffuse intergalactic medium (IGM) which at high redshifts could not be detected in other ways but whose contribution to the total signal is often important. These intensity maps also have the advantage of containing spatial information that can be used to further understand the processes of structure formation or as a cosmological probe since the fluctuations in the intensity of emission or absorption lines are correlated with underlying dark matter density fluctuations (Bass et al. 2009, p. 366). Also, with the observational data from several lines one will also be able to cross-correlate the lines which can be used to remove foreground from 21-cm observations. This is achievable since diverse emission lines will be observed at different frequencies and so will be contaminated mainly by uncorrelated line foregrounds. In addition, the technique allows smaller and cheaper telescopes without long baselines such as Karoo Array Telescope (KAT-7⁶), to be used in such experiments, hence increasing the science output in cosmology.

Presently, several IM experiments are in operation, such as the Green Bank Telescope (GBT⁷),

⁶<http://public.ska.ac.za/kat-7>

⁷<https://science.nrao.edu/facilities/gbt>

Baryon acoustic oscillations In Neutral Gas Observations (BINGO⁸) (Battye et al. 2012), Canadian Hydrogen Intensity Mapping Experiment (CHIME⁹) (Bandura et al. 2014; Newburgh et al. 2014), Tianlai¹⁰ (Chen 2012) and Five-Hundred-Meter Aperture Spherical Radio Telescope (FAST¹¹) (Nan et al. 2011). Among these instruments for IM experiments, the GBT produced the first HI signal at $z \sim 0.8$ and was cross-correlated with large-scale structure traced by galaxies in the WiggleZ dark energy survey (Masui et al. 2013; Contreras et al. 2013). Moreover, the capabilities of the next generation of radio telescopes such as dense aperture arrays for the Square Kilometre Array (SKA) and Hydrogen Intensity and Real-time Analysis eXperiment (HIRAX) make it only more promising, being the fact that, the technique is pretty cheap compared to usual galaxy surveys described in the first paragraph of section 1.1. Furthermore, these new instruments will provide a broader range of frequencies and a very massive survey area in order to produce HI intensity maps. IM experiments can be carried out at different redshifts either in auto-correlation mode, that is, single dish observations like BINGO (Battye et al. 2012) or interferometric mode like CHIME (Newburgh et al. 2014).

1.4 Problem Identification

Radio observations made with radio interferometers suffer from two main instrumental effects namely; Direction-Independent (DI) and Direction-Dependent (DD) effects. The complex instrumental gains in Fourier components due to the electronic devices that follow the antenna feeds are DI effects. These DI effects are easily calibrated and corrected separately from imaging. The DD effects are much more complicated, since they are applied during imaging and therefore, are transformed into a convolution of the measured components. This makes it very relevant to both calibrate the unknown DD effect and then correct the known or measured one. The ionospheric structure and the primary beam response of an altazimuthally mounted telescope are the common sources of DD effects as they are subject to mis-pointings and antenna structure deformation caused by the wind and gravitational load

⁸<http://www.bingotelescope.org/en/>

⁹<https://chime-experiment.ca/>

¹⁰<http://tianlai.bao.ac.cn/>

¹¹<http://fast.bao.ac.cn/en/>

on the dishes, differential heating, etc. These two time-varying terms go a long way to limit observations with the existing as well as the next generation of telescopes currently under construction. The challenges put forward by the ionosphere are especially stern at very low frequencies and with large interferometric arrays such as LOFAR¹² (van Haarlem et al. 2013; Wijnholds et al. 2010).

These challenges are also very crucial in IM experiment. For instance, using the IM technique requires the correct subtraction of the foreground continuum signal from our galaxy as well as extra-galactic sources, since the HI signal is weaker by several orders of magnitude than the astrophysical foreground signals (Yatawatta et al. 2013). Existing foreground subtraction techniques (Alonso et al. 2015; Gu et al. 2013) depend on the smoothness of this signal as a function of frequency. In the absence of instrumental corruptions, this assumption is perfectly valid. However, physical observations are affected by DD effects, that is, variations in gain amplitude and phase over the field-of-view (FoV), as well as polarisation leakage. In IM experiment, the primary beam in particular is a challenge, as it modulates the intensity as a function of the sky position, which is exactly what is being measured by this technique in the first place. In the case of KAT-7 and upcoming dish arrays, this will be dominated by pointing errors and polarisation leakages. Existing approaches to DD effects such as DD solutions (Smirnov 2011) are not directly applicable, since individual galaxies are not mapped out by this experiment. Hence, a different approach to map out DD effects in a stochastic sense, need to be developed.

1.5 Research Objective

The key focus of this project is to develop IM techniques for mapping out primary beams of a radio telescope and then, introduce realistic errors to perturb these modelled beams. We then attempt a correction and calibration of these distorted modelled beams and ultimately, use the final data for intensity mapping experiments. Thus, we simulate these modelled beams with full-sky polarisation maps and then, determine the amount of foregrounds that have corrupted the total intensity due to polarisation leakage and errors in the primary beams which have

¹²<http://www.lofar.org/>

not been accounted for. The study used Oxford’s Square Kilometre Array Radio-telescope (OSKAR¹³), a notional beamforming simulator, specifically developed to generate simulated data from large aperture arrays, such as those envisaged for phase I of the SKA to simulate the notional beams of KAT-7. The next beams produced for this study are Zernike models reconstructed from MeerKAT¹⁴ holography measured beams. The last primary beams used in this research are obtained from the Generalized Reflector Antenna farm analysis Software Package (GRASP¹⁵) of electromagneTIC RAdiation (TICRA) software.

1.6 Delimitation

The study main scope is to quantify two effects:

- (i) the contribution of polarisation leakage to the measured HI power spectrum, given some more or less realistic primary beams and
- (ii) the uncertainty on the estimate of (i) introduced by unmodelled differences in the primary beam.

1.7 Rationale and Motivation

Normally, antenna feeds measure the components of a signal along two orthogonal polarization states by two separate feeds. The signals from the two feeds travel through essentially independent paths till the correlator. However, due to mechanical imperfections in the feed or imperfections in the electronics, the two signals can leak into each other at various points in the signal chain. When a portion of the two signals leak into each other, it is referred to as the *polarisation leakage*. In terms of Stokes parameters, this produces an unwanted transfer of a signal between the Stokes I and QUV measurements. It is a particular problem for IM observations because polarised foreground signals are generally not smooth as a function of frequency due to Faraday rotation of the QU vector (Asad et al. 2015). Leakage, therefore, results in a non-smooth foreground component being introduced into Stokes I , one which

¹³<http://www.oerc.ox.ac.uk/ska/oskar2/>

¹⁴<http://www.ska.ac.za/gallery/meerkat/>

¹⁵<http://www.ticra.com/products/software/grasp>

is not amenable to traditional foreground subtraction techniques. Correcting for leakage is a challenge since it varies both as a function of time and frequency, hence, it is expected to limit observations with the existing as well as upcoming radio telescopes presently under construction (Bhatnagar et al. 2008). The study is motivated by this and therefore, concentrates rather on the effects of the primary beam particularly, DD polarisation leakage. The potential of IM has already been demonstrated by (Wolz et al. 2015; Chang et al. 2008; Wolz et al. 2014; Loeb and Wyithe 2008; Santos et al. 2015b) and the capabilities of upcoming telescopes as mentioned in section 1.3 make it only more promising. However, considerable research into this technique is necessary since, there are some sort of technical challenges in terms of data analysis and in particular measuring the primary beam response, which has to be overcome in order to make such an experiment work to its full potential.

1.8 Thesis Outline

The thesis is divided into seven different chapters as depicted in Fig. 1.4.

Chapter 1 briefly introduces the research topic by commencing with the general background of 21-cm emission line and continues by presenting the significance of IM experiment and clearly stating the research problem and objective. This chapter also justifies why the study is conducted and briefly explains how the simulations are done to produce the primary beams for various antenna types.

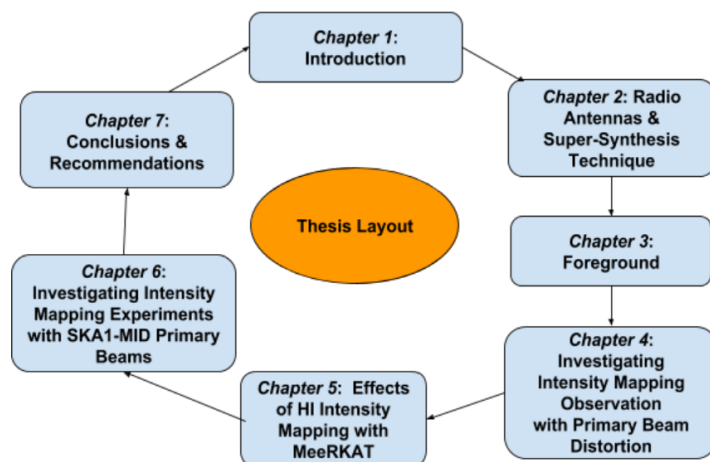


Figure 1.4: Structure of the thesis

The Chapter 2 discusses about radio telescope antennas where we clearly look at the numerous designs, operations and performances of antennas. Beamforming and radio array types are reviewed in this chapter. Also, we discuss a special technique known as super-synthesis, whereby we combine radio antennas as well as the Earth rotation to improve the u, v plane coverage for construction of radio images. The cheapest super-synthesis telescope is formed by 2 antenna elements. In one direction, the baseline varies through the movement of one antenna and in the other direction, the baseline vary through the Earth's rotation.

The foreground is discussed in Chapter 3. Here, the study mainly focused on galactic foregrounds and some foreground separation techniques.

Chapter 4 presents the first methodology employed in this research. In this chapter, we describe extensively the observational effects of primary beam perturbation of KAT-7, using the OSKAR software package. We then go ahead to determine the polarisation leakage by introducing the convolution technique to simulate the foregrounds. The study moves on further to compare the power spectrum of the simulated beams with the Jansky Very Large Array (JVLA¹⁶) holography measured beams.

The Chapter 5 describes the second methodology of this study. In this chapter, we produce modelled beams by fitting Zernike polynomials on MeerKAT measured beams to compute the reconstructed beams with less coefficients. These modelled beams are then used to simulate the foregrounds to estimate the effect on IM.

The third methodology in this work is presented in Chapter 6, where we generate GRASP simulated beams of SKA1-MID and then, also use that to measure the effect of IM.

The conclusions and recommendations are discussed in Chapter 7.

¹⁶<https://science.nrao.edu/facilities/vla>

Chapter 2

RADIO ANTENNAS AND SUPER-SYNTHESIS TECHNIQUE

Overview

Chapter Two introduces us to the general antenna parameters that are significant to describe the operation and performance of an antenna. A further discussion is made on how to mathematically derive the Stokes parameters from wave propagation. Beamforming and types of radio arrays are also discussed in this chapter. Finally, we give a brief description on super-synthesis technique for constructing radio images.

2.1 Introduction

The physical laws governing all classical EM phenomena are the famous Maxwell's equations:

$$\left\{ \begin{array}{l} \nabla \times \boldsymbol{\varepsilon}(\mathbf{r}, t) = -\frac{\partial}{\partial t} \mathbf{B}(\mathbf{r}, t) - \mathbf{M}(\mathbf{r}, t) \\ \nabla \times \mathbf{H}(\mathbf{r}, t) = \frac{\partial}{\partial t} \mathbf{D}(\mathbf{r}, t) + \mathbf{J}(\mathbf{r}, t) \end{array} \right. \quad (2.1)$$

where,

- $\boldsymbol{\varepsilon}(\mathbf{r}, t)$ electric field V/m ,
- $\mathbf{H}(\mathbf{r}, t)$ magnetic field A/m ,
- $\mathbf{D}(\mathbf{r}, t)$ electric induction C/m^2 ,
- $\mathbf{B}(\mathbf{r}, t)$ magnetic induction Wb/m^2 ,
- $\mathbf{J}(\mathbf{r}, t)$ electric current density (source) A/m^2 ,
- $\mathbf{M}(\mathbf{r}, t)$ magnetic current density (source) V/m^2 .

The mathematical model in equation 2.1 provides a complete description of the way electric and magnetic fields are generated and altered by each other, as well as by charges and currents. The electric and magnetic fields are represented as position vectors, in terms of amplitude and phase. The fields $\boldsymbol{\varepsilon}$ and \mathbf{H} vary in magnitude and orientation depending on both the position \mathbf{r} and time t , at which they are measured. The operator ∇ denotes the presence of some type of rotation in the variables of the equation. In effect, the change of $\boldsymbol{\varepsilon}$ and \mathbf{H} fields over time are equivalent to the change in the direction of the \mathbf{B} and \mathbf{D} fields respectively as EM waves move forward in space. These EM waves propagate at the speed of light and in an outward direction with respect to their origin. This phenomenon is termed as *EM Radiation* and obviously, in order to produce EM radiation, we must introduce a device capable of holding an alternating electric current. This device is known as an *antenna*. An antenna is therefore, defined as an electrical device designed to radiate or receive EM waves.

In radio astronomy, the antenna of a radio telescope operates in reception mode such that, a radio wave incident upon the antenna induces an electric current on its input terminals which can then be converted back into a radio frequency (RF) signal. This RF can be observed with a radio telescope at different ranges called *bands* as presented in Table 2.1 according

Table 2.1: Radio Frequency Bands

Band	Range of Wavelength (cm)	Frequency (GHz)
L	30 – 15	1 – 2
S	15 – 7.50	2 – 4
C	7.5 – 3.75	4 – 8
X	3.75 – 2.50	8 – 12
Ku	2.50 – 1.67	12 – 18

to Institute of Electrical and Electronics Engineers (IEEE) standard. The KAT-7 can observe L-band frequency which is very good for IM experiments.

2.2 Antenna Parameters

The numerous designs of an antenna make it necessary to describe the performance of an antenna. This of course, requires a clear understanding of the parameters of an antenna. This section therefore discusses the antenna parameters:

2.2.1 Field Regions

The EM fields of an antenna display different patterns depending on the space surrounding the antenna at which they are measured. This surrounding space can be classified into three regions as depicted in Fig. 2.1 (see Balanis 2005, p. 34):

- *Reactive near-field*: This is the closest region of the antenna. The energy in this region oscillates towards and away from the antenna, making it purely reactive and completely storing the energy. This makes both the electric and magnetic fields out of phase. The outer boundary for this region is at a distance $R < 0.62\sqrt{\frac{D^3}{\lambda}}$ where, R is the distance from the antenna surface, D is the largest dimension of the antenna and λ is the wavelength in metres. The frequency of the EM waves is related to the wavelength such that, $\lambda = \frac{c}{f}$ where, $c = 2.99792458 \times 10^8 \text{ m/s}$ is the speed of light and f is the frequency in Hz .
- *Radiating near-field*(also known as *Fresnel* region): This region lies between the reactive near-field and the far-field. The field strength in this region is lesser as compared to the reactive near-field. Thus, as the surrounding space from the antenna increases,

the EM fields become less reactive, making part of the energy to be converted into radiation. Also, the angular field distribution in this region is a function of the distance from the antenna and hence, the outer boundary is at a distance $R < 0.62 \frac{D^2}{\lambda}$.

- *Far-field* (also known as *Fraunhofer* region): This region exists at a distance $R > 2 \frac{D^2}{\lambda}$. The reactive fields are no longer present and only the radiation fields exist. Also, the electric and magnetic fields in this region are perpendicular and in-phase. The ratio between their magnitudes are constant. Furthermore, the general radiation pattern in this region remains the same regardless of the distance from the antenna.

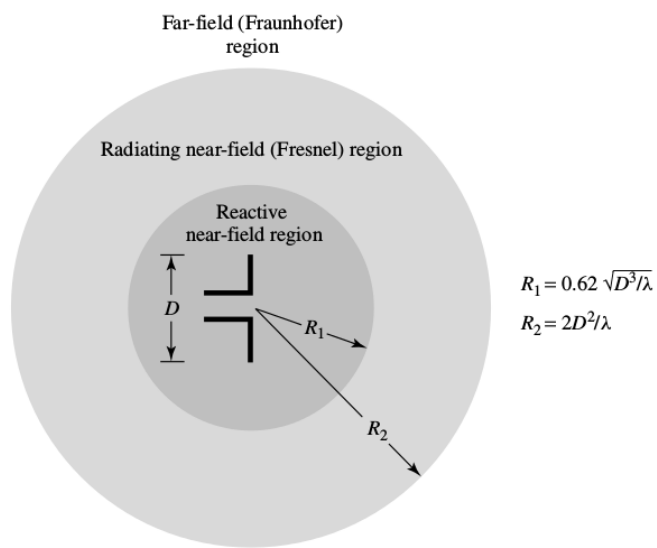


Figure 2.1: The different field regions of an antenna.

As the observation distance changes from near to far fields, the radiation pattern of an antenna also changes in shape in terms of amplitude and phase due to the variations of the fields.

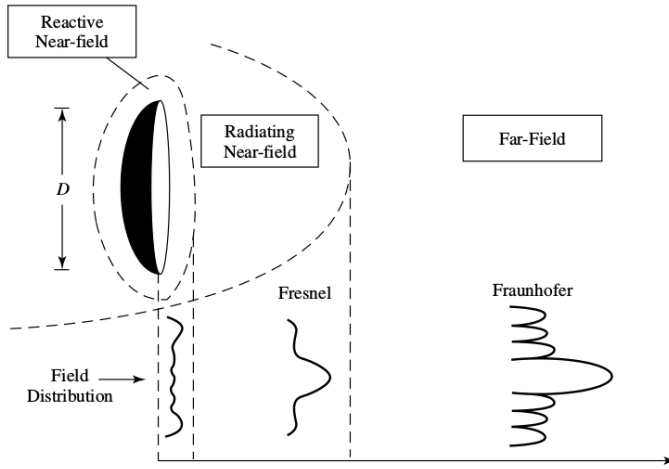


Figure 2.2: The different field regions of an antenna.

In Fig. 2.2 (see Balanis 2005, p. 35), the radiation pattern is almost uniformly distributed in the reactive near-field region. As the observation is gradually moved towards the radiating near-field, the radiation pattern begins to smooth and form lobes. The radiation pattern is fully formed at the far-field with minor and major lobes.

In radio astronomy, the antenna of a radio telescope operates in the far-field of the feed system to produce the desired illumination of the antenna.

2.2.2 Radiation Patterns

The antenna *pattern* is measured at the far-field region since there is no cause of change in the pattern when there is an increase in the distance. It describes the response of an antenna as a function of direction and generally comprises of a number of lobes as displayed in Fig. 2.3 (see Kraus 1966, p. 153). The lobes are briefly discussed as follows:

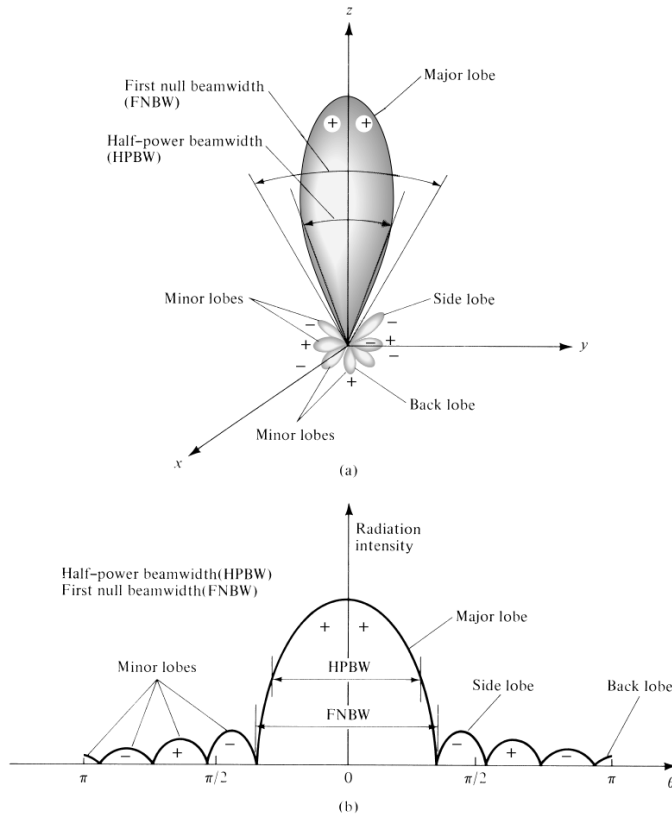


Figure 2.3: (a) Antenna pattern lobes in polar coordinates. (b) Antenna pattern lobes in linear power scale.

- The *major lobe* or the *main beam* contains the direction of maximum radiation. It is actually the region where the radiated power is most intense.
- Radiation from undesired direction is termed *minor lobe*. The highest minor lobe is referred to as the *side lobe* which is often adjacent to the main lobe as illustrated in Fig. 2.3. The minor lobe containing the direction opposite to that of the main beam is referred to as the *back lobe*.

2.2.3 Beamwidth

The angular distance between two identical points on opposite side of the pattern maximum is termed *beamwidth* of a pattern. The beamwidth is mostly presented in two ways:

- *Half Power Beam Width (HPBW)*: This is the angular difference between the points where the radiation intensity reaches half of its maximal value as shown in Fig. 2.3.
- *First Null Beam Width (FNBW)*: This is the angular difference between the two nulls enclosing the main lobe also presented in Fig. 2.3.

2.2.4 Radiation Intensity

The intensity of radiation is very dominant at the far-field region. It is mathematically expressed in terms of the far-zone electric field of an antenna:

$$U(\theta, \phi) = \frac{r^2}{2\eta} |\mathbf{E}(r, \theta, \phi)|^2 \quad (2.2)$$

where, U = radiation intensity (W/unit solid angle), $\mathbf{E}(r, \theta, \phi)$ = far-zone electric-field intensity of the antenna, r = radial electric-field component. The elevation angle θ describes the antenna tilt relative to the horizon while the azimuth angle ϕ describes the antenna traverse in a zero tilt state.

2.2.5 Radiation Patterns Types

There are three main categories of radiation patterns (see Fig. 2.4) namely:

- *Isotropic Radiation Pattern*: This results in constant pattern (spherical radiation pattern) in both azimuth and elevation planes. This hypothetical isotropic pattern is used as a reference to calculate antenna gain.
- *Omni Directional Radiation Pattern*: This pattern results in a uniform main beam at a particular plane and a constant decreasing pattern in the other. Thus, the pattern is 'dough-nut' in shape.
- *Directional Radiation Pattern*: This pattern contains one clear main beam in both azimuth and elevation planes.



Figure 2.4: Graphical representation of antenna radiation properties. From left: shows the Isotropic patterns, middle: presents the Omni Directional Radiation Pattern and right: Directional pattern.

2.2.6 Gain

The antenna gain G , is expressed as;

$$G = 4\pi \frac{U(\theta, \phi)}{P_{in}} \text{ (dimensionless)} \quad (2.3)$$

where, U = radiation intensity and P_{in} is the overall accepted power.

The antenna gain takes into account the antenna efficiency since it is a measure of how much power the antenna radiates in a certain direction, relative to how much power was incident upon the antenna.

2.3 EM Wave Polarisation

Consider a plane wave propagating in the positive z direction as in Fig. 2.5, with electric-field components in the x and y directions as given by

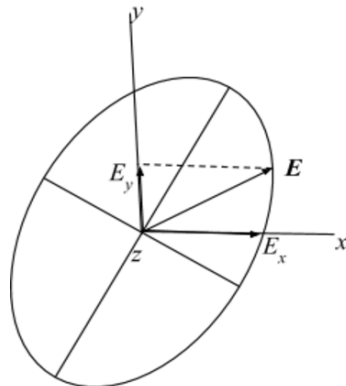


Figure 2.5: Relation of instantaneous electric-field vector \mathbf{E} to polarisation ellipse

$$E_x(z, t) = E_1 \cos\{\omega t - \beta z + \delta_x\} \quad (2.4a)$$

$$E_y(z, t) = E_2 \cos\{\omega t - \beta z + \delta_y\} \quad (2.4b)$$

where, the constant terms E_1 and E_2 characterize the maximum amplitude of x, y components respectively, $\omega = 2\pi\nu$ is the angular frequency, $\beta = 2\pi/\lambda$ is the measure of the ellipticity and δ_x, δ_y are phases of E_x and E_y respectively. Equations 2.4a and 2.4b characterize the two linearly polarised waves in the x and y directions respectively.

The resultant field is obtained by adding equations 2.4a to 2.4b vectorially:

$$\begin{aligned} \mathbf{E}(z, t) &= \hat{\mathbf{x}}E_x(z, t) + \hat{\mathbf{y}}E_y(z, t) \\ &= \hat{\mathbf{x}}E_1 \cos\{\omega t - \beta z + \delta_x\} + \hat{\mathbf{y}}E_2 \cos\{\omega t - \beta z + \delta_y\} \end{aligned} \quad (2.5)$$

where, $\hat{\mathbf{x}}, \hat{\mathbf{y}}$ = unit vectors in x and y directions. Therefore, at $z = 0$, equation 2.5 becomes;

$$\mathbf{E}(t) = \hat{\mathbf{x}}E_1 \cos\{\omega t + \delta_x\} + \hat{\mathbf{y}}E_2 \cos\{\omega t + \delta_y\} \quad (2.6)$$

As clearly presented in Kraus 1966, p. 109, by eliminating the time t in equation 2.6, we obtain the most general expression of an ellipse as;

$$aE_x^2 - bE_xE_y + cE_y^2 = 1 \quad (2.7)$$

where, $a = 1/E_1^2 \sin^2(\delta)$, $b = 2 \cos(\delta)/E_1E_2 \sin^2(\delta)$, $c = 1/E_2^2 \sin^2(\delta)$ and $\delta = \delta_y - \delta_x$.

Equation 2.7 shows that at any specific time t , the locus of points characterized by the propagation of E_x and E_y will trace out this curve. In equation 2.7, the product term E_xE_y actually shows a rotated ellipse. In general, the axes of the ellipse are not in x and y directions and therefore, the general case of elliptical polarisation as in Fig. 2.5 is presented in equation 2.5.

Obviously, from equation 2.5 if $E_1 = 0$, the wave is *linearly polarised* in the y direction and if $E_2 = 0$, the wave is linearly polarised in the x direction. If $\delta = 0$ and $E_1 = E_2$, the wave is linearly polarised at 45° with respect to the x axis. When $\delta = +90$ and $E_1 = E_2$, the wave is said to be *left circularly polarised* and when $\delta = -90$, it is known to be *right circularly polarised*.

2.3.1 Derivation of the Stokes Polarisation Parameters

In section 2.2, we dealt with fully polarised waves where, E_1, E_2 and δ are considered constants. A monochromatic (i.e. single-frequency) radiation is of this form. However, generally, in radio astronomy, the emission from celestial radio sources extends over wide frequency range and within any finite bandwidth $\Delta\nu$ consists of the superposition of a large number of statistically independent waves of a variety of polarisations. The resultant wave is said to be *randomly polarised*. In this section we consider a pair of plane waves that are orthogonal to each other at a point in space and choosing $z = 0$:

$$E_x(t) = E_1(t) \cos\{\omega t + \delta_x(t)\} \quad (2.8a)$$

$$E_y(t) = E_2(t) \cos\{\omega t + \delta_y(t)\} \quad (2.8b)$$

where, $E_1(t), E_2(t)$ are the instantaneous amplitudes, ω is the instantaneous angular frequency, $\delta_x(t), \delta_y(t)$ are the instantaneous phases of $E_x(t)$ and $E_y(t)$ respectively. The time variations of $E_1(t), E_2(t), \delta_x(t)$ and $\delta_y(t)$ are very slow compared to that of the mean frequency, ν ($\omega = 2\pi\nu$) which is of the order of the bandwidth $\Delta\nu$. Eliminating ωt term explicitly between equations 2.8a and 2.8b we get similar expression in equation 2.7:

$$\frac{E_x^2(t)}{E_1^2(t)} - 2\frac{E_x(t)E_y(t)}{E_1(t)E_2(t)} \cos \delta(t) + \frac{E_y^2(t)}{E_2^2(t)} = \sin^2 \delta(t) \quad (2.9)$$

where, $\delta(t) = \delta_y(t) - \delta_x(t)$. Equation 2.9 reduces into equation 2.7 when monochromatic radiation is considered, making E_x and E_y to be implicitly time dependent.

In order to measure the intensity of a radio wave, one takes the average per the time of observation . To do this, assume the time taken to be infinite because of a long period of time as relatively compared to the time for a single oscillation. The time average for equation 2.9 is therefore represented as;

$$\frac{\langle E_x^2(t) \rangle}{E_1^2} - 2\frac{\langle E_x(t)E_y(t) \rangle}{E_1E_2} \cos \delta + \frac{\langle E_y^2(t) \rangle}{E_2^2} = \sin^2 \delta \quad (2.10)$$

where, the symbol $\langle \rangle$ denotes the time average and

$$\langle E_i(t)E_j(t) \rangle = \lim_{T \rightarrow \infty} \int_0^T E_i(t)E_j(t)dt, \quad i, j = x, y \quad (2.11)$$

We multiply equation 2.10 by $4E_1^2E_2^2$ to get;

$$4E_2^2\langle E_x^2(t) \rangle - 8E_1E_2\langle E_x(t)E_y(t) \rangle \cos \delta + 4E_1^2\langle E_y^2(t) \rangle = (2E_1E_2 \sin \delta)^2 \quad (2.12)$$

and then use equation 4.26 to find the average values of equation 4.25 from equations 2.8a and 2.8b:

$$\langle E_x^2(t) \rangle = \frac{1}{2}E_1^2 \quad (2.13a)$$

$$\langle E_y^2(t) \rangle = \frac{1}{2}E_2^2 \quad (2.13b)$$

$$\langle E_x(t)E_y(t) \rangle = \frac{1}{2}E_1E_2 \cos \delta \quad (2.13c)$$

Substituting equations 2.13a, 2.13b and 2.13c into equation 4.26, we get;

$$2E_1^2E_2^2 - (2E_1E_2 \cos \delta)^2 + 2E_1^2E_2^2 = (2E_1E_2 \sin \delta)^2 \quad (2.14)$$

Representing equation 4.34 in perfect square form, we add and subtract $E_1^4 + E_2^4$ to get;

$$(E_1^2 + E_2^2)^2 - (2E_1E_2 \cos \delta)^2 - (E_1^2 - E_2^2)^2 = (2E_1E_2 \sin \delta)^2 \quad (2.15)$$

We can deduce the intensities from equation 4.35:

$$S_0 = E_1^2 + E_2^2 \quad (2.16a)$$

$$S_1 = E_1^2 - E_2^2 \quad (2.16b)$$

$$S_2 = 2E_1E_2 \cos \delta \quad (2.16c)$$

$$S_3 = 2E_1E_2 \sin \delta \quad (2.16d)$$

Equation 4.36 is then expressed as;

$$S_0^2 = S_1^2 + S_2^2 + S_3^2 \quad (2.17)$$

Equations 2.16a, 2.16b, 2.16c and 2.16d represent the Stokes polarisation parameters for a plane wave. These parameters are real quantities with S_0 being the total intensity. The parameter S_1 characterizes the linear horizontal or vertical polarisation, that of S_2 characterizes the amount of linear $\pm 45^\circ$ polarisation and S_3 represents the amount of right or left circular polarisation contained within the beam. These parameters can be used to determine the degree of polarisation P_{deg} , for a given state of polarisation:

$$P_{deg} = \frac{I_{pol}}{I_{tot}} = \frac{(S_1^2 + S_2^2 + S_3^2)^{1/2}}{S_0}, \quad 0 \leq P_{deg} \leq 1 \quad (2.18)$$

where, I_{pol} is the intensity of the sum of the polarization components and I_{tot} is the total intensity of the beam. $P_{deg} = 1$ relates to completely polarised light, $P_{deg} = 0$ relates to unpolarised light and $0 < P_{deg} < 1$ relates to partially polarised light.

The Stokes parameters can also be obtained by ignoring the time average approach and expressing equations 2.8a and 2.8b in terms of complex amplitudes:

$$E_x(t) = E_1 \exp\{i(\omega t + \delta_x)\} = E_x \exp\{i\omega t\} \quad (2.19a)$$

$$E_y(t) = E_2 \exp\{i(\omega t + \delta_y)\} = E_y \exp\{i\omega t\} \quad (2.19b)$$

where, $E_x = E_1 \exp\{i\delta_x\}$ and $E_y = E_2 \exp\{i\delta_y\}$ are the complex amplitudes. The Stokes polarisation parameters from these complex amplitudes are:

$$S_0 = E_x E_x^* + E_y E_y^* \quad (2.20a)$$

$$S_1 = E_x E_x^* - E_y E_y^* \quad (2.20b)$$

$$S_2 = E_x E_y^* + E_y E_x^* \quad (2.20c)$$

$$S_3 = i(E_x E_y^* - E_y E_x^*) \quad (2.20d)$$

Substituting equations 2.19a and 2.19b into equation 2.20, we reproduce the expression in equation 4.36.

The Stokes parameters give a full characterization of any polarisation state of a plane wave. In chapter four, we discuss further on how to formulate the Stokes parameters in terms of column matrix to obtain not only measurable intensities but also observables too.

For a more general discussion on wave polarisation see (Born and Wolf 1965; Kraus 1966; Wood 1988; Shurcliff 1962; Goldstein 2003).

In short, an EM wave received by an antenna consists of both electric and magnetic fields. If we are to track the curve traced by the tip of the electric field vector, in some fixed location in space, we will get, as time varies, a curve referred to as the polarization ellipse . Also, for a specified location we would generally get different curves, that is to say, the antenna polarization is dependent upon the direction of observation.

2.4 Antenna Arrays

An *antenna array* is a combination of 2 or more spatially separated antennas used to measure or direct the radiation intensity of a source towards a desired angular sector in order to have an improved performance over that of a single antenna. A very relevant characteristic of an array is that, the radiation pattern can be changed when we electronically steer or scan the antenna elements towards some other direction by changing their relative amplitudes and phases. This phenomenon does not occur when we use just a single antenna whose radiation pattern remain fixed. The use of an array for an observation gives us the opportunity to accept a particular desired array pattern without changing its physical dimensions. Furthermore, by manipulating the received signals from the individual antenna elements in different ways, we can achieve many signal processing functions such as spatial filtering (Armstrong, Zarb Adami, and Jones 2009; Leshem and van der Veen 2000; Wijnholds and van der Veen 2008), interference suppression (Ben-David and Leshem 2008; Levanda and Leshem 2010a; Mitchell and Robertson 2005), gain enhancement (Yatawatta 2008), target tracking (Woodburn et al. 2015; Duev et al. 2015), etc.

2.4.1 Mathematical Formulation of Antenna Array

Consider N antenna elements with corresponding $\bar{g}_k(\theta, \phi) |_{k=1,2,3,\dots,N}$ pattern of the k^{th} antenna. We take the elevation angle to vary over $-90^\circ \leq \theta \leq 90^\circ$ and that of the azimuthal angle to vary over $-180^\circ \leq \phi \leq 180^\circ$. Then, the overall output pattern $\bar{g}(\theta, \phi)$ is defined as:

$$\bar{g}(\theta, \phi) = \sum_{n=1}^N w_n \bar{g}_n(\theta, \phi) \exp\{i\xi\psi_n(\theta, \phi)\} \quad (2.21)$$

where, the element location is $\psi_n = x_n \sin \theta \cos \phi + y_n \sin \theta \sin \phi + z_n \cos \theta$, $\xi = \frac{2\pi}{\lambda}$ is the wavenumber, $w_n|_{n=1,2,3,\dots,N}$ are the elements complex weights.

If the antenna elements are identical, equation 2.21 becomes;

$$\bar{g}(\theta, \phi) = \bar{g}_1(\theta, \phi) \sum_{n=1}^N w_n \exp\{i\xi\psi_n(\theta, \phi)\} \quad (2.22)$$

where, $\bar{g}_1(\theta, \phi)$ is the element factor and $\sum_{n=1}^N w_n \exp\{i\xi\psi_n(\theta, \phi)\}$ is the array factor (AF). Equation 2.22 characterizes the *array pattern multiplication*.

Assuming we place N antenna elements uniformly linear on a particular axis with uniform spacing $n\Delta|_{n=0,1,2,3,\dots,N-1}$, then;

$$AF = \sum_{n=0}^{N-1} w_n \exp\{i\xi n \Delta \cos \theta\} \quad (2.23)$$

where, $w_n = \exp\{-i\xi n \Delta \cos \theta_0\} = (\exp\{i\gamma\})^n$.

From the summation theory, we can recall:

$$\sum_{n=0}^{\infty} \alpha^n = \frac{1}{1-\alpha}, \alpha \neq 1 \text{ and } \sum_{n=0}^{N-1} \alpha^n = \frac{1-\alpha^N}{1-\alpha}, \alpha \neq 1.$$

Applying these two theories to equation 2.23 and letting $\gamma = \xi\Delta(\cos\theta - \cos\theta_0)$, we get;

$$AF = \frac{1 - \exp\{iN\gamma\}}{1 - \exp\{i\gamma\}} \quad (2.24a)$$

$$= \frac{\exp\{iN\gamma/2\} \exp\{iN\gamma/2\} - \exp\{-iN\gamma/2\}}{\exp\{i\gamma/2\} \exp\{i\gamma/2\} - \exp\{-i\gamma/2\}} \quad (2.24b)$$

$$= \exp\{i(N-1)\gamma/2\} \frac{\sin(N\gamma/2)}{\sin(\gamma/2)} \quad (2.24c)$$

$$= \exp\{i(N-1)\xi\Delta/2(\cos\theta - \cos\theta_0)\} \frac{\sin\{\xi N(\Delta/2)(\cos\theta - \cos\theta_0)\}}{\sin\{\xi(\Delta/2)(\cos\theta - \cos\theta_0)\}} \quad (2.24d)$$

Since, $\frac{\sin(Nx)}{\sin(x)}$ behaves like $N \text{sinc}(x)$, the maximum value of equation 2.24 occurs when $\theta = \theta_0$. Therefore, normalizing the centre array at $z = 0$, we get:

$$AF = \frac{1}{N} \frac{\sin\{\xi N(\Delta/2)(\cos\theta - \cos\theta_0)\}}{\sin\{\xi(\Delta/2)(\cos\theta - \cos\theta_0)\}} \quad (2.25)$$

2.4.2 Beamforming

The combination of multiple signals with different complex weights from different receiving antenna elements form a new radiation pattern or what is mostly termed in radio astronomy as the primary beam. This phenomenon is known as *beamforming* and can be done in analogue component such as Low-Frequency Array (LOFAR) with high-band antennas (HBA) or after the signal is digitized, such as in the LOFAR stations. The algorithms used to generate this phenomenon can be classified into *coherent*, *incoherent* and multi-pixel beamformer methods. The application of coherent beamforming allows a narrow beam to be formed and therefore, provides a higher gain which is very useful during pulsar observation. Coherent beamforming increases the sensitivity in narrow field-of-view (FoV). Unlike coherent beamforming, incoherent beamforming does not affect FoV but increases the overall sensitivity. This kind of algorithm is very useful when searching for rare events where the location of occurrence is not known. The application of a multi-pixel beamformer such as the Giant Metre wave Radio Telescope (GMRT) combines the enhanced sensitivity of a coherent array beamformer with the wide FoV seen by an incoherent array beamformer. This algorithm is implemented using the recorded base-band data as in (Roy, Bhattacharyya, and Gupta 2012) making it possible to form sixteen directed beams in real-time. The multi-pixel beamformer can be used to improve the capabilities of studying pulsars.

2.4.3 Types of Radio Arrays

In this subsection, we discuss the main types of antenna receiving elements that can be used for radio interferometric observations. The advantages and disadvantages are also discussed.

2.4.3.1 Phased-Array Feeds

Generally, a single dish has one pixel and only records the total power captured within its primary beam at any given time. We can produce an image by pointing the single beam at different directions and then project the output on a sky grid. A feed design for a dish which generates multiple feeds instead of the single ‘pixel’ feed is known as a *phased-array feed* (PAF). This new technology in radio astronomy is same as having several arrays pointing at different places simultaneously. Its feed horn is electrically large and collects nearly all focused signal energy. Imaging with an array of multi-beam antennas gives a good resolution and increased in FoV. This increased in FoV is as a result of each receiving element requires its own isolated analogue front-end and digital back-end, making the feed more expensive. This new technology undergoing development and currently, PAFs have a higher system temperature and more limited analogue bandwidth compared to a single pixel feed. Additionally, the calibration of PAFs are a new challenge, and the software and techniques are in an ongoing state of development. Some of the PAF-based arrays are the Aperture Tile In Focus (APERTIF) project upgrade for Westerbork Synthesis Radio Telescope (WSRT) as in Fig. 2.6 and reproduced from (Garrett 2012), Australian Square Kilometre Array Pathfinder (ASKAP) also displayed in Fig. 2.6, GBT and the SKA MID survey.



Figure 2.6: Wide gain in FoV enabled by PAFs. Right-centre: APERTIF installed at the focus of a WSRT telescope. Extreme right: PAFs installed on ASKAP (courtesy CSIRO).

2.4.3.2 Transiting Arrays

Unlike having a dish that can track a particular point in the sky over many hours, a transiting array has elements with limited mobility making the sky to drift through the primary beam of the elements. Its feed has an effective primary beam which is large compared to that of a dish. As a source enters into the beam, it starts with a small apparent flux, then gradually increases until the source peaks at the zenith. It then decreases as it moves across the beam side lobes until it finally sets at the horizon. Some of the transiting Arrays are Precision Array for Probing the Epoch of Reionization (PAPER), Long Wavelength Array (LWA), Medicina Northern Cross and the Murchison Widefield Array (MWA) as shown Fig. 2.7. There are obvious cost advantages to building an array with no moving parts. Such arrays have wide FoV and can have the individual elements place close together. This allows for large-scale structure experiments such as Epoch of Reionization (EoR) and Baryon Acoustic Oscillations (BAO) studies. The disadvantages compared to dishes create a new challenge for calibration and imaging. The individual elements are less sensitive compared to a dish, so more elements are needed and requires larger correlator systems. Also, as the sky transits, the apparent flux of sources changes, so the primary beam must be well known in order to get back to the intrinsic flux of the sky. Depending on the scale of the primary beam, a transiting array has set amount of time per day in which a section of the sky can be observed. This means, a deep integration of a region of sky is not possible without observing for many days.



Figure 2.7: Transiting Arrays:- PAPER (top-left), LWA (bottom-left), Medicina Northern Cross (top-right) and MWA (bottom-right).

2.4.3.3 Aperture Arrays

We can convert a transiting array into a digital dish to form an *aperture array*. This makes it possible to point the digital dish in many directions of the sky simultaneously. The idea with an aperture array is that by updating the beamforming weights, the beam of the aperture array can track a region of the sky. The aperture array takes advantages from both dishes and transiting arrays. The main cost is the analogue and digital electronics to build such an array. For this reason, the aperture array is mainly used for low-frequency science, such as LOFAR as in Fig. 2.8 and the future SKA-low shown in Fig. 2.9, as the Dense Aperture Array (DAA) components are cheaper. With improved technology, the price of higher frequency components will make it possible to increase the observable frequency. A second issue with aperture arrays is that the primary beam changes depending on pointing location and frequency. As the beam is a weighted sum of all the individual elements there is limited precision to the beam shape. There is also the issue of sparse and dense aperture arrays. When the elements of the aperture array are placed closer than $\lambda/2$ observing wavelength the array is *dense*. The array is fully sampling the wavefront and there are no beam artefacts such as *grating lobes* (a type of side lobe) which introduces significant structure into the beam. If the elements are further apart than $\lambda/2$ then these side lobes structures appear and limit the sensitivity and FoV. For a single observing frequency, designing an aperture array is simple as all the

elements are spaced at $\lambda/2$. But, for wide-band arrays, if the elements are placed at $\lambda_i/2$ for a wavelength λ_i , then for any wavelength $< \lambda_i$ the array configuration under-samples that observing wavelength and introduces large grating lobes. Therefore, a balance between observing bandwidth, cost and dense versus sparse trade-off must be made during the array design.



Figure 2.8: Aperture Array:- LOFAR.



Figure 2.9: SKA-2 Dense Aperture Arrays precursor telescope.

A more detailed discussions on radio arrays can be seen in (Foster 2015; Garrett 2012).

2.5 Super-Synthesis Technique

2.5.1 Construction of Radio Images

Radio telescopes are used to measure the flux density of an observed radio source by integrating the intensity over the telescope beam. Intensity image of the observed source is then produced from the data obtained from the radio telescopes.

Fig. 2.10(a) as in (Joardar et al. 2010) displays a single dish radio telescope steering at a distant radio source with parallel rays illuminating the dish aperture. Consider that the aperture plane is located at the origin of a rectangular coordinate system (u, v, w) with w pointing directly at the source as in Fig. 2.10(b). Also, on the sky, consider the electric field distribution to be centered on different coordinate system (l, m). The electric field distribution $\varepsilon(u, v)$ on the u, v plane is defined in terms of the electric field distribution of $V(l, m)$ on the sky. Considering that we have full information about $\varepsilon(u, v)$, we can then find the auto-correlation of each of the electric field points on the u, v plane to get $W(u, v)$. The intensity field distribution $I(l, m)$ of the source is measured when we find the Fourier transform on $W(u, v)$. Realistically $\varepsilon(u, v)$ is not achievable, since the antenna produces a single output. This output is very significant as it shows a basic relation between intensity map of radio source on the sky with the aperture illumination.

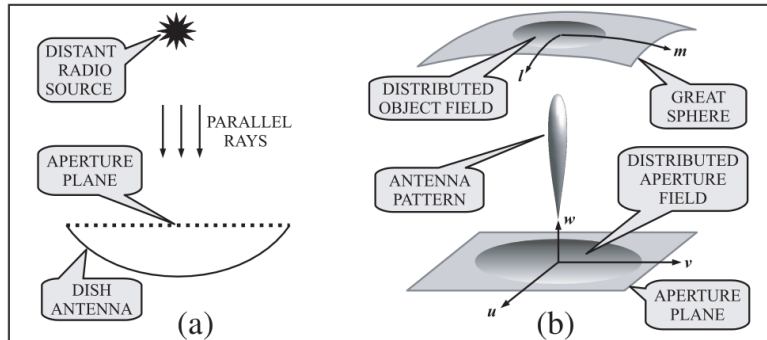


Figure 2.10: (a) A distant radio astronomical source illuminates a dish antenna with parallel rays. (b) Electric field distributions of a source on the great sphere and antenna aperture on the aperture plane

Although single dish radio telescopes like GBT, are very advantageous as discussed in (Emerson 2002) in making primary surveys of the sky at low resolution, their constructions are limited by their physical sizes. However, its data can be put together with antenna array also known as interferometer to obtain a good balance between lower and higher spatial frequency components.

Instead of a single dish antenna, an interferometer with the assistance of the rotation of Earth can synthesize a large antenna aperture. This technique is known as *super-synthesis* (Machin,

Ryle, and Vonberg 1952; Thompson and Bracewell 1974).

Consider a large number of radio telescopes distributed across a plane area situated at a given longitude, latitude and altitude as shown in Fig. 2.11(a) such that they track a distant radio source located on the celestial North pole. Consider also a rectangular coordinate system (u', v', w') whose origin is at the phase center of telescope plane as in Fig. 2.11(b) reproduced from (Joardar et al. 2010) such that w' axis points towards the zenith (source) and the u', v' plane remains stationary to the observed source. From the observed source towards the antennas, due to the rotation of the Earth, the position of the antennas appears to be moving over the u', v' plane. The outputs of individual radio telescopes is recorded at each integration time and then placed on the u', v' plane.

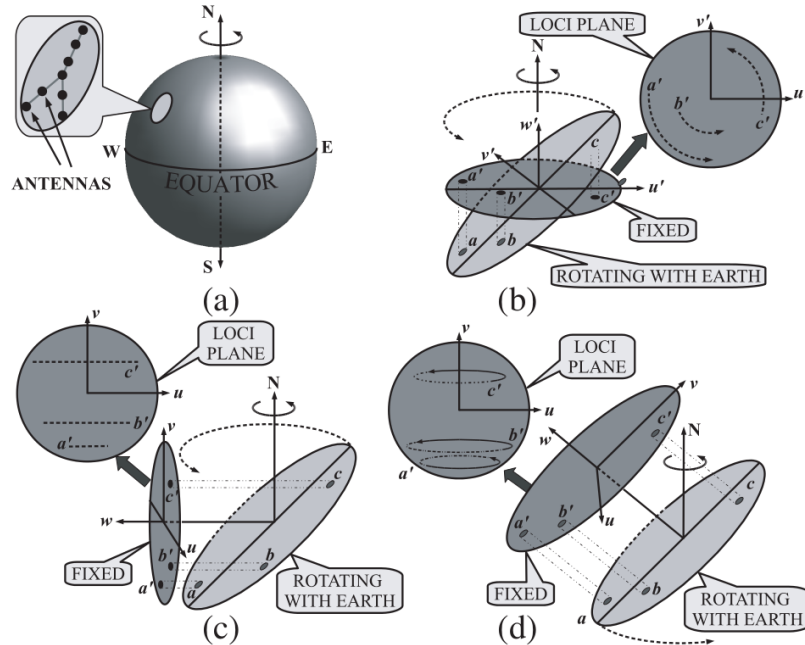


Figure 2.11: The principle of super synthesis. (a) An interferometer rotates with the Earth rotation (b) Observing a radio source towards celestial North Pole. (c) Observing a radio source along the celestial equator. (d) Observing a radio source along a celestial latitude in between.

The loci a' , b' and c' of the radio telescopes a , b and c respectively on the u', v' plane forms circles over a period of 24 h. Having numerous radio telescopes at different baselines from the origin of the (u', v', w') coordinates over a period of 24 h, the u', v' plane gets highly populated. The u', v' plane then forms the aperture of a large synthesized antenna. Thus, we apply Fourier transform on the u', v' plane data after calibration to obtain the field distribution

of the source. Considering a radio source on the celestial equator as presented in Fig. 2.11(c), the loci a' , b' and c' on the u', v' plane form straight lines. Thus, if all the radio telescopes are mounted on a single East-West line then their respective loci be a straight line and this not good enough for making a radio image. It is therefore necessary to mount some of the radio telescopes spread along the North-South axis. If the observed source is located at a celestial latitude between $(0^\circ, 90^\circ)$ or $(-90^\circ, 0^\circ)$, each of the loci form an ellipse as shown in Fig. 2.11(d).

2.5.2 Correlator Super-synthesis Arrays

The correlation products between any pair of antennas are used to fill the u, v plane, where the (u, v, w) coordinates are measured in wavelengths. If there are N antennas in an array, then the number of cross correlation is defined as $N \left(\frac{N-1}{2}\right)$. In any pair of antennas in an interferometer, when we fix one of the antennas at the origin of the (u, v, w) , the baseline between the two antennas on the u, v plane will rotate through 180° in 12 h. We obtain similar observation results when the other antenna is considered as the origin of the (u, v, w) coordinates. This makes it possible to cover 360° of baseline rotation in half a day. Thus, data obtained from an interferometer is a measure of the spatial coherence function called *visibility* and is denoted as $V(u, v)$. This visibility data cover only 1/2 of the u, v plane from a 12 h observation, but the other 1/2 can be obtained using equation 2.26, where $V^*(u, v)$ is the complex conjugate of $V(u, v)$. Hence, we can derive 24 h of observed data from a 12 h observation.

$$V(-u, -v) = V^*(u, v) \quad (2.26)$$

2.5.3 The Van Cittert-Zernike Equation

Consider a 2 element interferometer observing a radio source as in Fig. 2.12(a) obtained from (Joardar et al. 2010) such that the first element is positioned at the origin of the (u, v, w) coordinate system. Also, consider $I(l, m)$ to be the intensity distribution of the source on the celestial sphere such that the origin of the l, m coordinate system is at the phase reference position. If we denote $I(\bar{s})$ as the sky brightness at a frequency ν in the direction \bar{s} and assume $A(\bar{s})$ to be the effective aperture area of an antenna in the same direction, then the

signal power received over a bandwidth $\Delta\nu$ within a solid angular element $d\Omega$ for each antenna is given by $A(\bar{s})I(\bar{s})\Delta\nu d\Omega \cos(2\pi\nu\tau_g)$. Therefore, the correlated signal power dr over $d\Omega$ is given as;

$$dr = A(\bar{s})I(\bar{s})\Delta\nu d\Omega \cos(2\pi\nu\tau_g) \quad (2.27)$$

Integrating equation 2.27 over the celestial sphere we get the correlator power r :

$$r(\vec{d}_\lambda, \bar{s}) = \Delta\nu \int A(\bar{s})I(\bar{s}) \cos[2\pi(\vec{d}_\lambda \bar{s})] d\Omega \quad (2.28)$$

where, \vec{d}_λ is the baseline vector specified by the (u, v, w) coordinates and measured in wavelengths.

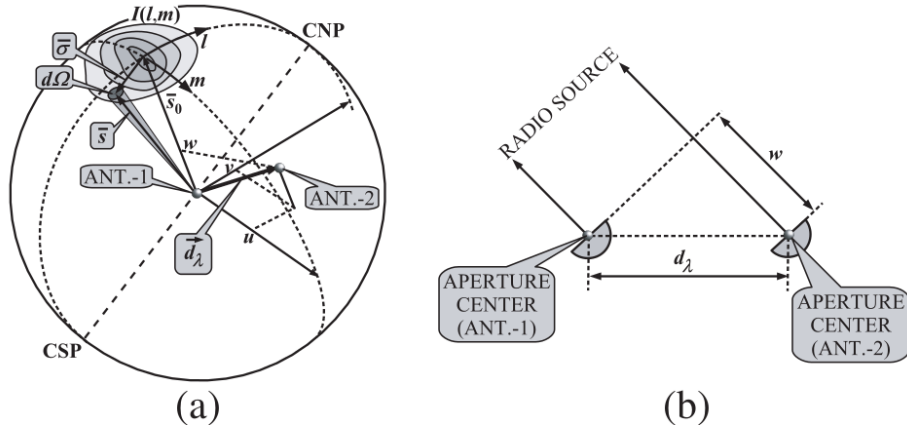


Figure 2.12: Geometry of a radio source and a simple interferometer. (a) An observed radio source with intensity distribution $I(l, m)$ using a simple two element radio interferometer. (b) Lower the elevation angle of the radio source the larger the value of w .

If we put $\bar{s} = \bar{\sigma} + \bar{s}_0$ such that $\bar{\sigma}$ is the space vector from the phase reference point to the observing point. Rewriting equation 2.28 we get;

$$\begin{aligned} r(\vec{d}_\lambda, \bar{s}_0) &= \Delta\nu \cos[2\pi(\vec{d}_\lambda \bar{s}_0)] \int A(\bar{\sigma})I(\bar{\sigma}) \cos[2\pi(\vec{d}_\lambda \bar{\sigma})] d\Omega \\ &\quad - \Delta\nu \sin[2\pi(\vec{d}_\lambda \bar{s}_0)] \int A(\bar{\sigma})I(\bar{\sigma}) \sin[2\pi(\vec{d}_\lambda \bar{\sigma})] d\Omega \end{aligned} \quad (2.29)$$

The visibility V is defined as a complex function:

$$V = |V| \exp(j\phi_\nu) = \int A'(\bar{\sigma})I(\bar{\sigma}) \exp(-j2\pi \vec{d}_\lambda \bar{\sigma}) d\Omega \quad (2.30)$$

with the real part being;

$$V = |V| \cos(\phi_\nu) = \int A'(\bar{\sigma}) I(\bar{\sigma}) \cos(2\pi \vec{d}_\lambda \bar{\sigma}) d\Omega \quad (2.31)$$

and the imaginary part being;

$$V = |V| \sin(\phi_\nu) = - \int A'(\bar{\sigma}) I(\bar{\sigma}) \sin(2\pi \vec{d}_\lambda \bar{\sigma}) d\Omega \quad (2.32)$$

where, $A'(\bar{\sigma}) = \frac{A(\bar{\sigma})}{A_0}$ is the normalized beam pattern of an antenna with A_0 being the peak antenna gain.

Substituting equation 2.31 into 2.30, we get;

$$r(\vec{d}_\lambda, \bar{s}_0) = A_0 \Delta\nu |V| \cos[2\pi(\vec{d}_\lambda \bar{\sigma} - \phi_\nu)] \quad (2.33)$$

Equation 2.33 shows that an interferometer measures the visibility which is the spacial coherence function with a different normalization.

To produce an image from equation 2.33, we need to know their positions on the u, v, w coordinate system and compare them with l, m coordinate system. As the elevation angle of the observed source decreases as in Fig. 2.12(b), the w term increases:

$$\vec{d}_\lambda \bar{s} = ul + vm + wn \quad (2.34)$$

If $\bar{s} = \bar{s}_0$ equation 2.34 simplifies to;

$$\vec{d}_\lambda \bar{s} = w \quad (2.35)$$

The solid angle $d\Omega$ can be expressed in polar coordinates as $d\Omega = \sin \theta d\theta d\phi$, where θ and ϕ are the polar and azimuthal angles in the (u, v, w) plane, that is, $\theta = \sin^{-1}(\sqrt{l^2 + m^2})$ and $\phi = \tan^{-1}(m/l)$. Using the Jacobian method, we can transform the coordinates (θ, ϕ) into (l, m) :

$$d\Omega = \frac{dldm}{n} = \frac{dldm}{\sqrt{1 - l^2 - m^2}} \quad (2.36)$$

Using equations 2.34 to 2.36, we can therefore rewrite the visibility V in equation 2.34 in terms of u, v, w :

$$V(u, v, w) = \int_{-\infty}^{\infty} \int_{-\infty}^{\infty} \frac{A'(l, m)I(l, m)}{\sqrt{1 - l^2 - m^2}} \exp\{-j2\pi[ul + vm + w(\sqrt{1 - l^2 - m^2} - 1)]\} dldm \quad (2.37)$$

Equation 2.37 is known as *van Cittert-Zernike equation* (Thompson, Moran, and Swenson 2001; Thompson and Bracewell 1974; Rau et al. 2009) and it shows that the visibility $V(u, v, w)$, is a Fourier transform of the product of the sky brightness $I(l, m)$, the primary beam response $A'(l, m)$ and $1/\sqrt{1 - l^2 - m^2}$.

When the distance of the observed source becomes less, $|l|$ and $|m|$ become very less such that $w(\sqrt{1 - l^2 - m^2} - 1)$ approaches zero and equation 2.37 reduces to;

$$V(u, v, w) \simeq V(u, v, 0) = \int_{-\infty}^{\infty} \int_{-\infty}^{\infty} \frac{A'(l, m)I(l, m)}{\sqrt{1 - l^2 - m^2}} \exp\{-j2\pi(ul + vm)\} dldm \quad (2.38)$$

and the inverse transform being defined by;

$$\frac{A'(l, m)I(l, m)}{\sqrt{1 - l^2 - m^2}} = \int_{-\infty}^{\infty} \int_{-\infty}^{\infty} V(u, v) \exp\{j2\pi(ul + vm)\} dudv \quad (2.39)$$

2.5.4 Filling the u,v Plane with Visibilities

Consider the phase reference position of an observed radio source is at (H_0, δ_0) in the local equatorial coordinate system. Assume X_λ, Y_λ and Z_λ are the baseline components in a rectangular coordinate system measured in wavelengths (Thompson, Moran, and Swenson 2001), then the u, v can be written as;

$$u^2 + \left[\frac{v - Z_\lambda \cos(\delta_0)}{\sin(\delta_0)} \right]^2 = X_\lambda^2 + Y_\lambda^2 \quad (2.40)$$

Equation 2.40 represents an ellipse which splits into 2 in the u, v plane if $Z_\lambda \neq 0$ (Thompson, Moran, and Swenson 2001). Fig. 2.13(a) produced from (Joardar et al. 2010) displays

equation 2.40 when observing a radio source at declination δ_0). That for Fig. 2.13(b) displays cases of a North-South baseline for different values of δ_0 .

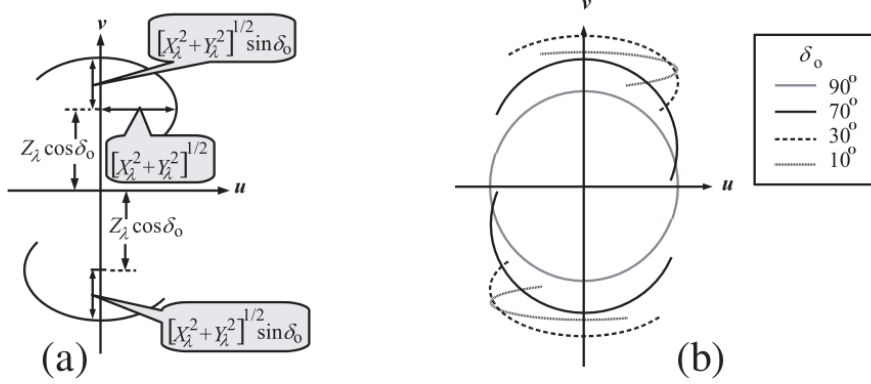


Figure 2.13: Locus on the u, v plane.. (a) Locus of the ellipse on u, v plane for a baseline with $Z_\lambda \neq 0$ observing a radio source at declination δ_0 . (b) Different declinations for different cases.

The KAT-7 consists of seven observing antennas located at latitude -30° , longitude 21° and altitude $1038m$ in configuration as shown in Fig. 2.14(a). Fig. 2.14(b) displays the u, v coverage at particular synthesis time with observed radio source at the phase centre. The circular structure rotates along with the Earth. If the zenith coincides with a celestial pole, then each point traces out a circle. Otherwise, the tracings could be elliptical, broken ellipse, or straight line (zero declination). When we increase the synthesis time, more data fill the u - v plane. Using equation 2.39, the intensity distribution $I(l, m)$ or image of the radio source is made. This is actually done after calibrating the data (Thompson, Moran, and Swenson 2001; Thompson and Bracewell 1974; Rau et al. 2009; Beardsley et al. 2016; Junklewitz et al. 2016).

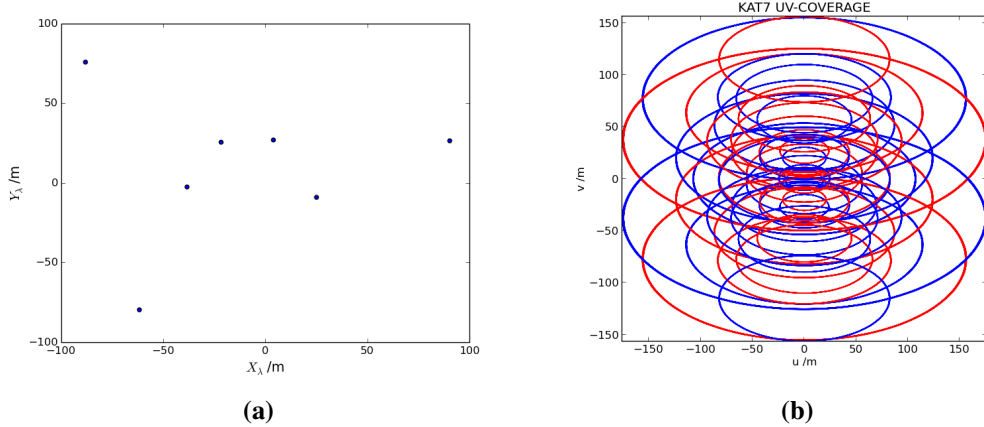


Figure 2.14: Filling the u - v plane with visibilities. (a) The KAT-7 configuration. (b) The u - v plane coverage of a 4h period of observation obtained from a source at the phase centre.

Using Fast Fourier Transform (FFT) approach, the data on u - v plane is interpolated on a uniform grid (Thompson, Moran, and Swenson 2001; Fu and Wu 2005; Zhang, Wu, and Sun 2007) and at the same time employ tapering technique (Thompson, Moran, and Swenson 2001) to reduce the side lobes of the synthesized antenna beam. The dirty image obtained after FFT may contain lots of artifacts (Desai et al. 2016). These are removed using algorithms such as CLEAN (Abrantes et al. 2009; Camps et al. 1998; Levanda and Leshem 2010b; Coughlan and Gabuzda 2012) or MEM (Coughlan and Gabuzda 2012; Junklewitz et al. 2016; Coughlan and Gabuzda 2013).

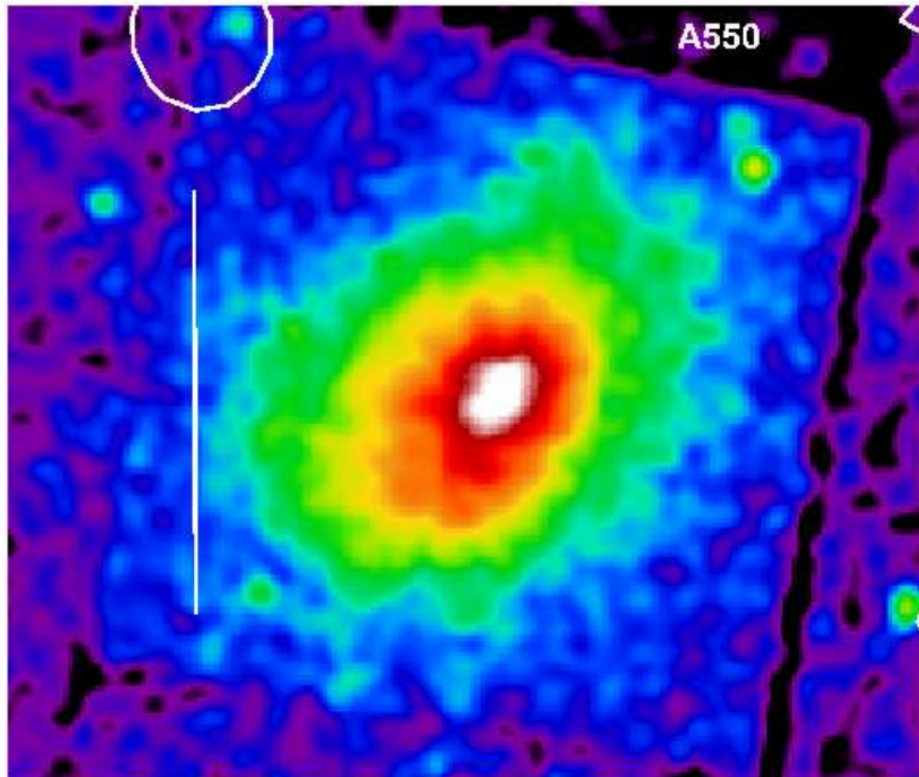


Figure 2.15: : 1.86 GHz KAT-7 radio contours of the A 550 cluster overlaid on the X-ray XMM-Newton images as an example of target that does not show any diffuse radio emission corresponding to the cluster centre. The image is not corrected by the primary beam. The vertical white bar indicates a 800kpc size..

Fig. 2.15 displays 1.86 GHz KAT-7 radio contours of the A 550 cluster as in (Bernardi et al. 2016) and drawn at $-2.5, 2.5, 10$ and 40 mJy beam^{-1} with positive (negative) contours drawn using solid (dashed) lines.

Chapter 3

FOREGROUND

Overview

Chapter Three briefly gives a review foregrounds with synchrotron, free-free and thermal dust emission. the components for separating foregrounds are also discussed.

3.1 Introduction

The observations and measurements of the Cosmic Microwave Background (CMB) temperature anisotropies have become the most dominant probe of the early universe and this will continue to revolutionize our understanding of cosmology. Since the discovery of CMB in 1965, the first measurement of CMB fluctuations in 1992 have relative amplitude of $\sim 2 \times 10^{-5}$. This minute effect means that a very high precision measurement is required to observe it. Recent satellite CMB experiments such as Cosmic Background Explorer (COBE) (Bennett et al. 1996), Wilkinson Microwave Anisotropy Probe (WMAP) (Hinshaw et al. 2013) and Planck (Planck Collaboration et al. 2014) have revealed the full-sky view at microwave frequencies. They have also provided us with numerous informations about the cosmological CMB and the various astrophysical processes in the Galaxy through foreground emissions. A better understanding of the foreground emissions can help us to determine the cosmological CMB signal and even estimate weaker polarisation signals from the CMB

anisotropies. In this chapter, we review the recent progress on the foreground subtraction methods and current knowledge about the foregrounds mainly focusing on the large-scale, diffuse, Galactic components.

3.2 Galactic Foreground

The measured diffuse radiation of the sky is a superposition of the CMB and of emission from Galactic and extragalactic sources. As seen in Fig. 3.1 and reproduced from (Schneider 2006, p. 16), the foreground emission clearly dominates in the neighbourhood of the Galactic disk and reduces very much at higher Galactic latitudes. The topmost image in Fig. 3.1 shows a dipole distribution which emanates from the Earth’s motion relative to the rest frame of the CMB. Due to the Doppler effect, we move at a speed of $\sim 600\text{km/s}$ relative to that system, which leads to a dipole anisotropy with an amplitude of $\Delta T/T \sim \nu/c \sim 2 \times 10^{-3}$.

If the contribution of the dipole is subtracted, we produce the map in the middle which clearly shows the emission from the Galactic disk. Since this emission has a different spectral energy distribution thus, it is not a blackbody of $T \sim 3K$, it can also be subtracted to produce the temperature map at the bottom. These are the primordial fluctuations of the CMB, with an amplitude of about $\Delta T/T \sim 2 \times 10^{-5}$. However, due to its different spectral behaviour, the foreground emission can be identified and subtracted.

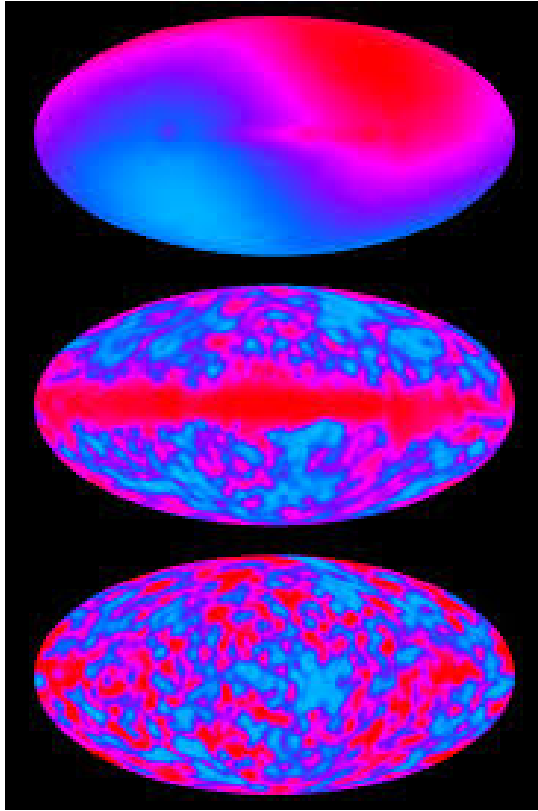


Figure 3.1: Temperature distribution of the CMB on the sky as measured by the COBE satellite.

Numerous research studies (Wolz et al. 2014; Jelić et al. 2010; Santos et al. 2015b; Alonso et al. 2015; Kiyotomo 2014) have clearly shown that synchrotron emission from the Galaxy dominates at low microwave frequencies ($\lesssim 30\text{GHz}$), whilst that of thermal dust emission is at higher frequencies ($\lesssim 70\text{GHz}$). Between these two components in frequency, lies the thermal free-free and non-thermal dust emissions, which are formed as a result of spinning dust grains as in Fig. 3.2 (Bennett et al. 1996). The subsections from 3.2.1 to 3.2.3 discuss briefly the components of the Galactic foregrounds, paying particular attention to their contribution to the polarisation measurements.

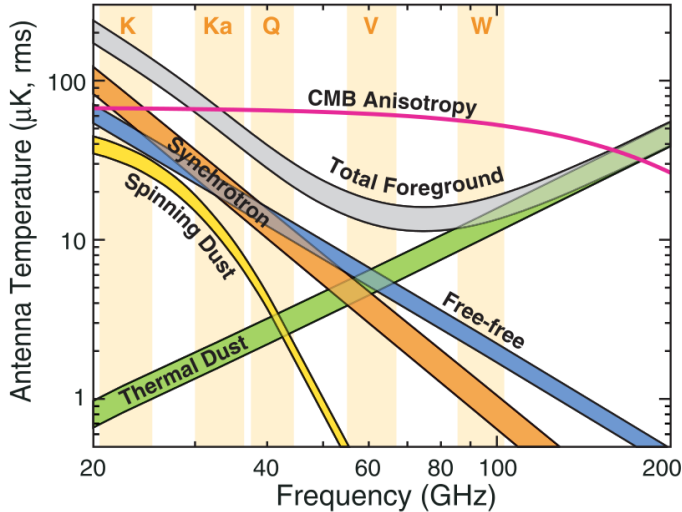


Figure 3.2: Different spectra of foreground emission components in the GHz range as measured by WMAP.

3.2.1 Synchrotron

A varying magnetic field can accelerate charge particles to emit radiation. The Diffuse Galactic Synchrotron Emission (DGSE) emerges from interactions between cosmic ray electrons and magnetic fields in the Galaxy. These interacting particles are accelerated to relativistic speeds in very high energetic environments, such as shock-waves from supernovae explosions. The synchrotron intensity and spectrum depend on the magnetic field strength and cosmic ray energy, showing significant spatial variations on the sky. The energy distribution of cosmic ray electrons follows a power-law such that $N(E) \propto E^{-\tau}$ where the energy $E > 10$ GeV (Adriani et al. 2011). The spectral index τ of the distribution is ≈ 3.0 and this is universally accepted when modelling in synchrotron and magnetic field.

According to (Miville-Deschénes et al. 2008), the intensity of a synchrotron radiation S_{sync} , at a frequency ν is mathematically expressed as;

$$S_{sync}(\nu) = \varepsilon_{sync}(\nu) \int_z n_e B_{\perp}^{(1+\tau)/2} dz \quad (3.1)$$

where equation 3.1 is integrated with respect to the sight-line z , n_e is cosmic ray density and $B_{\perp} = \sqrt{B_x^2 + B_y^2}$ is the x, y components of the magnetic field of the sky. From the power

Table 3.1: Measured Spectral Indices at Different Frequency Bands

γ_{sync}	Frequency Band (GHz)
-2.55	0.045 – 0.408
-2.71	0.408 – 2.30
-3.01	2.300 – 33.0

law we can express the emissivity term $\varepsilon_{sync}(\nu)$ as;

$$\varepsilon_{sync}(\nu) = \varepsilon_0 \nu^{-(\tau-1)/2} \quad (3.2)$$

Recall Rayleigh-Jeans law at frequency ν :

$$B_\nu(T) = \frac{2\nu^2 k_B T}{c^2} \quad (3.3)$$

where, c is the speed of light, k_B is the Boltzmann constant and T is the temperature in kelvins. Using equation 3.3, we can convert equation 3.1 into a brightness temperature T_{sync} at frequency ν :

$$T_{sync}(\nu) = \frac{c^2 S_{sync}(\nu)}{2k_B \nu^2} \quad (3.4)$$

Hence, the brightness temperature T_{sync} of synchrotron emission in a particular sight-line is expressed in power law at frequency ν :

$$T_{sync}(\nu) = T_{sync}(\nu_0) \left(\frac{\nu}{\nu_0} \right)^{\gamma_{sync}} \quad (3.5)$$

where, $\gamma_{sync} = -(\tau + 3)/2$. The spectral index γ_{sync} , as discussed by (Navarro 2014) changes at different frequency bands as displayed in table 3.1.

Fig. 3.3 is the 408 MHz full-sky survey taken from (Navarro 2014) and originally produced by (Haslam et al. 1982) displaying the sky in mollview form in Galactic coordinates at a frequency where the diffuse synchrotron emission is most dominant. A number of extragalactic sources are visible in the map, including the Cen A galaxy and the Magellanic clouds.

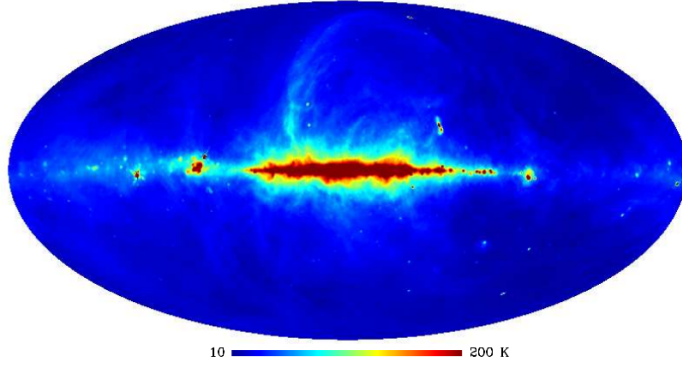


Figure 3.3: 408 MHz Full-Sky Map.

Synchrotron emissions are intrinsically linearly polarised since the cosmic ray electrons accelerated by the magnetic fields emit photons and are therefore polarized perpendicularly to the lines of field. Thus, the cosmic rays and magnetic field distributions of a galaxy can be used to predict the polarization foreground from synchrotron emission and remove it from observed maps. The degree of linear polarization integrated over all electron energy and frequency is defined as $l = (\tau + 1)/(\tau + 7/3)$. The polarisation factor (l) can be increased to 0.75 if the cosmic ray spectral index $\tau \approx 3$. According to (Miville-Deschénes et al. 2008), we can express the polarised intensity in terms of Stokes parameters Q and U at frequency ν :

$$I(\nu) = \sqrt{Q(\nu)^2 + U(\nu)^2} \quad (3.6)$$

with the angle of polarisation to be:

$$\varphi(\nu) = \frac{1}{2} \arctan \left(\frac{U(\nu)}{Q(\nu)} \right) \quad (3.7)$$

From equation 3.1, we can mathematically express the Stokes parameters Q and U of polarised synchrotron emission integrated along the sight-line z as;

$$Q_{sync}(\nu) = l_{sync} \varepsilon_{sync}(\nu) \int_z n_e B_{\perp}^{(1+\tau)/2} \cos(2\alpha) \sin(\beta) dz \quad (3.8)$$

and

$$U_{sync}(\nu) = l_{sync} \varepsilon_{sync}(\nu) \int_z n_e B_{\perp}^{(1+\tau)/2} \sin(2\alpha) \sin(\beta) dz \quad (3.9)$$

where, $\cos(2\alpha) = \frac{B_x^2 - B_y^2}{B_\perp^2}$ $0 < \cos(2\alpha) < 1$, $\sin(2\alpha) = -\frac{B_x^2 B_y^2}{B_\perp^2}$ $0 < \sin(2\alpha) < 1$ and
 $\sin(\beta) = \sqrt{1 - \frac{B_x^2}{B_\perp^2}}$ $0 < \sin(\beta) < 1$.

3.2.2 Free-free

Free-free emission or thermal bremsstrahlung is produced from electron–ion scattering in interstellar plasma. Thus, it occurs when an accelerated charged particle (i.e. thermally hot electrons) is deflected by an atom, molecule or ion. The $H\alpha$ line is a good tracer of free-free emission since both are emitted by the same ionized medium and both have intensities proportional to Emission Measure (EM) (Smoot 1998; Kiyotomo 2014) such that $EM \propto \int_z n_e^2 dl$ (z is the sight-line integral of free electron density n_e). The free-free emission intensity along a sight-line z , is defined as;

$$I_{free}(\nu) = 5.4(10^{-16}) \int_z \frac{g_{ff} Z_i^2 n_e n_i}{\sqrt{T_e}} \exp\left(-\frac{h\nu}{k_B T_e}\right) dz \text{ JySr}^{-1} \text{ cm}^{-1} \quad (3.10)$$

where, n_e, n_i are the number densities of electron and ions respectively. Z_i is the atomic number and $T_e \simeq 800K$ is the electron temperature. For $h\nu \ll k_B T$, the Kramers-Gaunt factor g_{ff} is expressed as;

$$g_{ff} = \frac{\sqrt{3}}{\pi} \left\{ \ln \frac{(2k_B T)^{3/2}}{\pi e \nu \sqrt{m_e}} - \frac{5\Upsilon}{2} \right\} \quad (3.11)$$

where, e is the electron charge, m_e is the electron mass and Υ is Euler–Mascheroni constant.

From equation 3.10 we can express in terms of brightness temperature T_B and thermodynamic temperature change ΔT_{CMB} :

$$\Delta T_{CMB} = \frac{(\exp(x) - 1)^2}{x^2 \exp(x)} \frac{\lambda^2}{2k} I_{free}(\nu) \quad (3.12a)$$

$$= \frac{(\exp(x) - 1)^2}{x^2 \exp(x)} T_B \quad (3.12b)$$

where, $x \equiv h\nu/k_B T_{CMB}$ and $T_{CMB} = 2.725$ K.

The free-free emission of average spectral index $\varsigma_{free} \simeq -2.1$ (Navarro 2014) and this value can vary slowly with a change in ν and T_e .

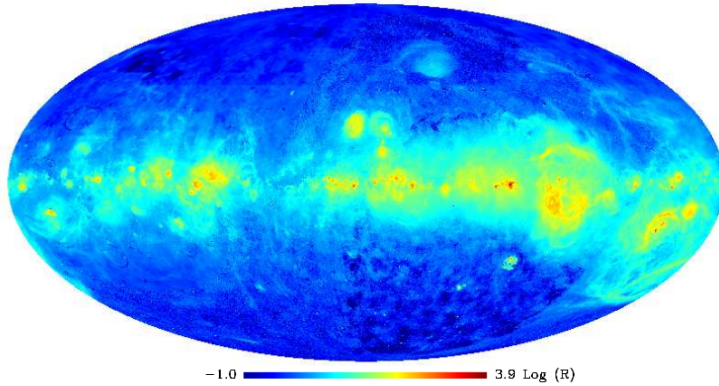


Figure 3.4: A Full-Sky $H\alpha$ Map.

Fig. 3.4 is taken from (Navarro 2014) and reproduced by (Finkbeiner, Langston, and Minter 2004) depicts a full-sky $H\alpha$ map that is corrected for dust extinction. It only traces the free-free emission on regions away from the Galactic plane, where the dust extinction is less dominant.

Thermal free-free emission has zero net polarisation since the scattering directions of electrons are isotropic and irregular. Furthermore, Thompson scattering could produce a polarisation signal at the edges of H_{II} regions, at a maximum value of $\sim 10\%$ and therefore, measuring the free-free polarisation over the entire sky from that, we get less than 1%.

3.2.3 Thermal dust

Thermal emission is produced from dust grains and mostly made of graphites, silicates, and Polycyclic Aromatic Hydrocarbons (PAHs). It dominates the foreground at frequencies $\gtrsim 70$ GHz. The dust grains get heated by the interstellar radiation field and then emit far-infrared light which eventually lead to multiple temperatures. The thermal dust intensity at temperature T_{dust} and frequencies ν is defined as;

$$I_\nu = B_\nu(T_{dust})\tau_{dust}(\nu) \quad (3.13)$$

where, $B_\nu(T_{dust})$ is the Planck function at dust temperature T_{dust} in the interval ($10 \lesssim T_{dust} \lesssim 50$) K and

$$\tau_{dust}(\nu) = \kappa(\nu) \int \rho dz \quad (3.14a)$$

$$= \kappa(\nu) \Sigma_{dust} \quad (3.14b)$$

such that, $\kappa(\nu)$ is the dust emissivity cross section per mass unit $cm^2 g^{-1}$, ρ is the dust mass density along the sight-line z and $\Sigma_{dust} = r\mu m_H N(H_2)$ is the dust mass for r being the dust-to-gas mass ratio, μ the mean molecular weight, m_H the mass of a Hydrogen gas and $N(H_2)$ the hydrogen column density.

Expressing $\kappa(\nu)$ in power law (Compiègne et al. 2011; Navarro 2014), we get;

$$\kappa(\nu) = \kappa_0(\nu) \left(\frac{\nu}{\nu_0} \right)^{\beta_{dust}} \quad (3.15)$$

Substituting equations 3.14 and 3.15 into equation 3.13 we get;

$$I_\nu = B_\nu(T_{dust}) \kappa_0(\nu) r \mu m_H N(H_2) \left(\frac{\nu}{\nu_0} \right)^{\beta_{dust}} \quad (3.16)$$

For modelling huge dust grains, the intensity of thermal emission in equation 3.16 can be reasonably well fitted with a modified black-body as discussed by (Fanciullo et al. 2015; Pagani et al. 2015; Navarro 2014):

$$I_\nu = B_\nu(T_{dust}) \kappa_0 \left(\frac{\nu}{\nu_0} \right)^{\beta_{dust}} \quad (3.17)$$

Fig. 3.5 shows Planck 857 GHz map of the whole sky, tracing the thermal emission from the large grains.

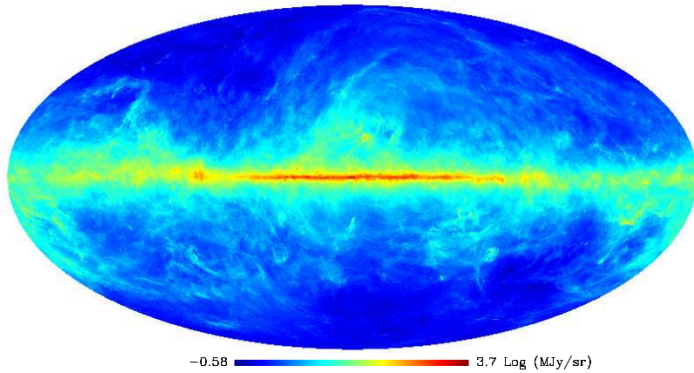


Figure 3.5: *Planck 857 GHz Full-Sky Map Tracing the Radiation from Thermal Dust.*

Large dust grains will generally radiate or even absorb photons mainly along the longest axis, making the long grain axis to become perpendicular to the local magnetic fields (Lazarian and Prunet 2002). Correlation of the polarization observations with the local magnetic field will tend to be parallel to the fields in the background light with absorption. This actually supports what was discovered in the middle of the last century by (Hiltner 1949; Hall 1949). Furthermore, the degree of polarisation is a good tracer of the magnetic field, since the grain alignment processes with the interstellar field (Navarro 2014; Lazarian and Finkbeiner 2003).

WMAP observations by (Kogut et al. 2007), clearly indicated that the fractional polarization of thermal dust emission is ≈ 0.01 when close to the Galactic centre and increases to ≈ 0.06 at the anti-centre. It also reported that diffuse thermal dust emission at high latitudes produces a fractional polarization within the range of 0.036 ± 0.011 .

3.3 Component Separation Methods

The CMB sky observation components are considered to have radiations that can be separated into spatial and spectral divisions such that a radiation process k is mathematically modeled as;

$$u_k(\nu, \varpi) = a(\nu)s_k(\varpi) \quad (3.18)$$

then the observation is expressed as;

$$v_j(\varpi) = \sum_k u_k(\nu_j, \varpi) + n_j(\varpi) \quad (3.19)$$

where, j represents the detector and $n_j(\varpi)$ is the detector's noise contribution. For each component k this takes the form;

$$v(\varpi) = \mathbf{A}\mathbf{s}(\varpi) + \mathbf{n}(\varpi) \quad (3.20)$$

where, \mathbf{A} is the mixing matrix with the number of rows and columns denoting the number of detectors and number of components, respectively.

Finding the inverse of the mixing matrix \mathbf{A} is the main challenge in component separation which gives a solution:

$$\hat{\mathbf{s}} = \mathbf{W}\mathbf{v} \quad (3.21)$$

Equation 3.21 becomes a Blind Source Separation (BSS) problem (Albataineh and Salem 2014), since the mixing matrix \mathbf{W} and the matrix with the independent source components \mathbf{v} are unknown. It is a classical ill-posed inverse problem, which admits an infinite number of solutions. The following are some of the possible ways we can employ to determine the inverse in Equation 3.21;

- A simple inverse approach can be applied in the case of a square and nonsingular \mathbf{A} : $\mathbf{W} = \mathbf{A}^{-1}$. This solution is unique but can introduce noise.
- In the case of having more channels than components, a pseudo-inverse may be used: $\mathbf{W} = [\mathbf{A}^T \mathbf{A}]^{-1} \mathbf{A}^T$. Here, the solution is unique but since there is no noise weighting, there is the possibility of contaminating all the data after inversion for one bad channel.
- If the noise correlation matrix \mathbf{C}_n is known then a generalized least-squares solution is applied: $\mathbf{W} = [\mathbf{A}^T \mathbf{C}_n^{-1} \mathbf{A}]^{-1} \mathbf{A}^T \mathbf{C}_n^{-1}$. Here too, the solution is unique, giving the best linear solution in the limits of high signal-to-noise ratio (SNR).
- A Wiener Solution can also be used when the correlation between the sources, \mathbf{C}_s is identified: $\mathbf{W} = [\mathbf{A}^T \mathbf{C}_n^{-1} \mathbf{A} + \mathbf{C}_s^{-1}]^{-1} \mathbf{A}^T \mathbf{C}_n^{-1}$. Here, the solution is not unique

and also minimizes the variance of a random signal. For uniqueness, the Wiener filter becomes; $\mathbf{W} = \mathbf{C}_s \mathbf{A}^T [\mathbf{C}_n + \mathbf{A} \mathbf{C}_n \mathbf{A}^T]$, where in the limits of high SNR it tends to the pseudo-inverse case.

The simplest approach to derive the CMB is known as *template fitting*. It involves fitting of sky templates to all the non-CMB sky emissions and subtract them from the maps. However, more improved methods have been developed to address the BSS problem. For instance, the independent component analysis (ICA) methods developed, mostly depend on the statistical independence of the sources. These methods produce much better solutions than using a simple second-order decorrelation method, such as the principal component analysis. Most of the ICA methods such as FastICA, consider that sources are statistically independent and non-Gaussian. Also, the spectral matching method considers the case of mixed stationary Gaussian components and goes further by taking into account the additive instrumental noise. This method works in spherical harmonic domain, which has the advantage of better control of the beams of the instrument. Recently, Sparse method (Bobin, Sureau, and Starck 2015) was also proposed for component separation. Several other methods have been extended to work in the wavelet domain, or to explicitly use the sparsity approach. The next subsections review some of the methods for component separation.

3.3.1 Component Separation in the Pixel Domain

3.3.1.1 *Template Fitting*

This is the simplest method for foreground cleaning and having the foregrounds as part of the microwave sky, we can perform a fit of the template to a microwave sky data to analyse the foregrounds. Consider a template data to be of the form;

$$\tilde{\mathbf{y}}_c = \mathbf{y}_c - \sum_k \beta_k \mathbf{T}_k \quad (3.22)$$

where, β_k is the amplitude for each foreground template and it is obtained by minimizing $\tilde{\mathbf{y}}_c^T \mathbf{C}^{-1} \tilde{\mathbf{y}}_c$ such that $\mathbf{C} = \langle \tilde{\mathbf{y}}_c \tilde{\mathbf{y}}_c^T \rangle$ is the overall covariance matrix for the template-corrected data. Equation 3.22 therefore becomes;

$$\sum_k \mathbf{T}_k^T \mathbf{C}^{-1} \mathbf{T}_k \beta_k = \mathbf{T}_k^T \mathbf{C}^{-1} \mathbf{y}_c \quad (3.23)$$

The cross-correlation among the templates in equation 3.23 is given by $\mathbf{T}_k^T \mathbf{C}^{-1} \mathbf{T}_k$. Equation 3.23 holds in pixel or harmonic spaces. However, in pixel space the signal covariance matrix is large and not sparse, whilst in harmonic space, the signal covariance matrix is diagonal by considering the signal to be Gaussian.

Apart from the simplicity of this method where the statistical properties of the noise in the foreground-cleaned map are negligible, the template map may contain spatial information that is significant for the non-stationary and highly non-Gaussian emission distribution of the Galactic foregrounds. The main drawback in using this technique is that, it considers that the frequency dependence is independent of the position pf the sky, which in reality, is not fully satisfied. Another setback is that, invalid template model could introduce systematic errors and non-Gaussianities to the data. These disadvantages have made the WMAP team to employ a more robust technique, called the Internal Linear Combination (ILC) for their template fitting (Gold et al. 2011).

For a more detailed description of template fitting techniques, refer to (Dunkley et al. 2009; Kiyotomo 2014; Gorecki et al. 2014; Pforr, Maraston, and Tonini 2012; Doré et al. 2014).

3.3.1.2 Internal Linear Combination

The ILC is very useful when there is no prior information about the foregrounds (Tegmark and Efstathiou 1996) and in this case, very little assumption is made about the different components in the signal. The main component is assumed to have the same template in all the frequency bands and the observations are calibrated with respect to this component. The ILC model is presented as;

$$y_i(p) = s(p) + f_i(p) + n_i(p) \quad (3.24)$$

where, i is the frequency channels, $f_i(p)$ and $n_i(p)$ are the foreground and noise contributions in pixel p respectively. The expected CMB signal $s_i(p)$ we want to estimate from the data $y_i(p)$ becomes;

$$\hat{s}(p) = \sum_i w_i(p) y_i(p) \quad (3.25)$$

such that, the weights $w_i(p)$ maximize a certain benchmark about the reconstructed estimate $\hat{s}(p)$, whilst maintaining the component of interest unchanged.

Consider the weights are independent of p such that $\sum_i w_i = 1$, then equation 3.25 can be presented as;

$$\hat{s}(p) = s(p) + \sum_i w_i f_i(p) + \sum_i w_i n_i(p) \quad (3.26)$$

Minimizing the variance σ^2 from equation 3.26 we get;

$$\sigma^2 = \mathbf{w}^T \mathbf{C} \mathbf{w} \quad (3.27)$$

where, $C = \langle \mathbf{y} \mathbf{y}^T \rangle$ with \mathbf{y} and \mathbf{w} denoting vectors of elements y_i and w_i . Using the Lagrange multiplier method, w_i becomes;

$$w_i = \frac{\sum_j C_{ij}^{-1}}{\sum_{ij} C_{ij}^{-1}} \quad (3.28)$$

The ILC method minimizes the overall variance of the ILC map which implies that the weights are strongly restricted by regions close to the galactic plane where most of the foregrounds are limited. Therefore, the best linear combination for cleaning the CMB map from foregrounds and noise might be different from regions close to the galactic plane. To make it more robust, the map is decomposed into several regions and ILC is applied to them independently. This method is recognized as a foreground subtraction technique rather than a component separation method. The method has been applied to the WMAP data and has produced successful visualizations of the CMB anisotropies (Bennett et al. 2013; Gold et al. 2011; Bennett et al. 2003; Gold et al. 2009; Hinshaw et al. 2007)

3.3.1.3 *FastICA*

FastICA is a mixture model that takes the form;

$$\mathbf{y}^j = \mathbf{A}_k^j \mathbf{s}^k \quad (3.29)$$

where, the elements of \mathbf{y} are the observed intensity at frequency j , \mathbf{A} is the mixing matrix as before and the elements of \mathbf{s} are the signal with foregrounds and are considered to be independent. The technique is used to analyse a combination of independent non-Gaussian sources in a noiseless setting. The decomposition is done by maximizing the linearly combined stochastic variable:

$$\mathbf{z}^k = \mathbf{W}_j^k \mathbf{x}^j \quad (3.30)$$

If $\mathbf{W} = \mathbf{A}^{-1}$ then $\mathbf{z}^k = \mathbf{s}^k$. To determine the decomposition matrix \mathbf{W} we need to evaluate the function $g(\mathbf{z}^k)$ whose level is non-Gaussian. Any non-linear function should perform in the same principle, but in usually, kurtosis and neg-entropy are frequently adapted used.

Some of the applications of FastICA to CMB component separation problem are published by (Maino et al. 2007; Chapman et al. 2012; Wei 2015; Donzelli et al. 2006).

3.3.1.4 *Correlated Component Analysis*

The Correlated Component Analysis (CCA) method is a partially blind approach that measures the mixing matrix on sub-patches of the sky based on second-order statistics of the data. The independence of the sources are not assumed rather, adopts commonly used models for the sources to reduce the number of parameters estimated and exploits the spatial structure of the source maps. The spatial structure of the maps are measured from the covariance matrices at different shifts (τ, ψ) :

$$\mathbf{C}_d(\tau, \psi) = \mathbf{A} \mathbf{C}_s(\tau, \psi) \mathbf{A}^T + \mathbf{C}_n(\tau, \psi) \quad (3.31)$$

where, $\mathbf{C}_d(\tau, \psi)$ is estimated from the data and $\mathbf{C}_n(\tau, \psi)$ is the noise covariance matrices obtained from map-making noise estimations. Minimizing equation 3.31, we get;

$$\sum_{\tau, \psi} \| \mathbf{A} \mathbf{C}_s(\tau, \psi) \mathbf{A}^T - \{ \mathbf{C}_d(\tau, \psi) - \mathbf{C}_n(\tau, \psi) \} \| \quad (3.32)$$

Applying the Frobenius norm, we can estimate the mixing matrix and the free parameters of the source covariance matrix.

Chapter 4

INVESTIGATING INTENSITY MAPPING OBSERVATION WITH REALISTIC PRIMARY BEAM DISTORTION

Overview

This Chapter introduces us to Ray Tracing and EM Simulations which are the general techniques for generating complex beam patterns of an antenna. We then proposed a notional beam model for this research and compare it with the standard beam pattern simulations.

4.1 Primary Beam Modelling

Over the past few years, there have been numerous techniques and software packages for modelling the primary beam response of an antenna. Some of the well known beam pattern packages are the `cassbeam`¹ - Cassegrain antenna simulator (Brisken 2003) which works

¹<https://github.com/ratt-ru/cassbeam>

by a simple geometrical ray-tracing technique and the commercially available GRASP² and FEKO³ software suites which operate through sophisticated EM modelling techniques. The latter two options produce the most accurate results but are quite expensive in computational and commercial terms. Appendix A.1 briefly describes how the ray tracing technique is used to obtain accurate voltage patterns for realistic antenna models such as the effects of central blockage, feed support legs and deviations from axis-symmetry. The EM simulation of GRASP is also discussed in Chapter 6 and in this research, the technique is used to construct the SKA1-MID primary beams.

The purpose of this chapter is to study the observational effects of primary beam distortion. To do this, we develop a recipe for computing both an ideal beam pattern and a set of many perturbed patterns representing deformations of the antenna. These are technically achievable with GRASP or FEKO, but practically laborious for the purpose of this research where many perturbed patterns are essentially considered. Moreover, the study does not need a physical *precise* model of the KAT-7 primary beam, since future IM observations will not be carried out by KAT-7. KAT-7 is a notional example that is adopted for the purposes of this study. Therefore, what is rather needed is a relatively cheap way to compute ideal and perturbed beams, with perturbations that are representative of those seen in actual telescopes.

The GPU-accelerated OSKAR package use digital beamforming technique (Dulwich et al. 2009; Mort et al. 2010) to simulate primary beams of aperture arrays. It has the ability to include the following for each station beam response:

- (i) Introduce independent specification of pointing direction for each station or tile,
- (ii) Introduce apodisation weighting (this will modify the shape of the station beam),
- (iii) Introduce antenna element position and dipole orientation error and
- (iv) Introduce systematic and random element phase and gain errors.

²<http://www.ticra.com/products/software/grasp>

³<https://www.feko.info/product-detail/overview-of-feko>

The simulator is also capable of simulating interferometers (Mort et al. 2017; Sinclair et al. 2014) produced from large aperture arrays by utilising the Radio Interferometer Measurement Equation (RIME) (Hamaker, Bregman, and Sault 1996; Smirnov 2011) to generate the simulated visibilities. In general, this software is relatively ‘flexible’ to use for the scope of this Chapter compared to the previous softwares mentioned above.

Below, we show that OSKAR can be used to compute “dish-like” primary beams, by generating a geometric dipole distribution that mimics the aperture illumination function (AIF) of a dish. We stress that the resulting beam pattern is completely notional, and cannot be treated as a physically accurate model of the KAT-7 beam. It is, however, broadly representative of the dish beam. Furthermore, perturbations with respect to this ideal notional beam can be readily generated by perturbing the dipole distribution. The OSKAR approach gives us a practical way of generating such ideal and perturbed beams. As pointed out above, this is sufficient for the purposes of our work. Later in this section, we compare the primary beam perturbations produced by our approach with those seen in holographic measurements of JVLA antennas and show that the simulated perturbations are also broadly representative.

4.2 OSKAR Beam Model

In order to generate a “dish-like” primary beam model using OSKAR, we aim to mimic the AIF of a KAT-7-like dish by a 2D distribution of dipole positions. There are two important features of the AIF that we need to model: a tapering off towards the edge of the dish (due to the illumination pattern of the feed), and aperture blockage by the centrally-mounted feed and its four supporting struts. To simulate illumination tapering, we generate a random distribution of 2D positions with a density that tapers off towards the edges of the dish. This is achieved by computing a set of positions as $x_d = R \cos(\psi)$ and $y_d = R \sin(\psi)$, where ψ is drawn from a uniform random distribution over a circular medium as $[0, 2\pi]$, and R is randomly generated by computing the *inverse transform method* (ITM) to enable us to draw a 1D radial probability distribution f_X . The following algorithm describes the ITM used to draw random values from a cumulative distribution function (CDF), F_X of a known density f_X :

- (i) Find the quantile function F_X^{-1} .
- (ii) Generate a uniform random number u .
- (iii) Return the random number $x = F_X^{-1}(u)$.

This study assumed the density function to be the Generalized Normal distribution, which is also known as the Super Gaussian (Pogany and Nadarajah 2009; Decker 1994), such that for $X \sim N(\mu, \sigma^s)$, we have;

$$f_X(x) = \frac{\sqrt{s}}{2\sigma\Gamma(\frac{1}{s})} \exp\left(-\left|\frac{x-\mu}{\sigma\sqrt{2}}\right|^s\right) \quad (4.1)$$

where, $-\infty < x < \infty$ is a random value, $-\infty < \mu < \infty$ is the mean, $\sigma > 0$ is the standard deviation, $s > 0$ is the peak factor and the gamma function is defined as $\Gamma(a, x) = \int_x^\infty t^{a-1} e^{-t} dt$.

The CDF of equation (4.1) is derived from the error functions such that the error function $erf(z)$ is defined by;

$$erf(z) = \frac{2}{\sqrt{\pi}} \int_0^z \exp(-t^2) dt \quad (4.2a)$$

$$= \frac{1}{\sqrt{\pi}} \gamma(1/2, z^2) \quad (4.2b)$$

and that of the complementary error function $erfc(z)$ is defined by;

$$erfc(z) = \frac{2}{\sqrt{\pi}} \int_z^\infty \exp(-t^2) dt \quad (4.3a)$$

$$= \frac{1}{\sqrt{\pi}} \Gamma(1/2, z^2) \quad (4.3b)$$

$$= 1 - erf(z) \quad (4.3c)$$

From equation (4.3), we can rewrite equation (4.2) as;

$$\operatorname{erf}(z) = 1 - \frac{1}{\sqrt{\pi}} \Gamma(1/2, z^2) \quad (4.4)$$

If we put $s = 2$ in equation (4.1), the normal distribution is produced and the respective CDF becomes;

$$\int_{-\infty}^x f(x'|\mu, \sigma^2) = \frac{1}{2} \left[1 + \operatorname{erf} \left(\frac{x' - \mu}{\sigma\sqrt{2}} \right) \right] \quad (4.5)$$

From equation (4.4) we can rewrite equation (4.5) as;

$$F_2(x) = 1 - \frac{1}{2\sqrt{\pi}} \Gamma \left(\frac{1}{2}, \frac{x - \mu}{\sigma\sqrt{2}} \right) \quad (4.6)$$

Extending equation (4.6) into the general form in equation (4.1), we get;

$$F_s(x) = \begin{cases} \frac{\Gamma(\frac{1}{s}, \{\frac{x-\mu}{\sigma\sqrt{2}}\}^s)}{2\Gamma(\frac{1}{s})}, & \text{if } x \leq \mu \\ 1 - \frac{\Gamma(\frac{1}{s}, \{\frac{x-\mu}{\sigma\sqrt{2}}\}^s)}{2\Gamma(\frac{1}{s})}, & \text{if } x > \mu \end{cases} \quad (4.7)$$

Using equation (4.7) in the ITM, we can now draw a random number u from a uniform distribution over $[0, 1]$ and then compute the sample R as $R = |F^{-1}(u)|$. This results in a “flat-top Gaussian” radial density distribution as shown in Fig. 4.1, left. The parameters of the Super Gaussian distribution, σ and s control the width of the distribution and the aggressiveness of the taper. The values adopted in this work to produce the radial distribution in the figure are $\sigma = 0.82$ and $s = 12.0$.

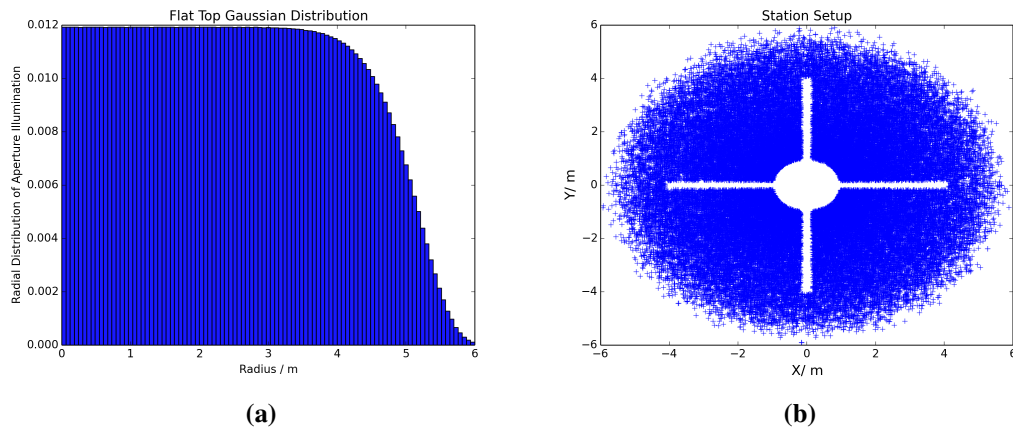


Figure 4.1: (a) The “flat-top Gaussian” radial distribution of dipole positions, mimicking a realistic aperture illumination where the dipoles get less dense towards the edge of the dish and (b) the resulting 2D dipole distribution with a mask applied to mimic aperture blockage ensures effective illumination and avoids tapering off.

We imitate the aperture blockage by simply masking the 2D positions. This ultimately results in the dipole distribution shown in Fig. 4.1, right. This dipole distribution is then fed into OSKAR as the “station layout”. For a given set of observational parameters (in particular, pointing at zenith), OSKAR then computes the station primary beam response. The resulting *Jones matrix* elements are shown in Fig. 4.2. Note how the beam pattern is broadly similar to that expected from a prime-focus dish. In particular, the first side-lobe shows the four-fold symmetry caused by the strut blockage. The presence of the phase component in Fig. 4.2 clearly shows that the so-called ideal beam is not that perfect since we are randomly placing the dipoles in the KAT-7 dish-like form, hence, the nominal X and Y dipoles are not directly orthogonal. In effect, we get the maximum $rmse \approx 0.10\%$ perturbed inaccuracies on the dish surface as reported in Fig. 4.3.

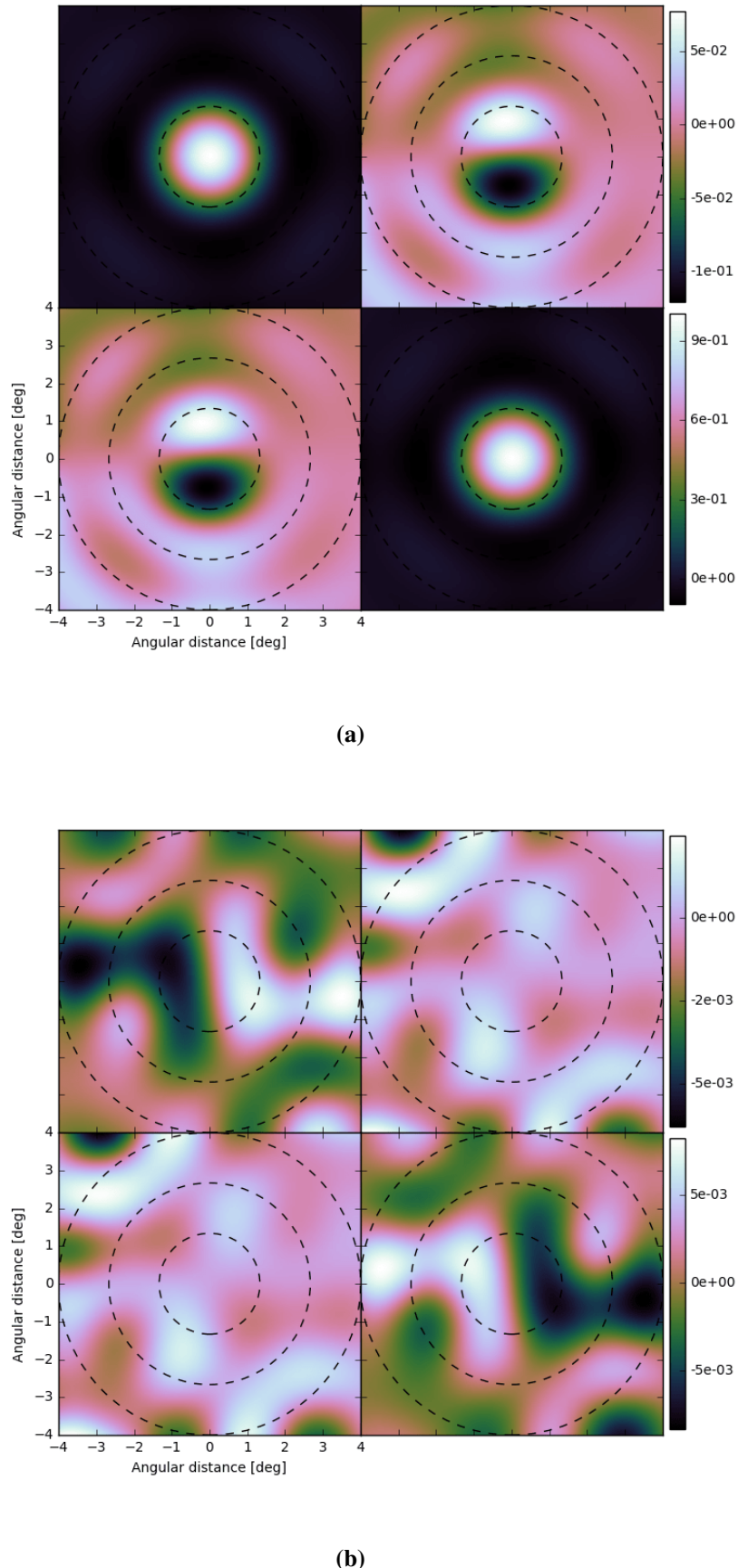


Figure 4.2: Jones matrix representation of the KAT-7-like beams produced by OSKAR and shown at 1 GHz: (a) real part (b) imaginary part. The intensity of the imaginary parts increases with fewer dipoles and becomes very less when more dipoles are used.

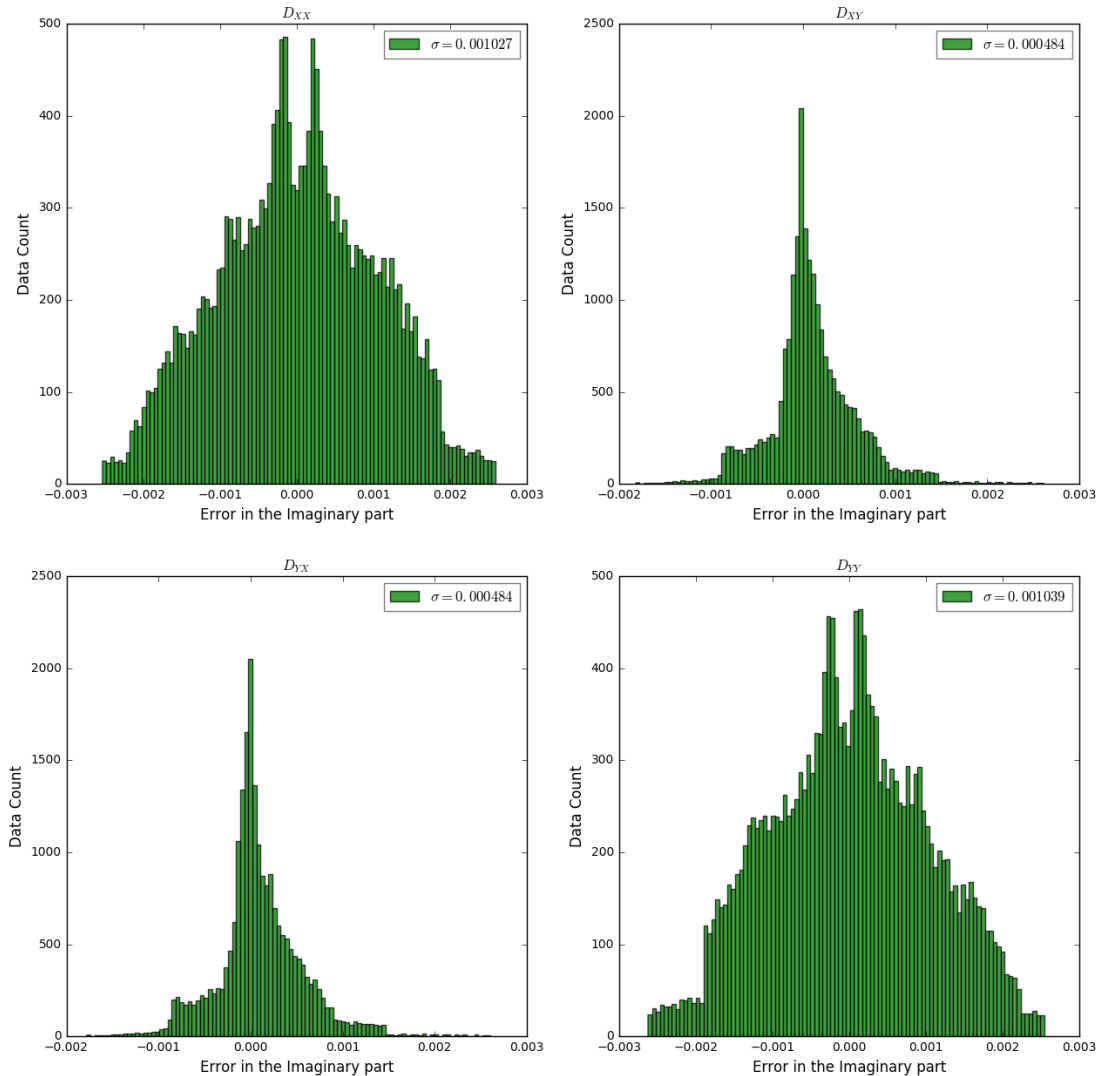


Figure 4.3: Histogram plots of the imaginary components in Fig. 4.2 showing the distribution of inaccuracies on the KAT-7 dish-like surface.

4.2.1 Jones and Mueller matrices

The Jones (Jones 1948; Jones 1942) formalism, originally formulated to describe optical polarization, was adapted to radio interferometry by Hamaker, Bregman, and Sault 1996 and extended to direction-dependent effects by Smirnov 2011. Here we use the derivations of the latter two works.

An electromagnetic plane wave propagating along axis z can be described, at any point in space and time, by two complex amplitudes, e_x and e_y . Conventionally, we arrange these into a column vector, $e = [e_x, e_y]^T$. A single-dish observation aims to measure the pairwise coherencies of these amplitudes:

$$x = \begin{bmatrix} \langle e_x e_x^* \rangle \\ \langle e_x e_y^* \rangle \\ \langle e_y e_x^* \rangle \\ \langle e_y e_y^* \rangle \end{bmatrix} = \langle e \otimes e^* \rangle, \quad (4.8)$$

where $\langle \cdot \rangle$ represents the average over a time/frequency interval, and \otimes is the outer (or Kronecker) product operator. From these measured coherencies, the Stokes parameters $IQUV$ (written as a column vector s) may be derived, by definition, as (Born and Wolf 1980):

$$s = \begin{bmatrix} I \\ Q \\ U \\ V \end{bmatrix} = \begin{bmatrix} \langle e_x e_x^* \rangle + \langle e_y e_y^* \rangle \\ \langle e_x e_x^* \rangle - \langle e_y e_y^* \rangle \\ \langle e_x e_y^* \rangle + \langle e_y e_x^* \rangle \\ -\imath(\langle e_x e_y^* \rangle - \langle e_y e_x^* \rangle) \end{bmatrix} \quad (4.9)$$

We can rewrite this in terms of a 4×4 conversion matrix S^{-1} as⁴:

$$s = \begin{bmatrix} 1 & 0 & 0 & 1 \\ 1 & 0 & 0 & -1 \\ 0 & 1 & 1 & 0 \\ 0 & -\imath & \imath & 0 \end{bmatrix} x = S^{-1}x. \quad (4.10)$$

What the instrument actually measures is a set of pairwise correlations between two voltages induced by the EM field on two orthogonal mode feeds, v_a and v_b . The Jones formalism assumes that these are linearly related to the EM field (i.e. that all signal propagation effects are linear). This can be written as $v = Je$, where v is a column vector of the two voltages,

⁴This follows Smirnov 2011 in defining S as the conversion matrix between Stokes vectors and coherency vectors, $v = Ss$. Conversely, S^{-1} operates in the opposite direction. Note that Hamaker, Bregman, and Sault 1996 use T to refer to S^{-1} .

and the 2×2 *Jones matrix* J describes signal propagation. The *measured* coherency x' can then be written as

$$x' = \langle v \otimes v^* \rangle = (J \otimes J^*) \langle e \otimes e^* \rangle = (J \otimes J^*)x, \quad (4.11)$$

and the measured Stokes parameter vector s' relates to the original Stokes vector via the so-called *Mueller matrix* M :

$$s' = Ms = S^{-1}(J \otimes J^*)Ss \quad (4.12)$$

For the purposes of this work, we ignore all propagation effects except the primary beam. In the context of this paper, the Mueller matrix refers to the Mueller matrix of the primary beam. This matrix is direction-dependent (i.e. each direction of arrival will have its own matrix associated with it). The total Stokes flux measured by a single dish observation is then an integration over the FoV:

$$s'_{\text{tot}} = \iint_{lm} M(l, m) s(l, m) dl dm, \quad (4.13)$$

where the integration is, in principle, over the entire celestial sphere, but in practice, since the Mueller matrix becomes negligibly small outside of a certain FoV, it can be replaced by a 2D integral over the tangent plane lm .

The Mueller matrix $M(l, m)$ corresponding to our KAT-7-like dish (Fig. 4.4a) can be derived from the Jones matrix $J(l, m)$ of Fig. 4.2. Note the physical meaning of the matrix elements J in equation (4.12) as displayed in Fig. 4.2. The on-diagonal terms of the Jones matrix describe the sensitivity of each feed, as a function of direction, to its matched EM field component. The off-diagonal terms describe leakage, i.e. the sensitivity of the feed to the nominally orthogonal EM field component. This leakage is due to mechanical and electronic

imperfections in the antennas and feeds. The next subsection presents a mathematical model of the Mueller matrix derived in terms of Jones matrices.

4.2.1.1 Derivation of Mueller Matrix

The Mueller matrix gives a detailed characterisation of a polarisation element (Bass et al. 2009) such that the polarisation change is described in terms of intensities S_k . Therefore, following (Goldstein 2003), we decompose each element of J_{ij} in equation (4.12) into further 2×2 matrices to get:

$$J_{ij} = \frac{1}{2} \sum_{k=0}^3 \sigma_k \zeta_k \quad (4.14)$$

where,

$$\sigma_0 = \begin{pmatrix} 1 & 0 \\ 0 & 1 \end{pmatrix}, \quad \sigma_1 = \begin{pmatrix} 0 & 1 \\ 1 & 0 \end{pmatrix}$$

$$\sigma_2 = \begin{pmatrix} 0 & -i \\ i & 0 \end{pmatrix}, \quad \sigma_3 = \begin{pmatrix} 1 & 0 \\ 0 & -1 \end{pmatrix}$$

The matrices $\{\sigma_0, \sigma_1, \sigma_2, \sigma_3\}$ provide a basis for the determination of the Mueller matrix M_{ij} . The matrix σ_0 is an identity matrix, σ_1, σ_2 and σ_3 are the 3 Pauli matrices which describe the propagation behaviour of the signal. ζ_k is associated to Pauli matrices:

$$[\zeta_k]_\alpha = [\sigma_k] \quad (4.15)$$

Hence, for $k = 0$,

$$\sigma_0 = \begin{pmatrix} 1 & 0 \\ 0 & 1 \end{pmatrix} = \begin{pmatrix} \zeta_{0,0} & \zeta_{0,1} \\ \zeta_{0,3} & \zeta_{0,4} \end{pmatrix} \quad (4.16)$$

We can deduce from equation (4.16) that;

$$\zeta_0 = \begin{pmatrix} \zeta_{0,0} \\ \zeta_{0,1} \\ \zeta_{0,2} \\ \zeta_{0,3} \end{pmatrix} = \begin{pmatrix} 1 \\ 0 \\ 0 \\ 1 \end{pmatrix} \quad (4.17)$$

Similarly, for $k = 1, 2$ or 3 , we get;

$$\zeta_1 = \begin{pmatrix} 1 \\ 0 \\ 0 \\ -1 \end{pmatrix}, \quad \zeta_2 = \begin{pmatrix} 0 \\ 1 \\ 1 \\ 0 \end{pmatrix}, \quad \zeta_3 = \begin{pmatrix} 0 \\ -i \\ i \\ 0 \end{pmatrix} \quad (4.18)$$

Normalizing equations (4.17) and (4.18) we get;

$$\mathbf{A} = \frac{1}{2} \begin{pmatrix} 1 & 1 & 0 & 0 \\ 0 & 0 & 1 & -i \\ 0 & 0 & 1 & i \\ 1 & -1 & 0 & 0 \end{pmatrix} \quad (4.19)$$

The Mueller matrix M_{ij} in component form, can be expressed as;

$$M_{ij} = (\mathbf{A}^*)^{-1} (\mathbf{J}_{ij} \otimes \mathbf{J}_{ij}^*) \mathbf{A}^* \quad (4.20)$$

where, the symbol \otimes , represents the Kronecker product. Considering $\mathbf{U} = (\mathbf{A}^*)^{-1} = \mathbf{A}^H$, we get;

$$M_{ij} = \mathbf{U} (\mathbf{J}_{ij} \otimes \mathbf{J}_{ij}^*) \mathbf{U}^{-1} \quad (4.21)$$

where, the notation H , represents Hermitian transpose such that;

$$\mathbf{U} = \frac{1}{2} \begin{pmatrix} 1 & 0 & 0 & 1 \\ 1 & 0 & 0 & -1 \\ 0 & 1 & 1 & 0 \\ 0 & -i & i & 0 \end{pmatrix}$$

characterises the propagation effects of the measured signals.

The Jones matrices in equation (4.21) can be expanded as;

$$J \otimes J^* = \begin{pmatrix} J_{00} J_{00}^* & J_{00} J_{01}^* & J_{01} J_{00}^* & J_{01} J_{01}^* \\ J_{00} J_{10}^* & J_{00} J_{11}^* & J_{01} J_{10}^* & J_{01} J_{11}^* \\ J_{10} J_{00}^* & J_{10} J_{01}^* & J_{11} J_{00}^* & J_{11} J_{01}^* \\ J_{10} J_{10}^* & J_{10} J_{11}^* & J_{11} J_{10}^* & J_{11} J_{11}^* \end{pmatrix} \quad (4.22)$$

If we substitute equation (4.22) into (4.21), we can then expand the Mueller matrix elements in terms of Jones matrix elements:

$$m_{II} = (J_{00}J_{00}^* + J_{01}J_{01}^* + J_{10}J_{10}^* + J_{11}J_{11}^*)/2 \quad (4.23a)$$

$$m_{IQ} = (J_{00}J_{00}^* - J_{01}J_{01}^* + J_{10}J_{10}^* - J_{11}J_{11}^*)/2 \quad (4.23b)$$

$$m_{IU} = (J_{00}J_{01}^* + J_{01}J_{00}^* + J_{10}J_{11}^* + J_{11}J_{10}^*)/2 \quad (4.23c)$$

$$m_{IV} = i(J_{00}J_{01}^* + J_{10}J_{11}^* - J_{01}J_{00}^* - J_{11}J_{10}^*)/2 \quad (4.23d)$$

$$m_{QI} = (J_{00}J_{00}^* + J_{01}J_{01}^* - J_{10}J_{10}^* - J_{11}J_{11}^*)/2 \quad (4.23e)$$

$$m_{QQ} = (J_{00}J_{00}^* - J_{01}J_{01}^* - J_{10}J_{10}^* + J_{11}J_{11}^*)/2 \quad (4.23f)$$

$$m_{QU} = (J_{00}J_{01}^* + J_{01}J_{00}^* - J_{10}J_{11}^* - J_{11}J_{10}^*)/2 \quad (4.23g)$$

$$m_{QV} = i(J_{00}J_{01}^* - J_{10}J_{11}^* - J_{01}J_{00}^* - J_{11}J_{10}^*)/2 \quad (4.23h)$$

$$m_{UI} = (J_{00}J_{10}^* + J_{10}J_{00}^* + J_{01}J_{11}^* + J_{11}J_{01}^*)/2 \quad (4.23i)$$

$$m_{UQ} = (J_{00}J_{01}^* - J_{01}J_{00}^* + J_{10}J_{11}^* + J_{11}J_{10}^*)/2 \quad (4.23j)$$

$$m_{UU} = (J_{00}J_{11}^* + J_{11}J_{00}^* + J_{01}J_{10}^* + J_{10}J_{01}^*)/2 \quad (4.23k)$$

$$m_{UV} = i(J_{00}J_{11}^* + J_{10}J_{01}^* - J_{11}J_{00}^* - J_{01}J_{10}^*)/2 \quad (4.23l)$$

$$m_{VI} = i(-J_{00}J_{10}^* + J_{10}J_{00}^* - J_{01}J_{11}^* + J_{11}J_{01}^*)/2 \quad (4.23m)$$

$$m_{VQ} = i(-J_{00}J_{10}^* + J_{10}J_{00}^* + J_{01}J_{11}^* - J_{11}J_{01}^*)/2 \quad (4.23n)$$

$$m_{VU} = i(-J_{00}J_{11}^* + J_{11}J_{00}^* - J_{01}J_{10}^* + J_{10}J_{01}^*)/2 \quad (4.23o)$$

$$m_{VV} = (J_{00}J_{11}^* - J_{10}J_{01}^* + J_{11}J_{00}^* - J_{01}J_{10}^*)/2 \quad (4.23p)$$

If we substitute the elements in equation (4.23) into equation (4.12), we get:

$$\begin{pmatrix} S'_I \\ S'_Q \\ S'_U \\ S'_V \end{pmatrix} = \begin{pmatrix} m_{II} & m_{IQ} & m_{IU} & m_{IV} \\ m_{QI} & m_{QQ} & m_{QU} & m_{QV} \\ m_{UI} & m_{UQ} & m_{UU} & m_{UV} \\ m_{VI} & m_{VQ} & m_{VU} & m_{VV} \end{pmatrix} \begin{pmatrix} S_I \\ S_Q \\ S_U \\ S_V \end{pmatrix} \quad (4.24)$$

The elements M_{ij} in equation (4.24) represent the complete beams in Fig. 4.4. The diagonal

terms of the Mueller matrix describe the sensitivity of the measured Stokes $IQUV$ components to their true counterparts, as a function of direction. The off-diagonal terms describe spurious leakage between the measured Stokes components. We can schematically write this as;

$$M = \begin{bmatrix} I \rightarrow I' & Q \rightarrow I' & U \rightarrow I' & V \rightarrow I' \\ I \rightarrow Q' & Q \rightarrow Q' & U \rightarrow Q' & V \rightarrow Q' \\ I \rightarrow U' & Q \rightarrow U' & U \rightarrow U' & V \rightarrow U' \\ I \rightarrow V' & Q \rightarrow V' & U \rightarrow V' & V \rightarrow V' \end{bmatrix}$$

Fig. 4.4a displays the KAT-7-like modelled beams produced from OSKAR in Mueller matrix form. For example, the elements $I \rightarrow Q, U, V$ in the 4×4 images describe how much of Stokes I intensity leaks into the polarisation components Q, U, V while, $Q \leftrightarrow U, Q \leftrightarrow V, U \leftrightarrow V$ are the cross-polarisation leakage terms. Section 4.2.2 describes further how the OSKAR package is used to introduce errors in the modelled beams to produce beam distortion.

4.2.2 Primary Beam Perturbation

The modelled beams produced in this chapter are corrupted with two kinds of errors. The first error type is the introduction of systematic and time-variable gain and phase errors. The nominal purpose of this in OSKAR is to simulate per-element gain and phase error before the beamformer, so that the beam-forming weight B^w , for a particular beam direction (θ_{bm}, ϕ_{bm}) , with dipole position (x, y, z) and time t becomes;

$$B^w(u) = B_{geo}^w(u)(G_0 + G_{error}) \exp(j[\phi_0 + \phi_{error}]) \quad (4.25)$$

where $u = (\theta_{bm}, \phi_{bm}, x, y, z, t)$, G_{error} and ϕ_{error} are pseudo-random values at each time-step t using a Gaussian distribution with standard deviations G_{std} and ϕ_{std} respectively. The complex multiplicative factor applied to each element is denoted by the parameters Gain G_0 and phase ϕ_0 respectively. This complex factor joins with the geometric beam-forming weight B_{geo}^w to produce the array factor to evaluate the station beam at each source position. For the purpose of our “disk-like” simulation, we introduced 5° phase error and 10% gain error into the beam-forming weight to distort the beams as shown in Appendix A.1a.

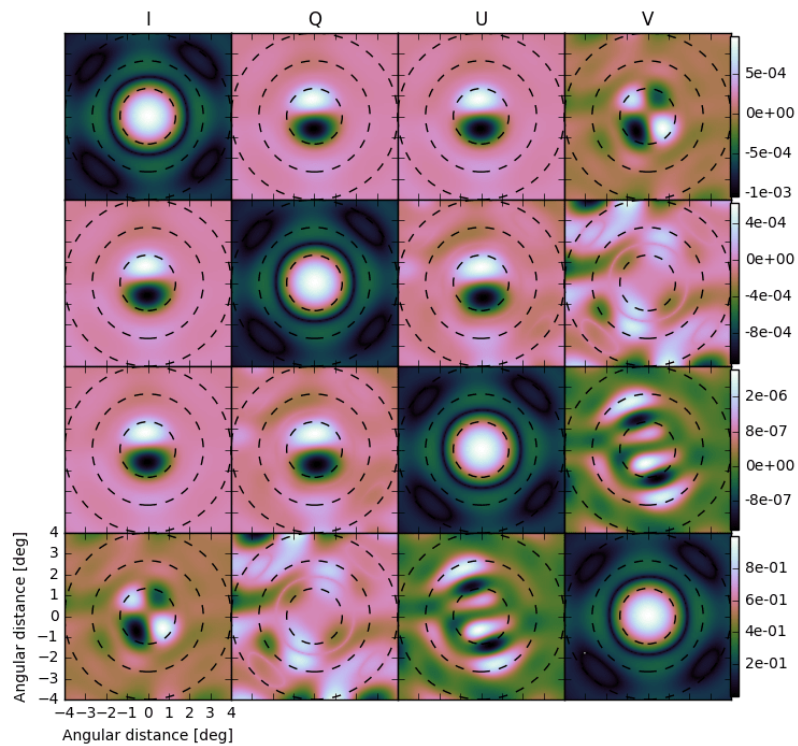
These sort of errors represent imperfections in the parabolic reflector surface (which, in real life, result in amplitude and phase errors over the aperture). The second error introduced is to uniformly change the orientation of the dipoles to create systematic error feed angle displacement as presented in Appendix A.1b. Figs. 4.4b and 4.4c show the beam errors produced by computing the differences between the true modelled beams in Fig. 4.4a and the two distorted beams in Appendices A.1a and A.1b respectively. The on-diagonal components of these beam errors represent the residual leakages and the off-diagonals show the residual systematic leakages. The maximum residual leakages produced in Figs. 4.4b and 4.4c are $\simeq 20\%$ and 10% respectively.

In order to see whether the level of beam distortion introduced in this manner is realistic, we compare the beam patterns obtained via holography measurements of two different JVLA dishes as presented in Appendices A.2a and A.2b. The measurement technique employed in producing these beams is based on the EVLA Memo (Perley and al. 2015) which consists of the utilisation of the Fourier transform relation between the complex far-field (i.e. amplitude and phase) radiation pattern of an antenna $\chi(u, v)$ and the complex aperture distribution $\zeta(l, m)$:

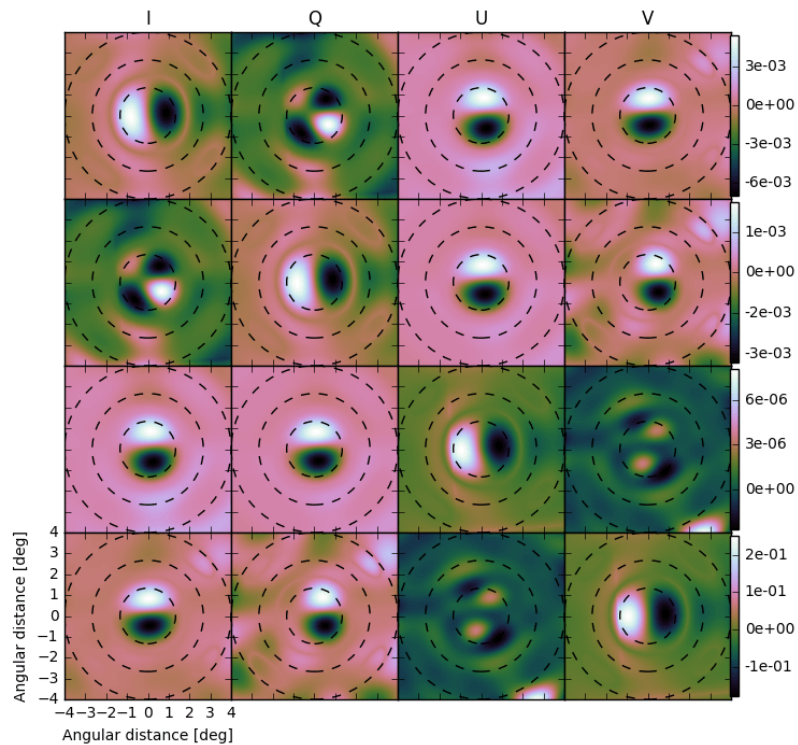
$$\chi(u, v) = \iint_{-\infty}^{+\infty} \zeta(l, m) \exp\{i2\pi(lu + mv)\} dl dm \quad (4.26)$$

where $u = x/\lambda$ and $v = y/\lambda$ denote the rectilinear coordinates in wavelength, in the aperture plane. The coordinates (l, m) are the direction cosine with respect to the aperture plane. The difference between the two holography measurements Fig. 4.4d corresponds to the real-life differences between the primary beam patterns of two nominally identical dishes. Note how these beam errors give a maximum residual leakage of $\simeq 10\%$. This demonstrates that our beam distortion procedure, using the error values we have adopted, results in physically realistic primary beam distortion levels.

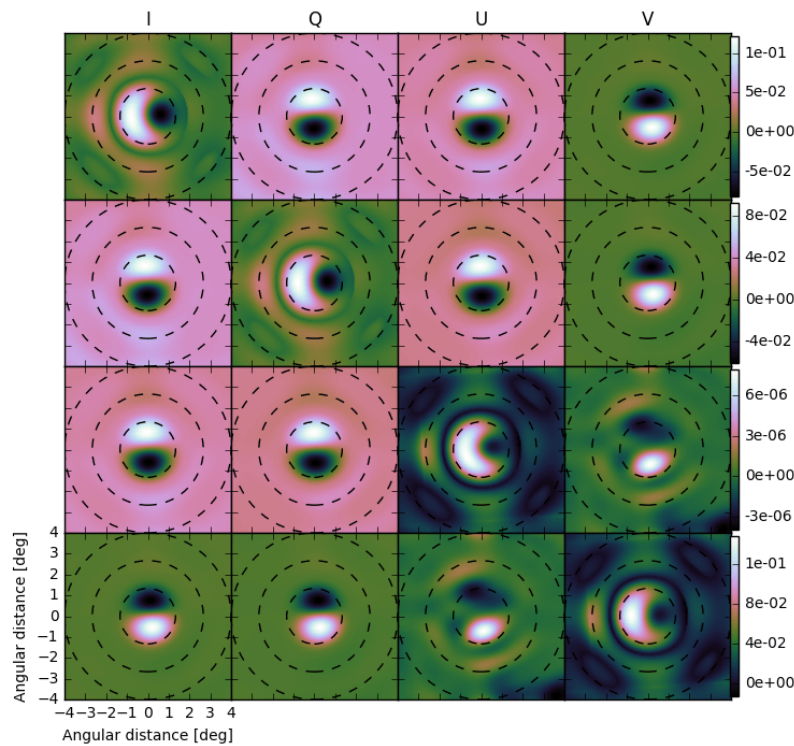
Having thus armed ourselves with an instrumental model, we now proceed to discuss the nature of our simulated sky.



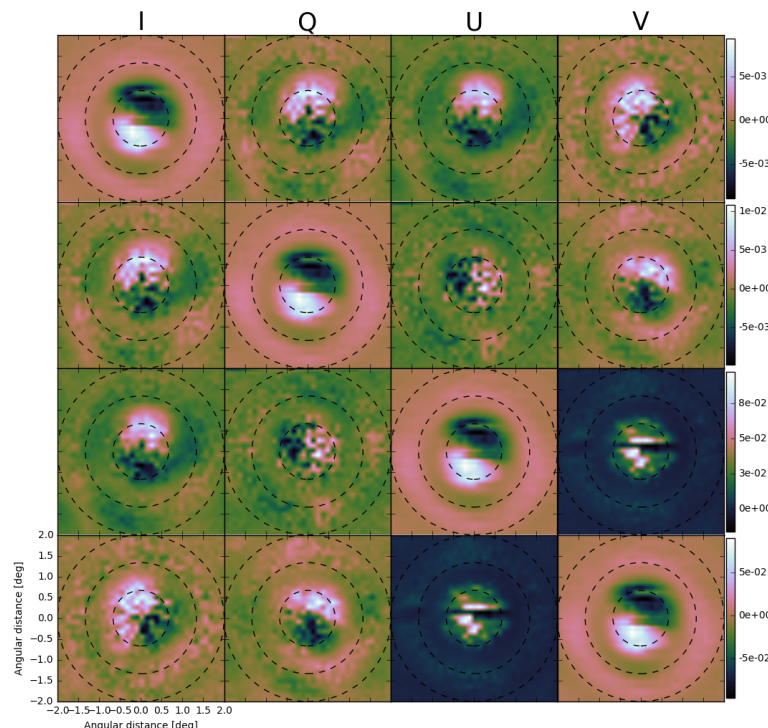
(a) 4×4 images of KAT-7 uncorrupted OSKAR beams.



(b) Difference between the uncorrupted OSKAR beams in Fig. 4.4a and the gain and phase error beams in appendix A.1a



(c) Difference between uncorrupted OSKAR beams in Fig. 4.4a and the dipole orientation error beams in appendix A.1b.



(d) Difference between JVLA holography measured beams in Appendices A.2a and A.2b.

Figure 4.4: Mueller matrix representations of full polarisation beams produced at 1 GHz

4.3 Simulation

The synchrotron emission from the Galaxy dominates at low microwave frequencies ($\lesssim 30\text{GHz}$), whilst that of thermal dust emission is at higher frequencies ($\lesssim 70\text{GHz}$). Between these two components in frequency, lies the thermal free-free and non-thermal dust emissions, which are formed as a result of spinning dust grains (Bennett et al. 1996). Detailed discussions on the components of the Galactic foregrounds, paying particular attention to their contributions to the polarisation measurements can be obtained from (Alonso et al. 2015; Kiyotomo 2014; Jelić et al. 2010; Santos et al. 2015a; Wolz et al. 2014).

In this work, the scheme used to simulate the full-sky polarisation maps as presented in Fig. 4.5 is fully described in Appendix D of Shaw et al. 2015, where they basically produce a large-scale base map by extrapolating the Haslam map (Loeb and Wyithe 2008) with a spectral index map from (Miville-Deschénes et al. 2008) and then randomly generate maps that add in fluctuations in frequency and on small angular scales. The smoothed synchrotron maps in Fig. 4.5 are represented by a sample of Hierarchical Equal Area isoLatitude Pixelation (HEALPix⁵) (Górski et al. 2005) of the sphere at a resolution of $N_{side} = 512$. Other techniques for simulating full-sky radio emission are presented by (de Oliveira-Costa et al. 2008; Geil, Gaensler, and Wyithe 2011; Jelić et al. 2008; The Polarbear Collaboration: P. A. R. Ade et al. 2014; Tucci et al. 2002). This study also considered the synchrotron emissions to be intrinsically linearly polarised and therefore, ignored the Stokes V part in Fig. 4.5 and all other V terms in the full polarisation beams discussed in Section ??.

⁵<http://healpix.sourceforge.net/>

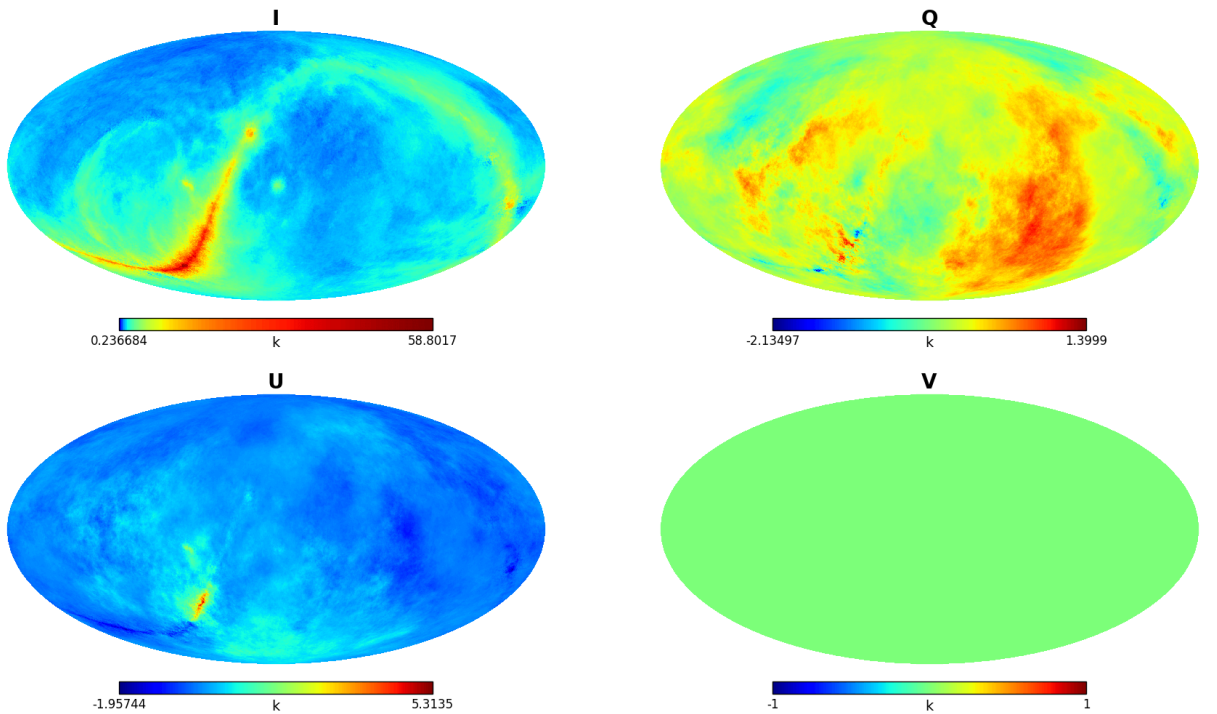


Figure 4.5: 1000 MHz full-sky synchrotron maps simulated by using m -mode formalism. These synchrotron maps characterize the full-sky polarisation maps for our low resolution simulated observations and are presented here in the mollweide projection form defined by equatorial coordinates in terms of Stokes parameters I, Q, U and V .

4.3.1 Full-sky Convolution

Convolution is a mathematical operation that interpolates two functions ψ_1 and ψ_2 to produce a third function χ that is typically viewed as a modification of one of the original functions. Consider $C_v(x)$ to be the convolution of $H_1(x)$ with $H_2(x)$, then its Fourier pair $\chi(\nu)$, is the product of $\psi_1(\nu)$ and $\psi_2(\nu)$ which are the Fourier pairs of $H_1(x)$ and $H_2(x)$ respectively. Thus,

$$H_1(x) \otimes H_2(x) \rightleftharpoons \psi_1(\nu) \cdot \psi_2(\nu) \quad (4.27)$$

where, the symbol \otimes denotes the convolution operator. By definition,

$$\begin{aligned} C_v(x) &= H_1(x) \otimes H_2(x) \\ &= \int_{-\infty}^{\infty} H_1(x') H_2(x - x') dx \end{aligned} \quad (4.28)$$

Taking the Fourier transform of both sides in equation (4.28), we get;

$$\begin{aligned}\chi(\nu) &= \int_{-\infty}^{\infty} C_v(x) e^{-2\pi j \nu x} dx \\ &= \int_{-\infty}^{\infty} \int_{-\infty}^{\infty} H_1(x') H_2(x - x') e^{-2\pi j \nu x} dx' dx\end{aligned}\quad (4.29)$$

Let $y = x - x' \Rightarrow dy = dx$

$$\chi(\nu) = \int_{-\infty}^{\infty} \int_{-\infty}^{\infty} H_1(x') H_2(y) e^{-2\pi j \nu (x' + y)} dx' dy \quad (4.30)$$

Equation (4.30) can therefore be separated to give

$$\begin{aligned}\chi(\nu) &= \int_{-\infty}^{\infty} H_1(x') e^{-2\pi j \nu x'} dx' \cdot \int_{-\infty}^{\infty} H_2(y) e^{-2\pi j \nu y} dy \\ &= \psi_1(\nu) \cdot \psi_1(\nu)\end{aligned}\quad (4.31)$$

Expressing the general definition in equation (4.31) into 2D discrete form, we have;

$$\begin{aligned}\chi(\nu_1, \nu_2) &= H_1(\nu_1, \nu_2) \otimes H_2(\nu_1, \nu_2) \\ &= \sum_{i=-\infty}^{\infty} \sum_{j=-\infty}^{\infty} H_1(i - \nu_1, j - \nu_2) H_2(i, j)\end{aligned}\quad (4.32)$$

In equation (4.32), the values $\chi(\nu_1, \nu_2)$ of the discrete function χ for any particular (ν_1, ν_2) follows by multiplying each value $H_2(i, j)$ of the discrete function H_2 with a kernel function $H_1(i - \nu_1, j - \nu_2)$ between a particular (ν_1, ν_2) and varying (i, j) where, $(-\infty < i, j < +\infty)$. Thus, each value $\chi(\nu_1, \nu_2)$ of the function χ is a weighted mean of the values $H_2(i, j)$ with weights $H_1(i - \nu_1, j - \nu_2)$ defined by the function H_1 . In this chapter, we apply similar technique to simulate the foreground of the sky.

To perform an IM experiment, the radio telescope(s) is pointed at different patches of the sky so that the instrument can measure the overall intensity emerging from patches from the autocorrelation of the radio signal, as a function of frequency. In order to emulate this observation technique in our IM simulation, the discrete convolution in equation (4.33) is used to measure the intensities of the full sky synchrotron maps in Fig. 4.5. Let (θ, ϕ) denote the celestial coordinates of the foregrounds of the sky such that, B are the fully polarised

beams and f_{sky} are the foregrounds of the sky. We can then model the convolved foregrounds to be:

$$\begin{aligned} F^{conv}(\theta, \phi) &= B(\theta, \phi) \otimes f_{sky}(\theta, \phi) \\ &= \sum_{(\theta', \phi') = \lfloor (\theta, \phi) \rfloor} B(\theta' - \theta, \phi' - \phi) \cdot f_{sky}(\theta', \phi') \end{aligned} \quad (4.33)$$

where $(\theta', \phi') \leq npix$ and the symbol $\lfloor \cdot \rfloor$ denotes the nearest pixels. The measured foreground pixel values $F^{conv}(\theta, \phi)$ of the discrete function F^{conv} for any particular (θ, ϕ) follows by multiplying each foreground pixel value $f_{sky}(\theta, \phi)$ of the discrete function f_{sky} with a beam $B(\theta' - \theta, \phi' - \phi)$ between a particular (θ', ϕ') and varying (θ, ϕ) . Thus, each pixel value $F^{conv}(\theta, \phi)$ of the function F^{conv} is a weighted mean of the pixel values $f_{sky}(\theta, \phi)$ with weights $B(\theta' - \theta, \phi' - \phi)$ defined by the function B . If we take the modelled beams B in Fig. 4.4a to convolve the full-sky polarisation maps (f_{sky}) in Fig. 4.5, we obtain the convolved maps F^{conv} in Fig. 4.6. The same approach is repeated using the distorted beams in Appendices A.1a and A.1b and also, the holography measured beams in Appendices A.2a and A.2b to produce their respective convolved maps. The original spatial distributions of the foregrounds in Fig. 4.5 are clearly maintained in the diagonals of the convolved maps as shown in Fig. 4.6. This happens when we simulate the full-sky maps with the gain terms in the diagonals of our beams.

In IM experiments, what is actually interested in, is to measure the total intensity of a signal. Therefore, in section 4.3.2, we present a mathematical model of the convolved power spectrum using the angular power spectrum to describe the spatial distribution of the measured foregrounds in a spherical harmonic domain.

4.3.2 Angular Power Spectrum

In CMB studies (Abitbol, Hill, and Johnson 2016; Krachmalnicoff et al. 2016; Wolz et al. 2015; Souradeep, Saha, and Jain 2006; Saha, Jain, and Souradeep 2006; White 1998), it is a common practice to characterize the distribution of flux in a sphere with the angular power spectrum. The same approach is employed in this project to describe the diffuse foreground

intensity over spherical harmonics $Y_{l,m}$.

Consider the foreground of the sky is emitted by our own galaxy or the distribution galaxies emitting 21-cm with an intensity equivalent to $T(\hat{\sigma})$. We can measure the total source emission temperature $T(\hat{\sigma})$, in each sky pixel and represent the distribution as an expansion in 2D spherical harmonics:

$$T(\hat{\sigma}) = \sum_{l=0}^{\infty} \sum_{m=-l}^{l} a_{lm} Y_{lm}(\hat{\sigma}) \quad (4.34)$$

where $\hat{\sigma} \equiv (\psi, \xi)$ is the unit vector in some direction in the sky and $Y_{lm}(\hat{\sigma})$ are the spherical harmonic functions evaluated in the direction $\hat{\sigma}$ such that, they form a complete orthonormal set on the unit sphere and can be expressed as;

$$Y_{lm}(\psi, \xi) = (-1)^m \sqrt{\frac{2l+1}{4\pi} \frac{(l-m)!}{(l+m)!}} P_l^m(\cos \psi) e^{im\xi} \quad (4.35)$$

In equation (4.35), the indices $l = 0, \dots, \infty$ and $-l < m < l$ with P_l^m denoting the Legendre polynomials. l is known as the multipole which denotes a given angular scale γ in the sky, where $\gamma \simeq 180^\circ/l$. The coefficients a_{lm} in equation (4.34),

$$a_{lm} = \int_{\psi=-\pi/2}^{\pi/2} \int_{\xi=0}^{2\pi} T_{lm}(\hat{\sigma}) Y_{lm}^*(\hat{\sigma}) d\xi d\psi \quad (4.36)$$

is related to what we normally do in the Fourier space.

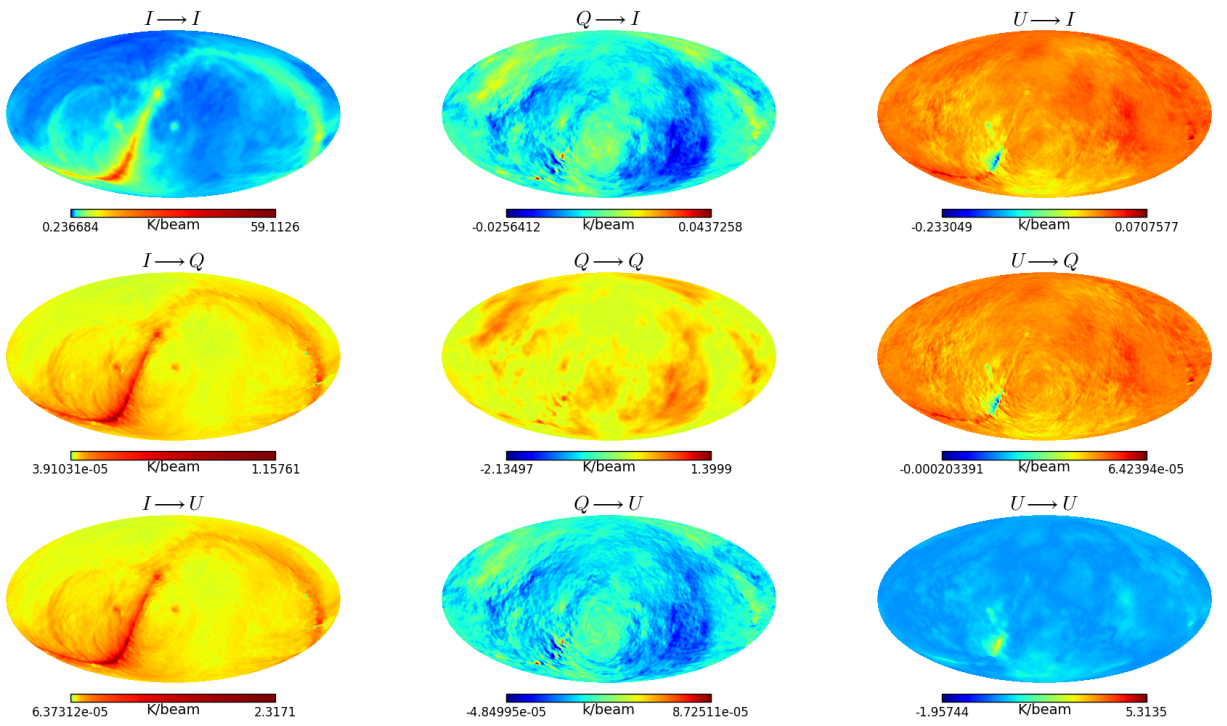


Figure 4.6: Convolved full-sky polarisation maps using the non-distorted OSKAR beams. For example, we used the m_{II} beam in Fig. 4.4a to convolve Stokes I in Fig. 4.5 and produce the convolved map $I \rightarrow I$, then we used m_{QI} beam to convolve Stokes Q to obtain the convolved map $Q \rightarrow I$, also, using the m_{UI} beam to convolve Stokes U we produced the convolved map $U \rightarrow I$. The other convolved maps are produced in the same manner using their respective beams.

Consider any two pixels, then the correlation function of the temperatures is expressed as;

$$C_{cr}(\Theta) = \langle T(\hat{\sigma}_i)T(\hat{\sigma}_j) \rangle, \quad \Theta = \sigma_i \cdot \sigma_j \quad (4.37)$$

where the brackets $\langle \rangle$, denote averaging over $2l + 1$ values of m . Equation (4.37) strictly relies on the separation angle between two sources as discussed in Schramm and Galeotti 1997, p. 78 and therefore, can be rewritten in terms of Legendre polynomials:

$$C_{cr}(\Theta) = \sum_{l=0}^{2l+1} \frac{2l+1}{4\pi} C_l P_l(\cos \Theta) \quad (4.38)$$

From equation (4.38), we can estimate the statistical distribution of the angular power spectrum \hat{C}_l of the entire sky in terms of a_{lm} :

$$\hat{C}_l = \frac{1}{2l+1} \sum_m |\hat{a}_{lm}|^2, \quad -l < m < l \quad (4.39)$$

In this work, we used *anafast* in HEALPix library to compute the auto-power spectrum \hat{C}_l of foregrounds of the sky in section 4.3.1 by executing an approximate, discrete point-set quadrature on a sphere sampled at the HEALPix pixel centres. Spherical harmonic transforms are then computed using recurrence relations for Legendre polynomials on co-latitude ψ and Fast Fourier Transforms on longitude ξ .

4.4 Results and Analysis

The measured maps of $\{I^T, Q^T, U^T\}$ (row 1) and $\{I_D^{GP}, Q_D^{GP}, U_D^{GP}\}$ (row 2) in Fig. 4.8 are generated by convolving both the true and perturbed model beams with the foregrounds and by summing across each of the convolved Stokes terms. (shown in Fig. 4.6). The maps in row 2 correspond to the corruptions due to beam mis-modelling (in this case, due to gain and phase errors as presented in Appendix A.3). Note the similarities between these measured maps, if we compute the differences between them, we can see these simulated maps are not the same and this is even confirmed by the systematic differences in the maps displayed in Fig. 4.7. Moreover, the errors in linear polarisation (QU) terms (in row 3) clearly show the dominance of Stokes I in the measured maps of Stokes Q_D^{GP} and U_D^{GP} . However, this effect can be corrected by subtracting the Stokes I term to regain the original polarisation maps of Q and U . A similar approach is employed to obtain the measured maps in Appendices A.4 and A.5. The latter is obtained when the foregrounds are convolved with the JVLA measured beams whilst the former is produced by using corrupted beams due to orientation errors introduced in the dipoles.

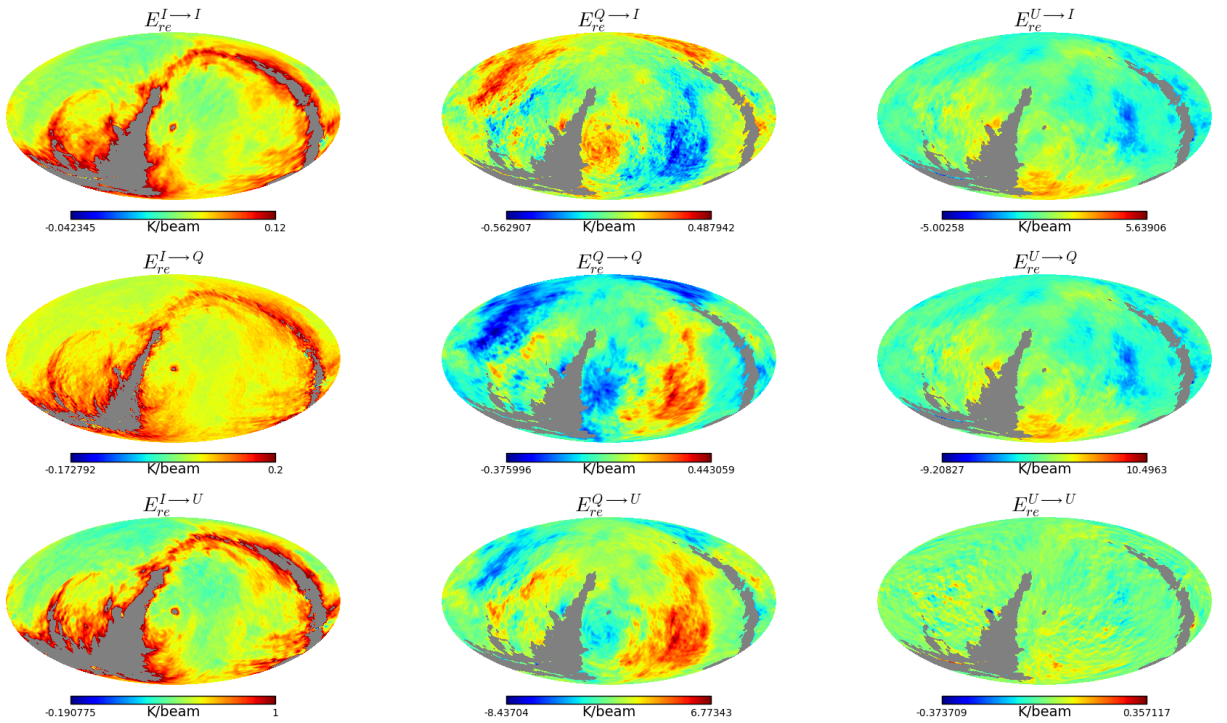


Figure 4.7: Systematic errors of full-sky maps produced by computing the relative error between the absolute of the convolved true sky maps and the corrupted sky maps due to gain and phase error beams.

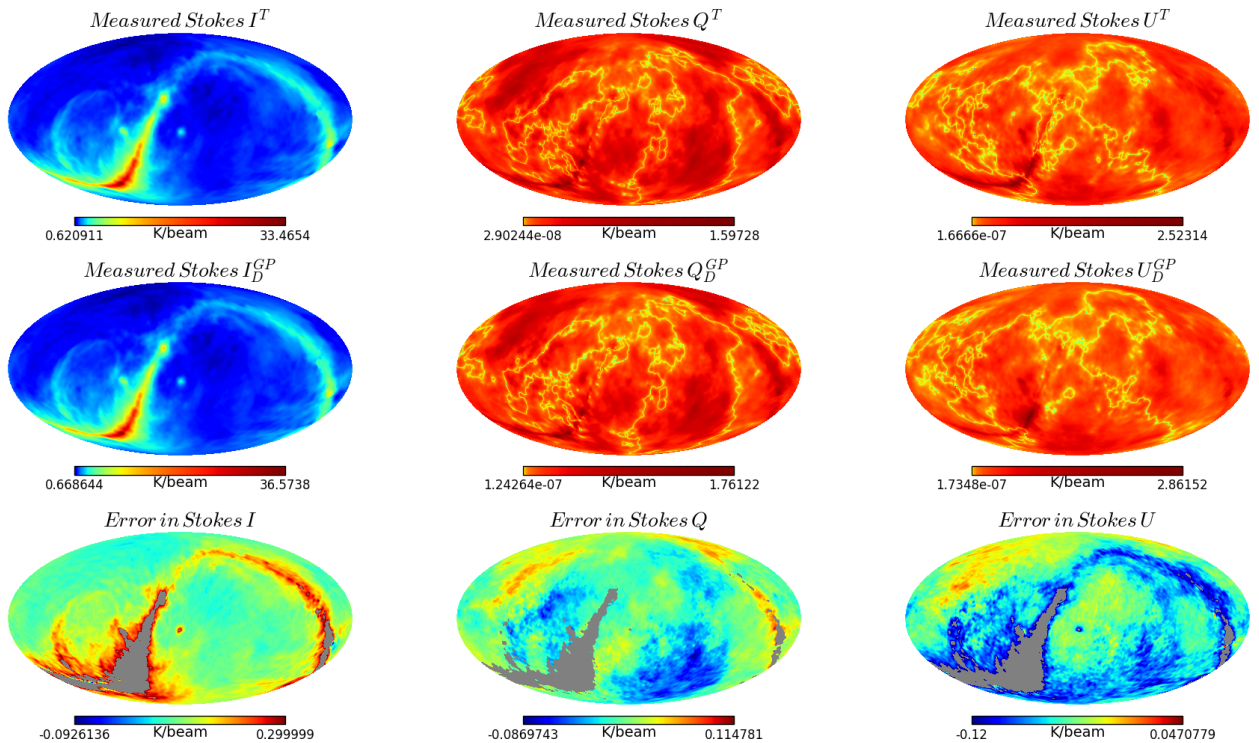


Figure 4.8: The top and middle maps depict the measured foregrounds of Stokes I , Q and U for using the non-distorted and the gain and phase error full polarisation beams respectively. The bottom maps are the corresponding errors in I , Q and U .

The auto-power spectra presented in Fig. 4.9 estimate the density of the measured foregrounds at different multipole moments. Note how the beam power in each plot of both OSKAR and the holographic measured beams is normalised to 1. It is computed by finding the quotient of the power spectrum of the convolved sky map and the original sky map. The OSKAR beam power plots in Stokes I , Q and U , converge at a multipole moment of $l = 60$. This value relates to an angular scale of 3.0° on the sky whilst the power spectra of the JVLA beams converge just at a multipole moment of $l = 100$, giving an angular scale of $1.8^\circ \simeq 2.0^\circ$ on the sky. These angular scales are equivalent to the beam sizes used to convolve the original maps in Fig. 4.5. Note also the effect of these two beams on the convolved power spectra of Stokes I , Q and U . The measured values for the convolved power spectra of Stokes I , Q and U are $10\text{ }K/\text{beam}$, $10^{-1}\text{ }K/\text{beam}$ and $10^{-1}\text{ }K/\text{beam}$ respectively. These values in Fig. 4.9 actually predicted the foreground's temperature of the true sky. Hence, the corresponding errors in I , Q and U due to perturbation of the beams are $\approx 10^{-2}\text{ }K/\text{beam}$, $10^{-4}\text{ }K/\text{beam}$ and $10^{-6}\text{ }K/\text{beam}$ respectively.

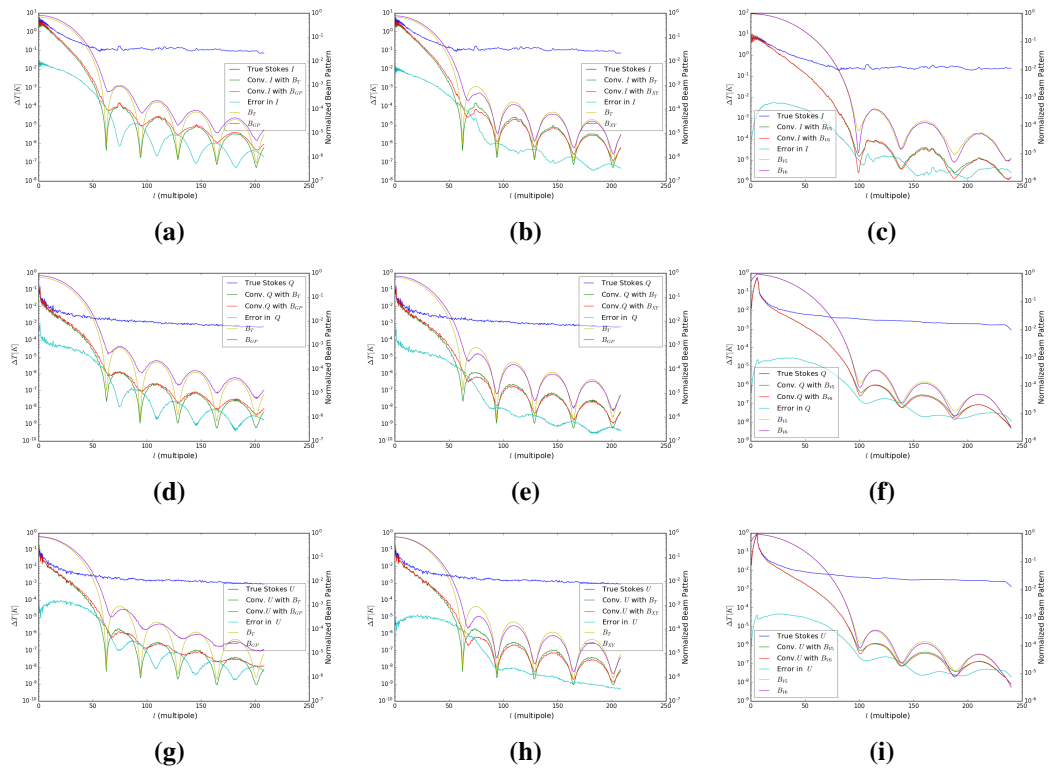


Figure 4.9: Convolved angular power spectra estimation of foreground maps. First row: Shows Stokes I spectra plots for using simulated beams (Fig. 4.9a and 4.9b) and holography measured beams (Fig. 4.9c). Second row: Displays Stokes Q spectra plots for using simulated beams (Fig. 4.9d and 4.9e) and holography measured beams (Fig. 4.9f). Third row: Displays Stokes U spectra plots for using simulated beams (Fig. 4.9g and 4.9h) and holography measured beams (Fig. 4.9i).

In IM experiments, the HI signal is measured in Stokes I , so we are particularly interested in the total intensity and the leakages from polarisation into Stokes I (that is, $|Q + iU| \rightarrow I$). Fig. 4.10 shows how the $|Q + iU| \rightarrow I$ leakage and the error in the Stokes I map affect the HI signal. Here, a spherical power spectrum of the simulated model of 21-cm brightness temperature at $z \approx 0.67$ produced from the CRIME⁶ fast simulation software and described by Alonso, Ferreira, and Santos (2014) is generated and then compared with the spectra plots of the Galactic foregrounds presented in Figs. 4.10a and 4.10b. The HI signal power in Fig. 4.10a is higher than the I -leakage at a multipole moment of $l = 60$ which is about 2 orders of magnitude greater at lower scales. This occurs when we do not correct the beam errors (i.e., gain, phase and orientation of dipole errors) in $Q \rightarrow I$ and $U \rightarrow I$ at all. The fractional leakage of $|Q + iU|$ and I is computed to give $\approx 1.0\%$ for the intrinsic case ($|Q + iU|_T$) where a true model of the beam is known. In this case, the power of the HI signal

⁶<http://intensitymapping.physics.ox.ac.uk/CRIME.html>

is higher than the I -leakage at a multipole moment of $l = 25$. The spectra plots reported in Fig. 4.10b, try to correct the columns that feeds into Stokes I (i.e., $Q \rightarrow I$, $U \rightarrow I$ and $I \rightarrow I$) by assuming the corresponding beams (i.e., m_{QI} , m_{UI} and m_{II}) are not known to the extent to which they have been assumed in this project, then the power spectrum of the HI signal can be observed at a multipole moment of $l = 25$. We conclude that if the knowledge of the beam is of a similar quality than the one assumed in this chapter then we will be able to recover the cosmological HI signal without great problems and without further calibration on scales larger than $l = 60$, however, this work suggests that if polarisation calibration is performed correctly then results can be improved and we can recover scales above $l = 25$. In either case, given the strength of the foregrounds in the galactic centre we will not be able to recover scales larger than $l < 25$.

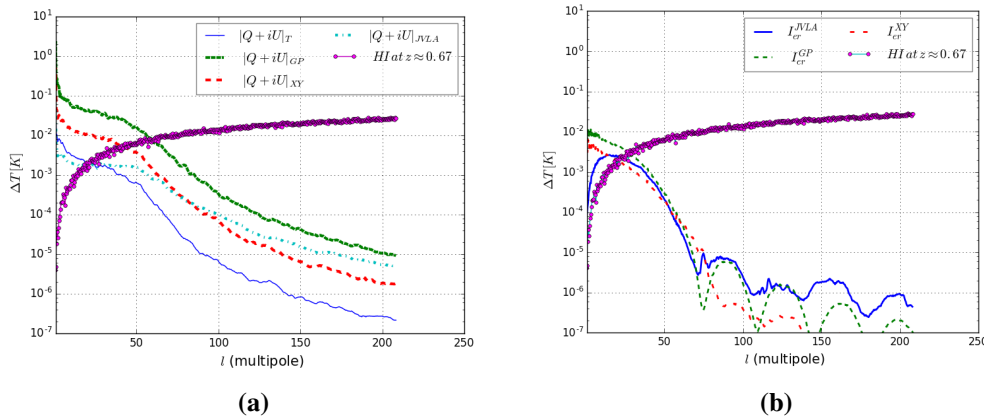


Figure 4.10: Comparing polarisation leakages when there is no beam correction with correcting the beam errors in Stokes I : (a) Quantifies the amount of leakages into Stokes I which is caused by both measured (holography) and modelled (OSKAR) beams. The solid circular spectrum is the simulated 21-cm brightness temperature described by Alonso, Ferreira, and Santos (2014) at a $z \approx 0.67$. The solid thin spectrum ($|Q + iU|_T$), is the leakage in I when the true modelled beams in Fig. 4.4a are used. The dashed spectra plots ($|Q + iU|_{GP}$, $|Q + iU|_{XY}$, $|Q + iU|_{JVL A}$) are the leakages in I when we use modelled beams with gain, phase and dipole displacement and holography measured beams respectively. (b) These spectra plots show the estimate of the 21-cm signal when we correct for the errors in Stokes I beam.

The spectra plots in Fig. 4.11 evaluate the systematic effects of beam errors on Stokes I , Q and U . These residuals are determined as a result of the respective differences between the distorted and non-distorted measured full-sky maps as depicted in Fig. 4.7. We then compute the standard errors of these residual plots to estimate the uncertainties in the angular power spectra when modelled beams are assumed whilst the foreground maps are convolved with

the measured beams. Table A.1 in Appendix A.4 shows the corresponding inaccuracies in the power spectrum estimation. For instance, the standard errors introduced in $Q \rightarrow I$ are $\approx 0.015\%$ (due to gain and phase errors) and 0.014% (due to dipole orientation errors). Also, that of $U \rightarrow I$ are $\approx 0.005\%$ and 0.0045% accordingly. The uncertainties in the spectra plots are as a result of the inaccuracies on the surface of the modelled dish as presented in Fig. 4.3.

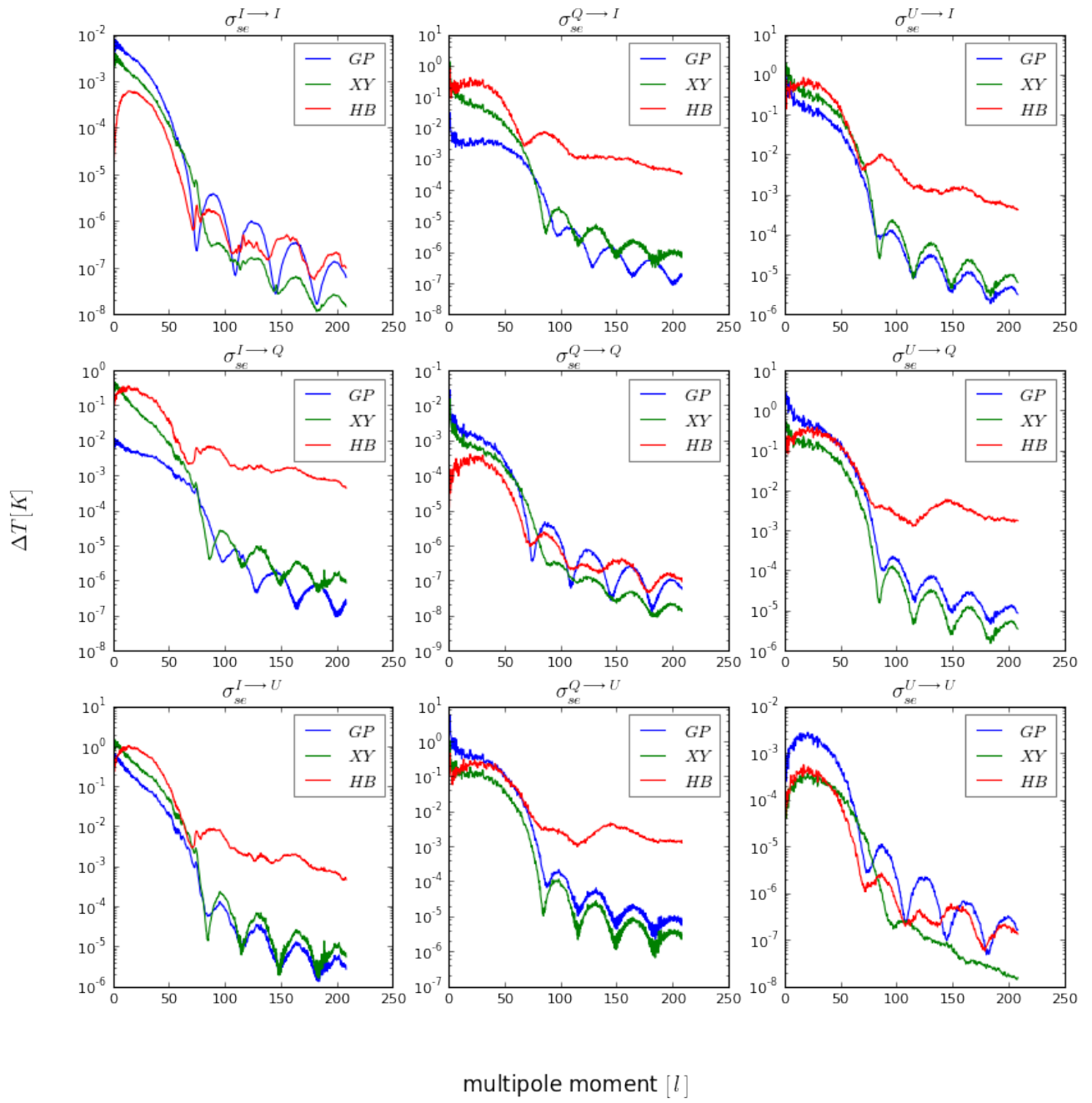


Figure 4.11: These are the spectra plots of the systematic errors in Fig. 4.7. The notations GP and XY in the legends denote the residuals for gain-phase and dipole orientation errors in the OSKAR beams, that of HB depicts the errors in the holography beams. These errors are then used to estimate the imperfections in the simulation by computing the expected value of the standard deviations of the sampling distributions of the residual maps to produce Table A.1.

4.5 Conclusions

The study introduced a relatively cheaper technique to produce realistic primary beams of KAT-7 and perturbed these beams (using gain, phase and dipole orientation errors) for intensity mapping experiments. These fully polarised modelled beams are then used to simulate the full-sky polarisation maps by the method of convolution in order to compute the intensities of the diffused Galactic foregrounds and determine the amount of signals that have seeped from linear polarisation into total intensity. The simulation is repeated using the JVLA holography measured beams and then compared with the modelled beam simulation in order to estimate the error introduced in the power spectrum when modelled beams are used. The following are the key findings of the research:

- The fractional error introduced in the convolved power spectrum estimation for assuming modelled beams to measured beams are 0.08% for Stokes I , 0.03% for Q and 0.07% for U . This is due to the imperfections in the nominal orientation of the dipoles which describe the distribution of the KAT-7 dish-like surface. Our beam modelling showed that there is 0.10% perturbed inaccuracies on the dish surface.
- If we construct a model of a beam and then carry out polarisation rotation and calibration of the phase in order to correct the beam in Stokes I then, the level of leakage to get in Stokes I is $\approx 10^{-2}$ K, given the lack of knowledge of the beam. But, if we don't do any correction at all from the beam then, the kind of leakage we get is $\approx 10^{-1}$ K.
- Furthermore, the power of the HI signal can be estimated at a moment of $l = 25$ when the beam is corrected in Stokes I (i.e., $Q \rightarrow I$, $U \rightarrow I$ and $I \rightarrow I$) and at a moment of $l = 60$ without any beam correction. This makes the latter moment to be > 2 orders of magnitude higher than when we correct the error in the beam.
- Finally, if a true model of the beam is assumed, then the fractional leakage of the intrinsic $|Q + iU|_T \rightarrow I$ is $\approx 1.0\%$, hence, making it possible to measure the power spectrum of the 21-cm signal at a multipole moment of $l = 25$ which conforms to when we correct the beam error in Stokes I .

In summary, the outputs of this research have shown how OSKAR can be used for beam pattern simulations, especially for large aperture arrays like those envisaged for the SKA.

Hence, with the fully polarised modelled beams produced from OSKAR and the convolution technique for foregrounds simulations, we can estimate the amount of foregrounds that had leaked from intensity into polarisation and vice-versa. Our future work is to implement a similar approach with MeerKAT holography measured beams to investigate HI intensity mapping observation.

Chapter 5

EFFECTS OF HI INTENSITY MAPPING WITH MeerKAT

Overview

This Chapter introduces us to ...

5.1 Introduction

Image reconstruction produced from an original data is an inverse problem. Usually, it is difficult to explicitly solve the inverse problem directly. To overcome this difficulty, many orthogonal moment based feature extraction methods such as Zernike Moments (ZM) (Goswami and Prasad 2013; Thuong et al. 2015; Teague 1980), Krawtchouk moments (Clemente et al. 2017; Yap, Paramesran, and Ong 2003), Legendre Moments (LM) (Zhang et al. 2010; Yap and Raveendran 2005), Tchebichef moments (Mukundan, Ong, and Lee 2001; Shu et al. 2010), etc., have been introduced into image analysis and achieved great success. The analysis in (Wu et al. 2017; D’Angelo and Rampone 2016; Zhang and Lu 2004) shows that the

moments based feature representations own some advantages such as compact representation, robustness to noise, invariance properties (i.e. rotation, scale and translation) and low computational as well as storage costs. In this research, ZM method is used to reconstruct the image since, apart from the previous advantages given, the number of coefficients used to reconstruct the image are independent of the number of Zernike polynomials used in the sequence. This condition of independence or orthogonality, means that any number of additional terms can be added without impact on those already computed.

This chapter further explores how the IM techniques discussed in chapter 4 scale to MeerKAT telescopes. Thus, instead of using OSKAR to simulate perturbed fully polarised beams, we fit Zernike polynomials to MeerKAT holography measured beams and then perturbed with the fit. We then simulate these reconstructed beams with the foregrounds to determine the leakage terms.

5.2 Mathematical Basis of Zernike Moments

Consider a wavefront in polar coordinates (ρ, θ) , denoted by $\Phi_w(\rho, \theta)$, to be a linear combination of Zernike polynomials over a circular unit, then this phenomenon can mathematically be expressed as;

$$\Phi_w(\rho, \theta) = \sum_{n,m}^M C_n^m Z_n^m(\rho, \theta) \quad (5.1)$$

The *basis of Zernike moment* $Z_n^m(\rho, \theta)$, in equation 5.1 is defined as (Ferreira et al. 2015);

$$Z_n^m(\rho, \theta) = \begin{cases} N_n^m R_n^{|m|}(\rho) \cos(m\theta), & m \geq 0 \\ -N_n^m R_n^{|m|}(\rho) \sin(m\theta), & m < 0 \end{cases} \quad (5.2)$$

In equation 5.2, the *radial polynomial* $R_n^{|m|}(\rho)$ and the *normalisation factor* N_n^m are denoted as: $R_n^{|m|}(\rho) = \sum_{s=0}^{\frac{n-|m|}{2}} (-1)^s \frac{(n-s)!}{s!(\frac{n+|m|}{2}-s)!(\frac{n-|m|}{2}-s)!} \rho^{n-2s}$, $N_n^m = \sqrt{\frac{2n+1}{1+\delta_{m,0}}}$

where $\delta_{m,0}$ is the Kronecker delta function such that $\delta_{0,0} = 1$ and $\delta_{m,0} = 0$ when $m \neq 0$.

The index $n \geq 0$: $n = 0, 1, 2, \dots$ and for a specific n , the index m takes the values

$$m = -n, -n + 2, -n + 4, \dots, n.$$

The Zernike polynomials $Z_n^m(\rho, \theta)$ are a set of complete orthogonal over a unit circle and this is conveniently represented in equation 5.2 as the products of angular functions and radial polynomials. The orthogonality of this function makes the coefficients not to be dependent on each other (Charman 2005; Wyant and Creath 1992) and hence, these coefficients are normally expressed in double (n, m) or single (j) modes. The n mode characterizes the order of aberration and mode m represents the azimuthal frequency of the sinusoidal. The radius parameter, denoted ρ , is continuous over the range of $(0, 1)$ and this means the azimuthal component is continuous over the range of θ , such that $0 \leq \theta \leq 2\pi$. Fig. 5.1 displays 8 of such radial responses, where it can clearly be observed that the polynomials converge as they approach the edge of the unit disc. This also confirms that, the Zernike polynomials of all orders are confined to the interval $(-1, 1)$ and therefore, can be used as basis functions of image moments as shown in Fig. 5.2.

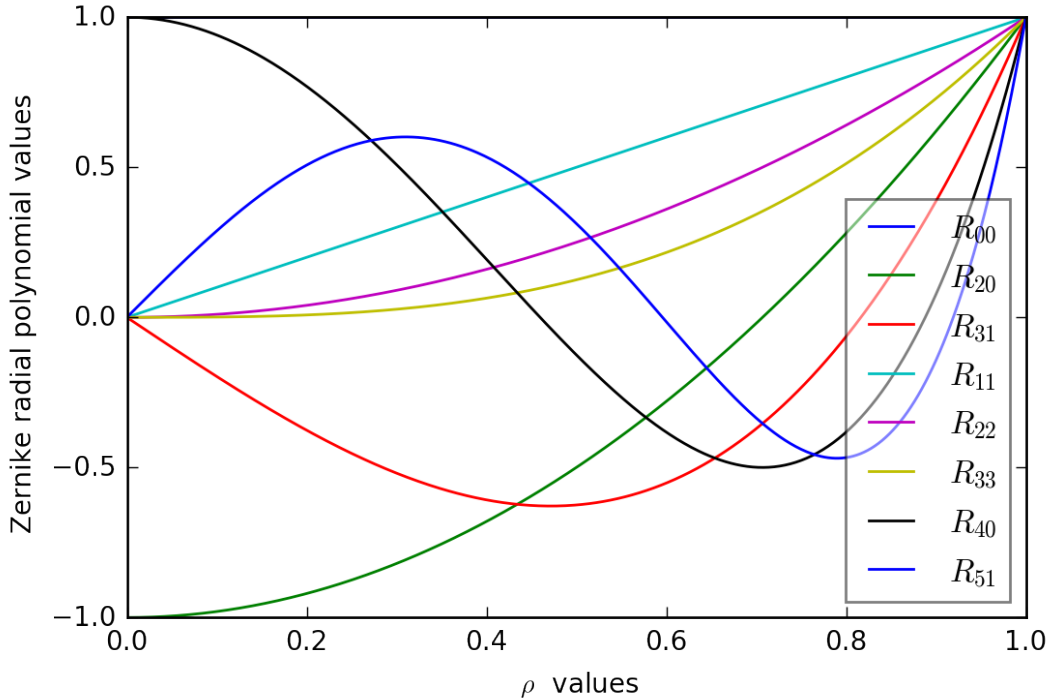


Figure 5.1: Expansion of eight orthogonal radial polynomial $R_n^{[m]}(\rho)$ plots. Here, the value of unity can be obtained at the outer edge, since $R_n^{[m]}(1) = 1$.

The surface plots in Fig. 5.2 depict the Zernike pyramid formed by the first 10 levels. In

the central column, the modes are invariant by rotation (i.e. $m = 0$) and hence, the column can be seen as a symmetry around the axis. On each level (i.e. same n value), the Zernike modes of opposite azimuthal frequency value have the same overall shape, but a different orientation. These pairs are required to enable any mode to be freely oriented around 360° , by selectively adjusting the weight of each mode to obtain the desired orientation.

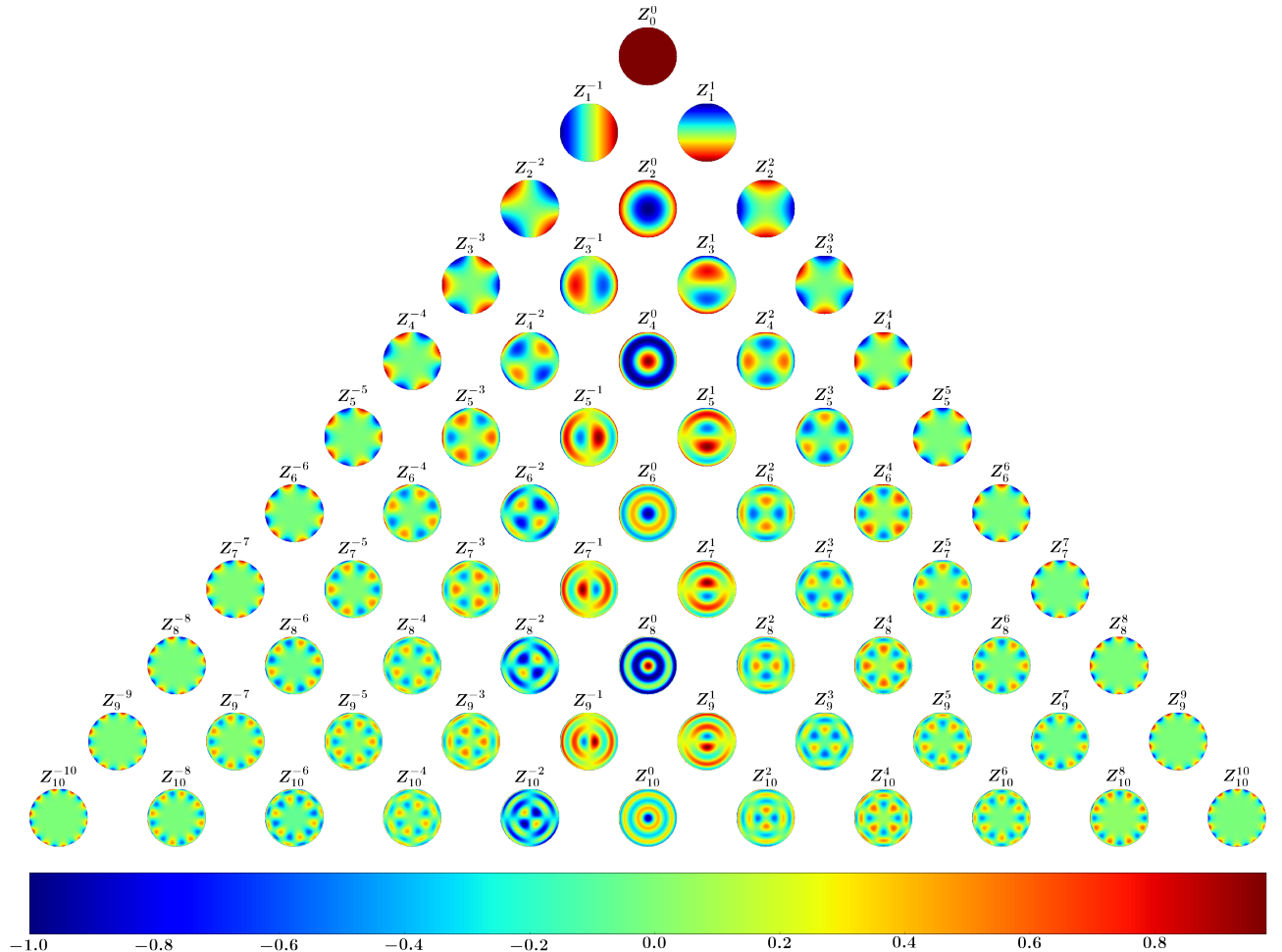


Figure 5.2: Representation of basis patterns of Zernike moments $Z_n^m(\rho, \theta)$ of order 10, plotted on a unit circle.

Occasionally, a single mode scheme is used to describe the Zernike expansion coefficients (Noll 1976; Wyant and Creath 1992). Since the polynomials depend upon two parameters n and m , ordering of a single mode scheme is arbitrary. To obtain the single mode j , it is convenient to lay out the polynomials in a pyramid with row number n and column number m . The single mode, j , starts at the top and the corresponding single indexing scheme, with index variable j , is shown in Table 5.1. In the single mode scheme, we have;

$$Z_j(\rho, \theta) = Z_n^m(\rho, \theta) \quad (5.3)$$

where $j = \frac{n(n+2)+m}{2}$, $n = \left\lceil \frac{-3+\sqrt{(9+8j)}}{2} \right\rceil$ and $m = 2j - n(n + 2)$. The special bracket notation $\lceil . \rceil$ corresponds to the ceil function.

Table 5.1: Relationship between single and double index schemes to third order.

Radial order, n	Angular frequency, m						
	-3	-2	-1	0	1	2	3
0				$j = 0$			
1			$j = 1$		$j = 2$		
2		$j = 3$		$j = 4$		$j = 5$	
3		$j = 6$		$j = 7$		$j = 8$	$j = 9$

In this research, we will deal exclusively with the double indexed Zernike polynomials as portrayed by [14,15, *].

5.2.1 Orthonormality

The orthonormality of a Zernike polynomial for a particular mode (m, n) as described by (*) can be written as:

5.3 Methodology

Since, these are the strongest or activated coefficients, we would expect the activated surfaces to exhibit surface features commonly associated with beams of that type. Our Results are in agreement with expectations of domain experts. For instance, corneas that are diagnosed as XY often have cone shape protruding from the surface. This aberration, referred to as 'coma' in modelled terms z7 or z8 (vertical and horizontal coma). Figure clearly show that feature. That's the activated coefficients which reflect the geometric features of the beams.

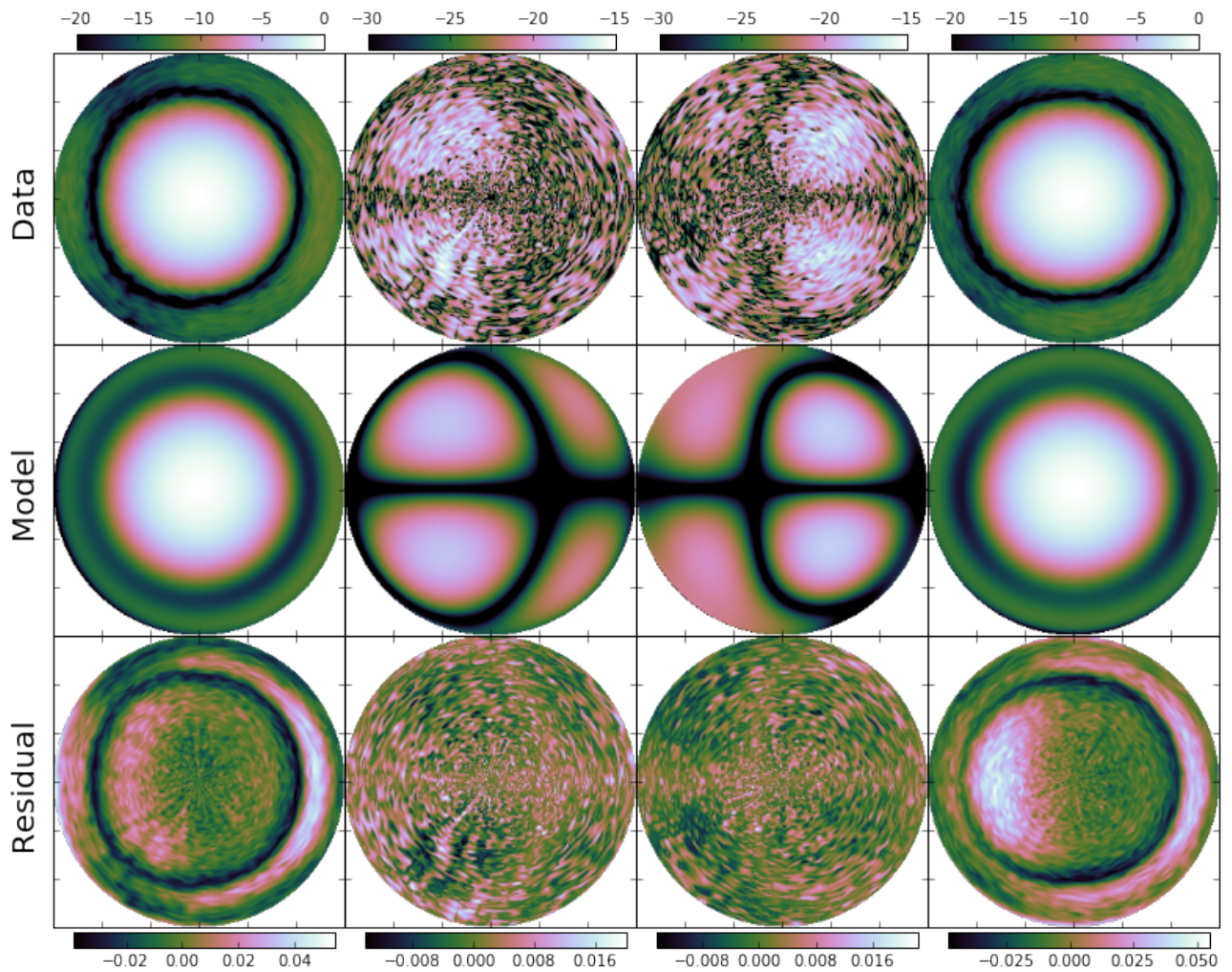


Figure 5.3: Representation of basis patterns of Zernike moments $Z_n^m(\rho, \theta)$ of order 10, plotted on a unit circle.

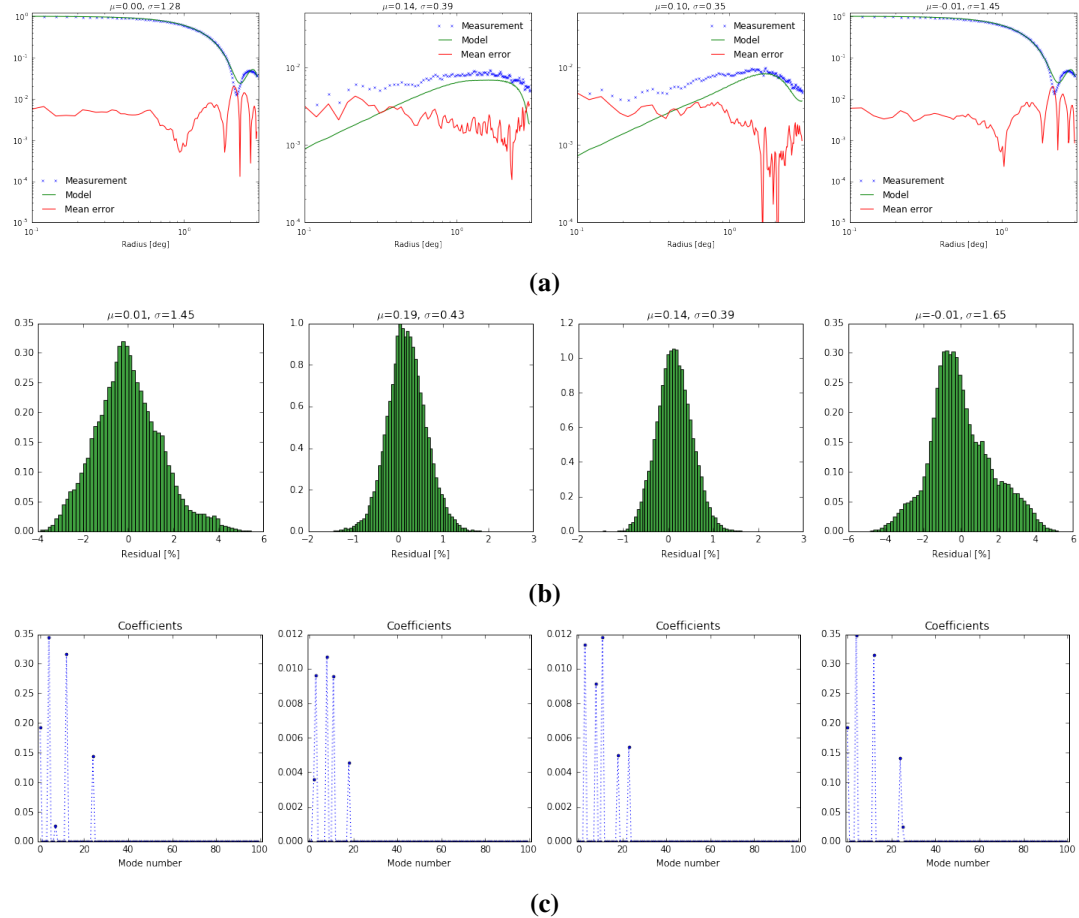


Figure 5.4: Fully polarised distorted primary beams of KAT-7. (a) Due to gain and phase errors. (b) Due to dipole orientation errors.

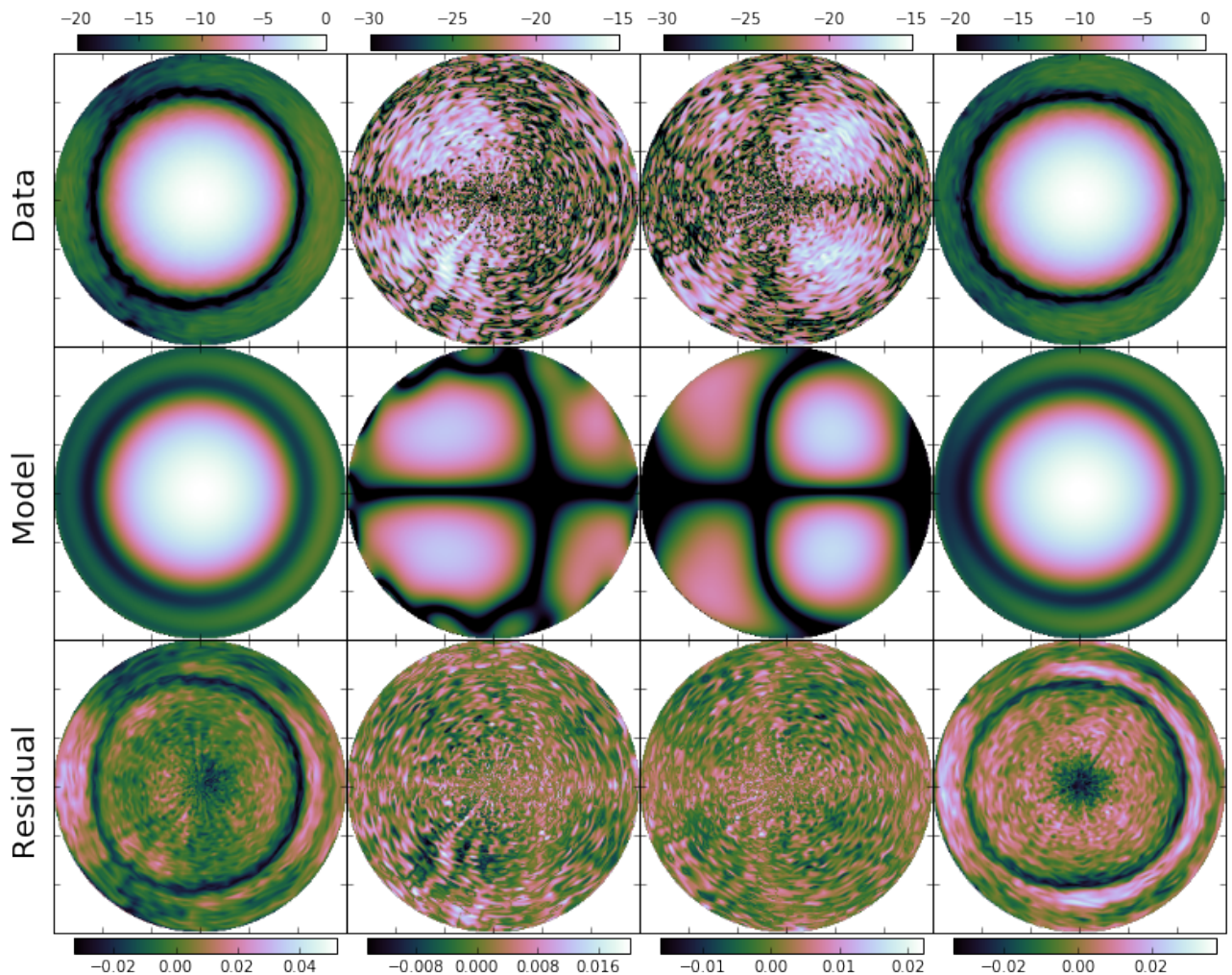


Figure 5.5: Representation of basis patterns of Zernike moments $Z_n^m(\rho, \theta)$ of order 10, plotted on a unit circle.

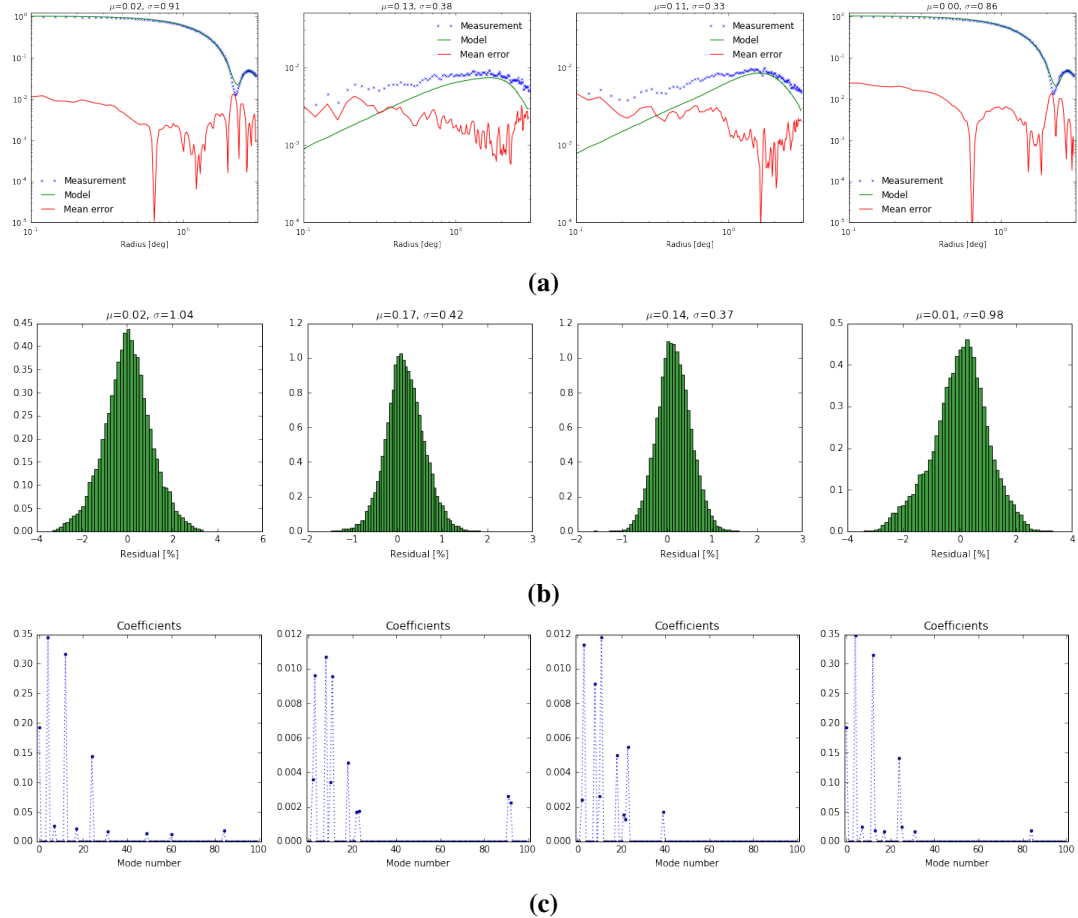


Figure 5.6: Fully polarised distorted primary beams of KAT-7. (a) Due to gain and phase errors. (b) Due to dipole orientation errors.

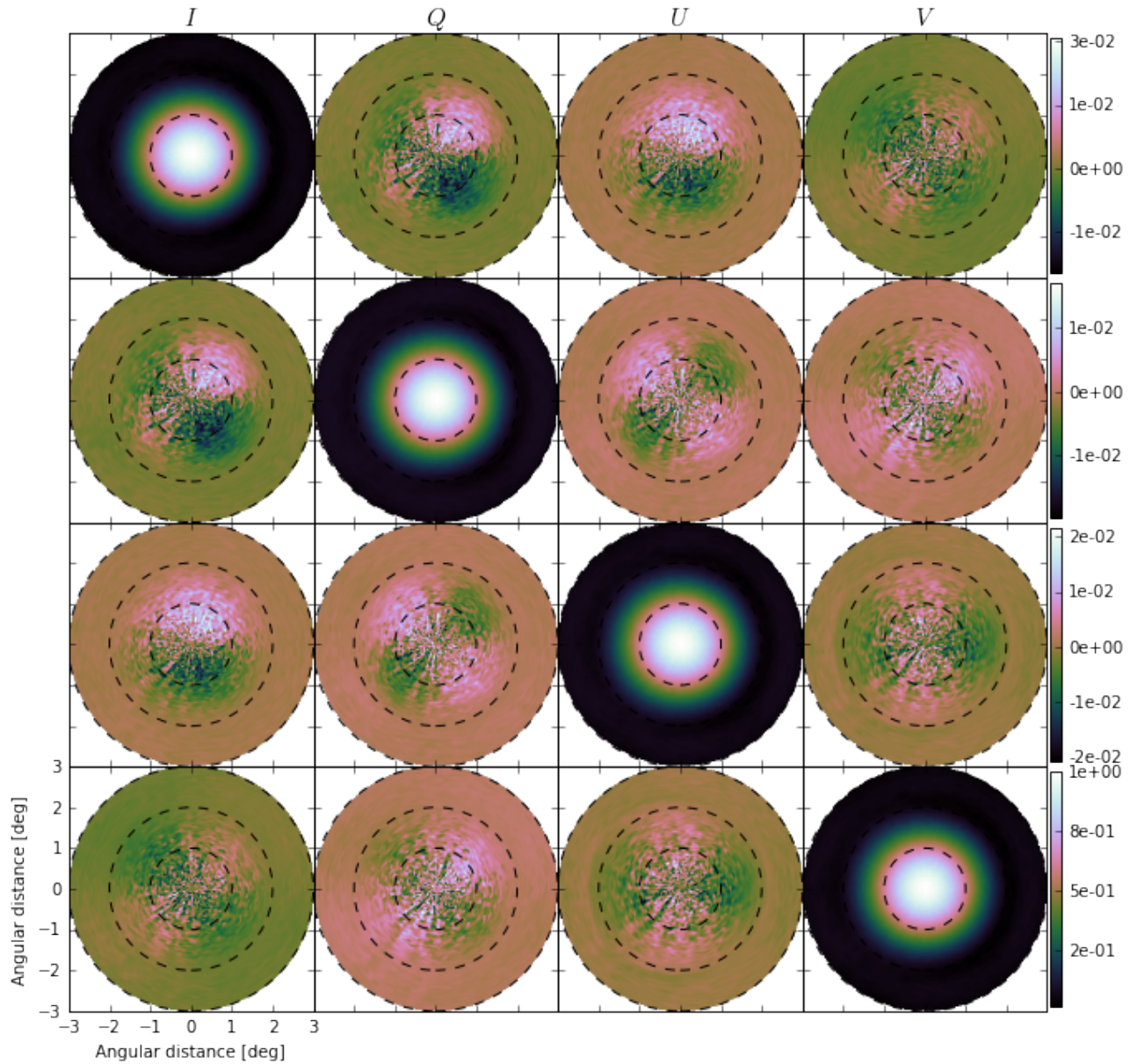


Figure 5.7: Representation of basis patterns of Zernike moments $Z_n^m(\rho, \theta)$ of order 10, plotted on a unit circle.

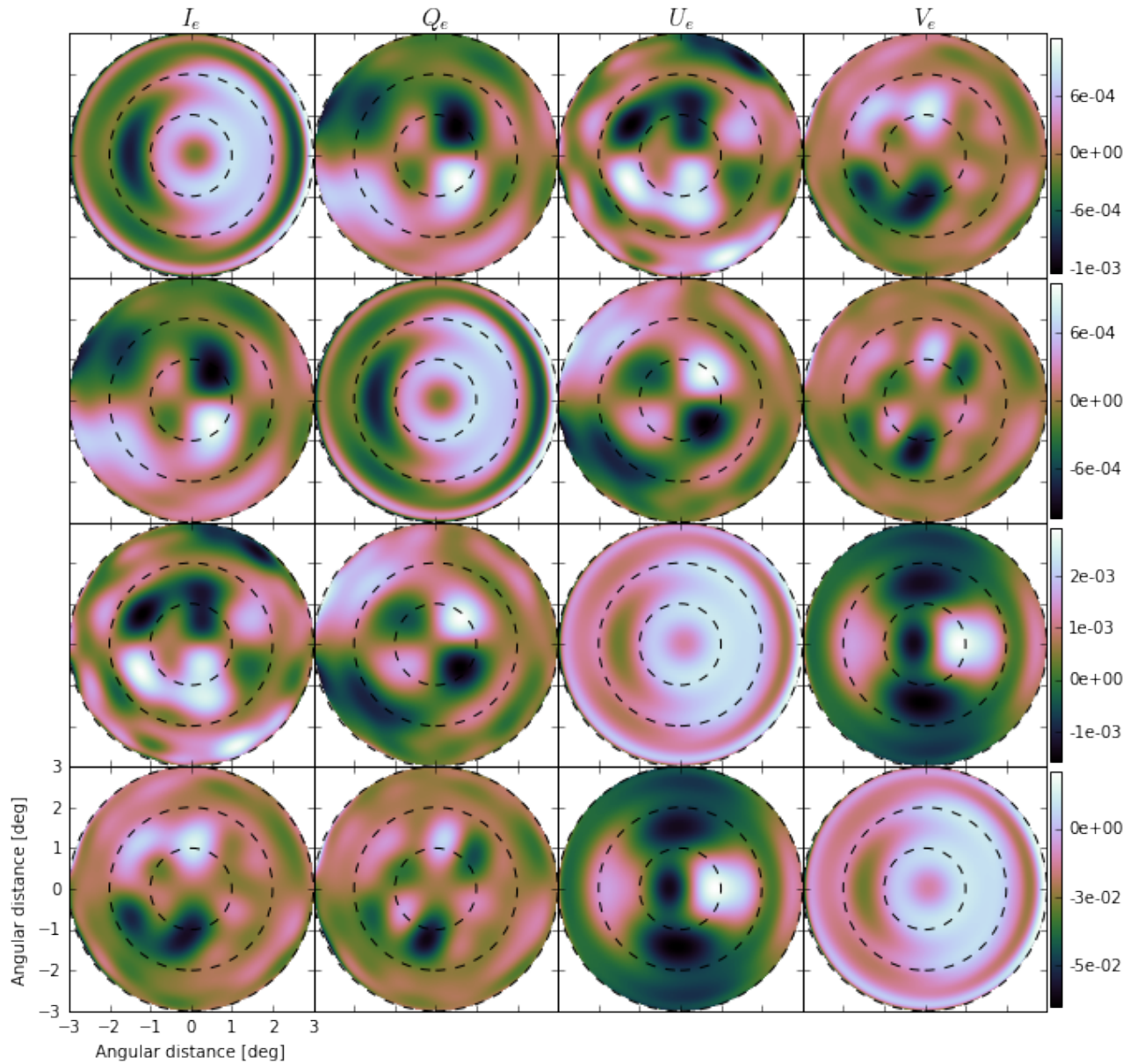


Figure 5.8: Representation of basis patterns of Zernike moments $Z_n^m(\rho, \theta)$ of order 10, plotted on a unit circle.

5.4 Results and Discussion

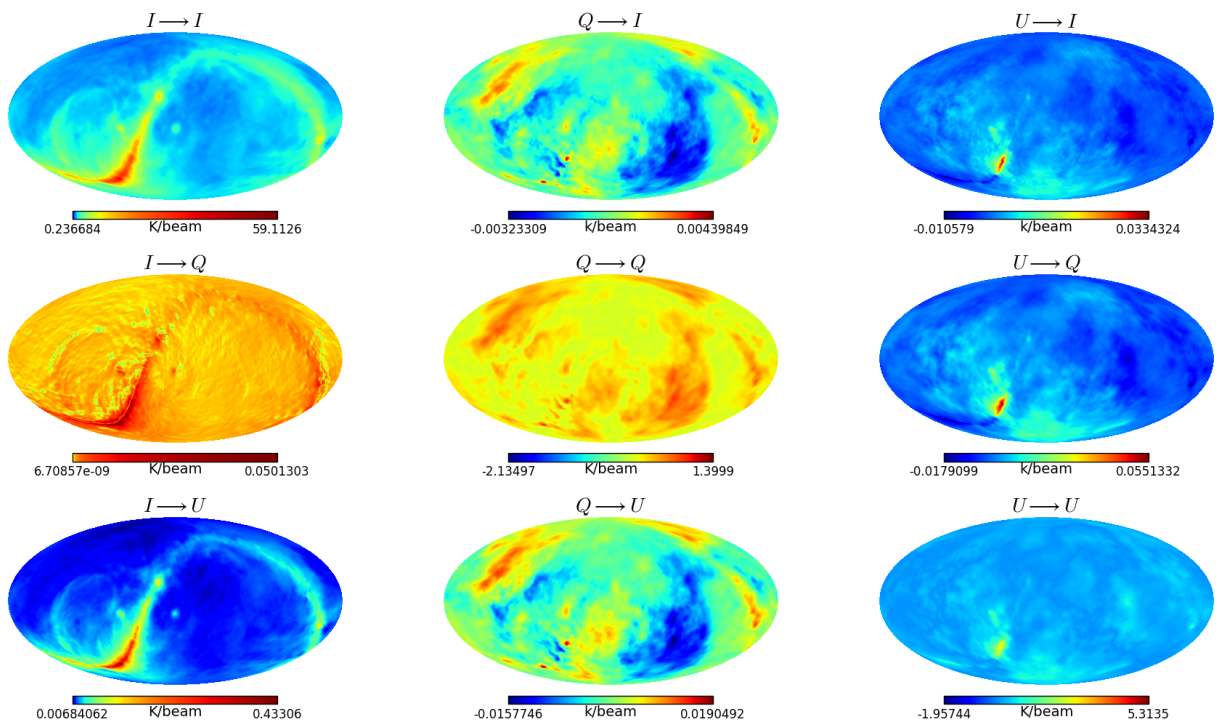


Figure 5.9: Measured Stokes I , Q and U for using non-distorted and distorted dipole orientation error OSKAR beams with corresponding errors terms.

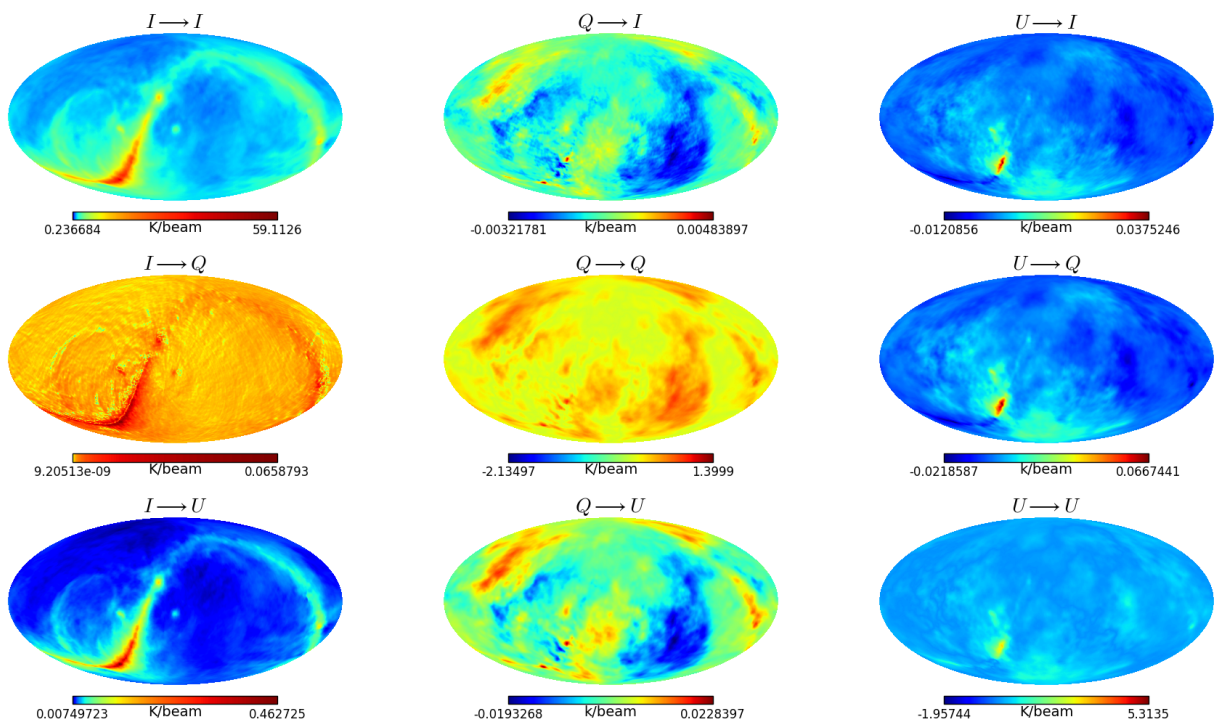


Figure 5.10: Measured Stokes I , Q and U for using non-distorted and distorted dipole orientation error OSKAR beams with corresponding errors terms.

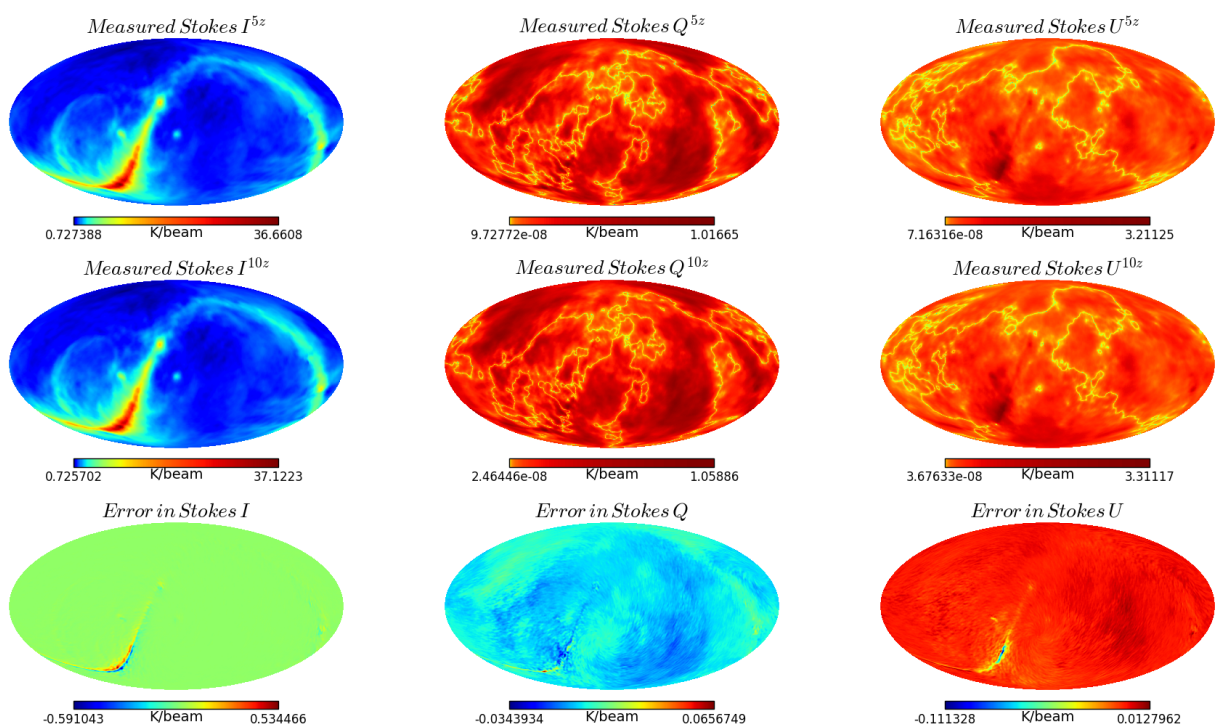


Figure 5.11: Measured Stokes I , Q and U for using non-distorted and distorted dipole orientation error OSKAR beams with corresponding errors terms.

Chapter 6

INVESTIGATING INTENSITY MAPPING EXPERIMENTS WITH SKA1-MID PRIMARY BEAMS

6.1 EM Simulations

EM simulations are computed using Software packages such as General Reflector Antenna Software Package (GRASP) and FEKO. The GRASP software developed by TICRA, produces antenna beampattern by using EM methods such as Physical Theory of Diffraction, Geometrical Theory of Diffraction, Spherical Wave Expansion, Plane Wave Expansion and Methods of Moments for the numerical analysis. For instance, Physical Optics analysis are carried out by computing induced currents on optical surfaces, which are then used to produce the antenna beam pattern. This is good for smooth surfaces and where there are breaks near the edges, Physical Theory of Diffraction is then used to treat those breakages. The FEKO simulator generally models the beampattern of an antenna based on characteristics mode analysis approach (Kim and Nam 2013; Vogel et al. 2015) whereby it applies numerical interpolations of some weighted sets of orthogonal to decompose an incoming signal into current modes.

Digital beamforming techniques such as ray tracing and EM simulations for aperture array

components pose a lot of computational challenges. This research introduces a cheaper technique for producing full polarisation beampattern of KAT-7, using OSKAR simulator and primarily focus on how best to realistically distort these beams. The computational challenge in this proposed technique is relatively less since, the simulator models aperture arrays as a collection of dipoles. The simulation of large aperture array is very unique in IM experiments, since IM experiment relies on large FoV, rather than mosaicking, as they require the noise to be uniform over the field (Vaate et al. 2014). Here, we present a simulation of KAT-7 beam pattern using OSKAR, where the primary beam changes in a known way by simulating pointing errors and then validate these with a holography measured and simulated “ideal” beams of VLA.

Chapter 7

CONCLUSIONS

Bibliography

- Abitbol, M. H., J. C. Hill, and B. R. Johnson (2016). “Foreground-induced biases in CMB polarimeter self-calibration”. In: *MNRAS* 457, pp. 1796–1803. DOI: [10.1093/mnras/stw030](https://doi.org/10.1093/mnras/stw030). arXiv: [1512.06834](https://arxiv.org/abs/1512.06834).
- Abrantes, F. et al. (2009). “Proxy calibration to instrumental data set: Implications for paleoceanographic reconstructions”. In: *Geochemistry, Geophysics, Geosystems* 10, Q09U07, Q09U07. DOI: [10.1029/2009GC002604](https://doi.org/10.1029/2009GC002604). arXiv: [0806.2228](https://arxiv.org/abs/0806.2228).
- Adriani, O. et al. (2011). “Cosmic-Ray Electron Flux Measured by the PAMELA Experiment between 1 and 625 GeV”. In: *Physical Review Letters* 106.20, 201101, p. 201101. DOI: [10.1103/PhysRevLett.106.201101](https://doi.org/10.1103/PhysRevLett.106.201101). arXiv: [1103.2880 \[astro-ph.HE\]](https://arxiv.org/abs/1103.2880).
- Albataineh, Z. and F. M. Salem (2014). “A RobustICA Based Algorithm for Blind Separation of Convulsive Mixtures”. In: *ArXiv e-prints*. arXiv: [1408.0193 \[cs.LG\]](https://arxiv.org/abs/1408.0193).
- Alonso, D., P. G. Ferreira, and M. G. Santos (2014). “Fast simulations for intensity mapping experiments”. In: *MNRAS* 444, pp. 3183–3197. DOI: [10.1093/mnras/stu1666](https://doi.org/10.1093/mnras/stu1666). arXiv: [1405.1751](https://arxiv.org/abs/1405.1751).
- Alonso, D. et al. (2015). “Blind foreground subtraction for intensity mapping experiments”. In: *mnras* 447, pp. 400–416. DOI: [10.1093/mnras/stu2474](https://doi.org/10.1093/mnras/stu2474). arXiv: [1409.8667](https://arxiv.org/abs/1409.8667).
- Anderson, L. B. et al. (2012). “Heterotic line bundle standard models”. In: *Journal of High Energy Physics* 6, 113, p. 113. DOI: [10.1007/JHEP06\(2012\)113](https://doi.org/10.1007/JHEP06(2012)113). arXiv: [1202.1757 \[hep-th\]](https://arxiv.org/abs/1202.1757).
- Armstrong, R. P., K. Zarb Adami, and M. E. Jones (2009). “A Wideband, Four-Element, All-Digital Beamforming System for Dense Aperture Arrays in Radio Astronomy”. In: *ArXiv e-prints*. arXiv: [0910.2865 \[astro-ph.IM\]](https://arxiv.org/abs/0910.2865).
- Asad, K. M. B. et al. (2015). “Polarization leakage in epoch of reionization windows – I. Low Frequency Array observations of the 3C196 field”. In: *Monthly Notices of the Royal Astronomical Society* 451.4, pp. 3709–3727. DOI: [10.1093/mnras/stv1107](https://doi.org/10.1093/mnras/stv1107). eprint: [1412.4003](https://arxiv.org/abs/1412.4003).

- /oup/backfile/content_public/journal/mnras/451/4/10.1093/mnras/stv1107/2/stv1107.pdf. URL: +<http://dx.doi.org/10.1093/mnras/stv1107>.
- Balanis, C. A. (2005). *Antenna Theory Analysis and Design*. Hoboken, New Jersey: John Wiley & Sons, Inc.
- Bandura, K. et al. (2014). “Canadian Hydrogen Intensity Mapping Experiment (CHIME) pathfinder”. In: *Ground-based and Airborne Telescopes V*. Vol. 9145. procspie, p. 914522. DOI: [10.1117/12.2054950](https://doi.org/10.1117/12.2054950). arXiv: [1406.2288 \[astro-ph.IM\]](https://arxiv.org/abs/1406.2288).
- Bass, M. et al. (2009). *Handbook of Optics: Geometrical and Physical Optics, Polarized Light, Components and Instruments*. New York, US: McGraw Hill Professional.
- Battye, R. A. et al. (2012). “BINGO: a single dish approach to 21cm intensity mapping”. In: *ArXiv e-prints*. arXiv: [1209.1041 \[astro-ph.CO\]](https://arxiv.org/abs/1209.1041).
- Beardsley, A. P. et al. (2016). “An Efficient Feedback Calibration Algorithm for Direct Imaging Radio Telescopes”. In: *ArXiv e-prints*. arXiv: [1603.02126 \[astro-ph.IM\]](https://arxiv.org/abs/1603.02126).
- Ben-David, C. and A. Leshem (2008). “Parametric High Resolution Techniques for Radio Astronomical Imaging”. In: *IEEE Journal of Selected Topics in Signal Processing* 2, pp. 670–684. DOI: [10.1109/JSTSP.2008.2005318](https://doi.org/10.1109/JSTSP.2008.2005318). arXiv: [0807.4852](https://arxiv.org/abs/0807.4852).
- Bennett, C. L. et al. (1996). “Four-Year COBE DMR Cosmic Microwave Background Observations: Maps and Basic Results”. In: *apjl* 464, p. L1. DOI: [10.1086/310075](https://doi.org/10.1086/310075). eprint: [astro-ph/9601067](https://arxiv.org/abs/astro-ph/9601067).
- Bennett, C. L. et al. (2003). “First-Year Wilkinson Microwave Anisotropy Probe (WMAP) Observations: Foreground Emission”. In: *apjs* 148, pp. 97–117. DOI: [10.1086/377252](https://doi.org/10.1086/377252). eprint: [astro-ph/0302208](https://arxiv.org/abs/astro-ph/0302208).
- Bennett, C. L. et al. (2013). “Nine-year Wilkinson Microwave Anisotropy Probe (WMAP) Observations: Final Maps and Results”. In: *apjs* 208, 20, p. 20. DOI: [10.1088/0067-0049/208/2/20](https://doi.org/10.1088/0067-0049/208/2/20). arXiv: [1212.5225](https://arxiv.org/abs/1212.5225).
- Bernardi, G. et al. (2016). “A KAT-7 view of a low-mass sample of galaxy clusters”. In: *ArXiv e-prints*. arXiv: [1603.07595](https://arxiv.org/abs/1603.07595).
- Beutler, F. et al. (2011). “The 6dF Galaxy Survey: baryon acoustic oscillations and the local Hubble constant”. In: *MNRAS* 416, pp. 3017–3032. DOI: [10.1111/j.1365-2966.2011.19250.x](https://doi.org/10.1111/j.1365-2966.2011.19250.x). arXiv: [1106.3366](https://arxiv.org/abs/1106.3366).

- Bhatnagar, S. et al. (2008). “Correcting direction-dependent gains in the deconvolution of radio interferometric images”. In: *A&A* 487, pp. 419–429. DOI: [10.1051/0004-6361:20079284](https://doi.org/10.1051/0004-6361:20079284). arXiv: [0805.0834](https://arxiv.org/abs/0805.0834).
- Blake, C. et al. (2011). “The WiggleZ Dark Energy Survey: mapping the distance-redshift relation with baryon acoustic oscillations”. In: *MNRAS* 418, pp. 1707–1724. DOI: [10.1111/j.1365-2966.2011.19592.x](https://doi.org/10.1111/j.1365-2966.2011.19592.x). arXiv: [1108.2635](https://arxiv.org/abs/1108.2635).
- Bobin, J., F. Sureau, and J.-L. Starck (2015). “Polarized CMB recovery with sparse component separation”. In: *ArXiv e-prints*. arXiv: [1508.07131](https://arxiv.org/abs/1508.07131).
- Bolonkin, Alexander (2017). *Femtotechnologies and Innovative Projects*. Lulu. com.
- Born, M. and E. Wolf (1965). *Principles of Optics*. New York: Pergamon Press.
- Born, M. and E. Wolf (1980). *Principles of Optics Electromagnetic Theory of Propagation, Interference and Diffraction of Light*.
- Brisken, W. (2003). *A program for Cassegrain antenna modelling*. A Cassegrain antenna simulator. <http://packages.ubuntu.com/lucid/cassbeam>.
- Burke, Bernard F and Francis Graham-Smith (2009). *An introduction to radio astronomy*. Cambridge University Press.
- Camera, Stefano et al. (2014). “Cosmology on the largest scales with intensity mapping”. In: *Journal of Physics: Conference Series*. Vol. 566. 1. IOP Publishing, p. 012004.
- Camps, A. et al. (1998). “Extension of the Clean Technique to the Microwave Imaging of Continuous Thermal Sources by Means of Aperture Synthesis Radiometers”. In: *Progress In Electromagnetics Research Symposium* 18.
- Chang, T.-C. et al. (2008). “Baryon Acoustic Oscillation Intensity Mapping of Dark Energy”. In: *Phys. Rev. Lett.* 100.091303.
- Chapman, E. et al. (2012). “Foreground removal using FASTICA: a showcase of LOFAR-EoR”. In: *mnras* 423, pp. 2518–2532. DOI: [10.1111/j.1365-2966.2012.21065.x](https://doi.org/10.1111/j.1365-2966.2012.21065.x). arXiv: [1201.2190 \[astro-ph.CO\]](https://arxiv.org/abs/1201.2190).
- Charman, WN (2005). “Wavefront technology: past, present and future”. In: *Contact Lens and Anterior Eye* 28.2, pp. 75–92.
- Chen, X. (2012). “The Tianlai Project: a 21CM Cosmology Experiment”. In: *International Journal of Modern Physics Conference Series*. Vol. 12. International Journal of Modern Physics Conference Series, pp. 256–263. DOI: [10.1142/S2010194512006459](https://doi.org/10.1142/S2010194512006459). arXiv: [1212.6278 \[astro-ph.IM\]](https://arxiv.org/abs/1212.6278).

- Ciardi, B. and P. Madau (2003). “Probing beyond the Epoch of Hydrogen Reionization with 21 Centimeter Radiation”. In: *Astrophysical Journal* 596, pp. 1–8. DOI: [10.1086/377634](https://doi.org/10.1086/377634). eprint: [astro-ph/0303249](https://arxiv.org/abs/astro-ph/0303249).
- Clemente, C. et al. (2017). “Automatic Target Recognition of Military Vehicles With Krawtchouk Moments”. In: *IEEE Transactions on Aerospace Electronic Systems* 53, pp. 493–500. DOI: [10.1109/TAES.2017.2649160](https://doi.org/10.1109/TAES.2017.2649160).
- Cole, S. et al. (2005). “The 2dF Galaxy Redshift Survey: power-spectrum analysis of the final data set and cosmological implications”. In: *MNRAS* 362, pp. 505–534. DOI: [10.1111/j.1365-2966.2005.09318.x](https://doi.org/10.1111/j.1365-2966.2005.09318.x). eprint: [astro-ph/0501174](https://arxiv.org/abs/astro-ph/0501174).
- Colless, M. et al. (2003). “The 2dF Galaxy Redshift Survey: Final Data Release”. In: *ArXiv Astrophysics e-prints*. eprint: [astro-ph/0306581](https://arxiv.org/abs/astro-ph/0306581).
- Compiègne, M. et al. (2011). “The global dust SED: tracing the nature and evolution of dust with DustEM”. In: *aap* 525, A103, A103. DOI: [10.1051/0004-6361/201015292](https://doi.org/10.1051/0004-6361/201015292). arXiv: [1010.2769](https://arxiv.org/abs/1010.2769).
- Contreras, C. et al. (2013). “The WiggleZ Dark Energy Survey: measuring the cosmic growth rate with the two-point galaxy correlation function”. In: *MNRAS* 430, pp. 924–933. DOI: [10.1093/mnras/sts608](https://doi.org/10.1093/mnras/sts608). arXiv: [1302.5178 \[astro-ph.CO\]](https://arxiv.org/abs/1302.5178).
- Coughlan, C. and D. Gabuzda (2012). “MEM and CLEAN Imaging of VLBA Polarisation Observations of Compact Active Galactic Nuclei”. In: *Journal of Physics Conference Series* 355.1, 012020, p. 012020. DOI: [10.1088/1742-6596/355/1/012020](https://doi.org/10.1088/1742-6596/355/1/012020). arXiv: [1107.3481](https://arxiv.org/abs/1107.3481).
- Coughlan, C. P. and D. C. Gabzuda (2013). “MEM imaging of multi-wavelength VLBA polarisation observations of Active Galactic Nuclei”. In: *ArXiv e-prints*. arXiv: [1307.6757 \[astro-ph.GA\]](https://arxiv.org/abs/1307.6757).
- D’Angelo, G. and S. Rampone (2016). “Feature Extraction and Soft Computing Methods for Aerospace Structure Defect Classification”. In: *ArXiv e-prints*. arXiv: [1611.04782 \[cs.CV\]](https://arxiv.org/abs/1611.04782).
- de Oliveira-Costa, A. et al. (2008). “A model of diffuse Galactic radio emission from 10 MHz to 100 GHz”. In: *MNRAS* 388, pp. 247–260. DOI: [10.1111/j.1365-2966.2008.13376.x](https://doi.org/10.1111/j.1365-2966.2008.13376.x). arXiv: [0802.1525](https://arxiv.org/abs/0802.1525).
- Decker, F. J. (1994). *Beam Distributions Beyond RMS*. 6th Workshop on Beam Instrumentation. Standford Linear Accelerator Center, University of Stanford.

- Desai, S. et al. (2016). “Detection and Removal of Artifacts in Astronomical Images”. In: *ArXiv e-prints*. arXiv: [1601.07182 \[astro-ph.IM\]](#).
- Donzelli, S. et al. (2006). “Angular power spectrum of the FASTICA cosmic microwave background component from Background Emission Anisotropy Scanning Telescope data”. In: *mnras* 369, pp. 441–448. DOI: [10.1111/j.1365-2966.2006.10320.x](#). eprint: [astro-ph/0507267](#).
- Doré, O. et al. (2014). “Cosmology with the SPHEREX All-Sky Spectral Survey”. In: *ArXiv e-prints*. arXiv: [1412.4872](#).
- Duev, D. A. et al. (2015). “RadioAstron as a target and as an instrument: Enhancing the Space VLBI mission’s scientific output”. In: *A&A* 573, A99, A99. DOI: [10.1051/0004-6361/201424940](#). arXiv: [1411.4576 \[astro-ph.IM\]](#).
- Duffy, A. R. et al. (2012). “Modelling neutral hydrogen in galaxies using cosmological hydrodynamical simulations”. In: *MNRAS* 420, pp. 2799–2818. DOI: [10.1111/j.1365-2966.2011.19894.x](#). arXiv: [1107.3720 \[astro-ph.CO\]](#).
- Dulwich, F. et al. (2009). “OSKAR: Simulating Digital Beamforming for the SKA Aperture Array”. In: *Wide Field Astronomy & Technology for the Square Kilometre Array*, p. 31.
- Dunkley, J. et al. (2009). “Prospects for polarized foreground removal”. In: *American Institute of Physics Conference Series*. Ed. by S. Dodelson et al. Vol. 1141. American Institute of Physics Conference Series, pp. 222–264. DOI: [10.1063/1.3160888](#). arXiv: [0811.3915](#).
- Emerson, D. (2002). “Why Single Dish”. In: *ASP Conference Series*. 278.
- Fanciullo, L. et al. (2015). “Dust models post-Planck: constraining the far-infrared opacity of dust in the diffuse interstellar medium”. In: *aap* 580, A136, A136. DOI: [10.1051/0004-6361/201525677](#). arXiv: [1506.07011](#).
- Ferreira, C. et al. (2015). “Orthogonal systems of Zernike type in polygons and polygonal facets”. In: *ArXiv e-prints*. arXiv: [1506.07396 \[astro-ph.IM\]](#).
- Finkbeiner, D. P., G. I. Langston, and A. H. Minter (2004). “Microwave Interstellar Medium Emission in the Green Bank Galactic Plane Survey: Evidence for Spinning Dust”. In: *apj* 617, pp. 350–359. DOI: [10.1086/425165](#). eprint: [astro-ph/0408292](#).
- Foster, G. (2015). *Required Instrumentation Information for Interferometrists and Radio Astronomers*. Research Report. RATT, Department of Physics and Electronics, Rhodes University.

- Fu, C. and J. Wu (2005). “Wavelet Interpolation Algorithm for Synthetic Aperture Radiometer”. In: *Progress In Electromagnetics Research Symposium 1.5*, pp. 510–514.
- Garrett, M. A. (2012). “Radio Astronomy Transformed: Aperture Arrays - Past, Present Future”. In: *From Antikythera to the Square Kilometre Array: Lessons from the Ancients*, p. 41. arXiv: [1211.6455 \[astro-ph.IM\]](#).
- Geil, P. M., B. M. Gaensler, and J. S. B. Wyithe (2011). “Polarized foreground removal at low radio frequencies using rotation measure synthesis: uncovering the signature of hydrogen reionization”. In: *mras* 418, pp. 516–535. DOI: [10.1111/j.1365-2966.2011.19509.x](#). arXiv: [1011.2321](#).
- Gold, B. et al. (2009). “Five-Year Wilkinson Microwave Anisotropy Probe Observations: Galactic Foreground Emission”. In: *apjs* 180, pp. 265–282. DOI: [10.1088/0067-0049/180/2/265](#). arXiv: [0803.0715](#).
- Gold, B. et al. (2011). “Seven-year Wilkinson Microwave Anisotropy Probe (WMAP) Observations: Galactic Foreground Emission”. In: *apjs* 192, 15, p. 15. DOI: [10.1088/0067-0049/192/2/15](#). arXiv: [1001.4555](#).
- Goldstein, D. (2003). *Polarized Light: Revised and Expanded*. New York: Marcel Dekker, Inc.
- Gorecki, A. et al. (2014). “A new method to improve photometric redshift reconstruction. Applications to the Large Synoptic Survey Telescope”. In: *aap* 561, A128, A128. DOI: [10.1051/0004-6361/201321102](#). arXiv: [1301.3010](#).
- Górski, K. M. et al. (2005). “HEALPix: A Framework for High-Resolution Discretization and Fast Analysis of Data Distributed on the Sphere”. In: *ApJ* 622, pp. 759–771. DOI: [10.1086/427976](#). eprint: [astro-ph/0409513](#).
- Goswami, G. and J. Prasad (2013). “Maximum entropy deconvolution of primordial power spectrum”. In: 88.2, 023522, p. 023522. DOI: [10.1103/PhysRevD.88.023522](#). arXiv: [1303.4747 \[astro-ph.CO\]](#).
- Gu, J. et al. (2013). “The Application of Continuous Wavelet Transform Based Foreground Subtraction Method in 21 cm Sky Surveys”. In: *ApJ* 773, 38, p. 38. DOI: [10.1088/0004-637X/773/1/38](#). arXiv: [1306.5378](#).
- Hall, J. S. (1949). “Observations of the Polarized Light from Stars”. In: *Science* 109, pp. 166–167. DOI: [10.1126/science.109.2825.166](#).

- Hamaker, J. P., J. D. Bregman, and R. J. Sault (1996). “Understanding radio polarimetry. I. Mathematical foundations.” In: 117, pp. 137–147.
- Haslam, C.G.T. et al. (1982). “A 408 MHz all-sky continuum survey. II. The atlas of contour maps”. In: *A & AS* 47.
- Hiltner, W. A. (1949). “On the Presence of Polarization in the Continuous Radiation of Stars. II.” In: *apj* 109, p. 471. DOI: [10.1086/145151](https://doi.org/10.1086/145151).
- Hinshaw, G. et al. (2007). “Three-Year Wilkinson Microwave Anisotropy Probe (WMAP) Observations: Temperature Analysis”. In: *apjs* 170, pp. 288–334. DOI: [10.1086/513698](https://doi.org/10.1086/513698). eprint: [astro-ph/0603451](https://arxiv.org/abs/astro-ph/0603451).
- Hinshaw, G. et al. (2013). “Nine-year Wilkinson Microwave Anisotropy Probe (WMAP) Observations: Cosmological Parameter Results”. In: *apjs* 208, 19, p. 19. DOI: [10.1088/0067-0049/208/2/19](https://doi.org/10.1088/0067-0049/208/2/19). arXiv: [1212.5226](https://arxiv.org/abs/1212.5226).
- Jelić, V. et al. (2008). “Foreground simulations for the LOFAR-epoch of reionization experiment”. In: *mnras* 389, pp. 1319–1335. DOI: [10.1111/j.1365-2966.2008.13634.x](https://doi.org/10.1111/j.1365-2966.2008.13634.x). arXiv: [0804.1130](https://arxiv.org/abs/0804.1130).
- Jelić, V. et al. (2010). “Realistic simulations of the Galactic polarized foreground: consequences for 21-cm reionization detection experiments”. In: *mnras* 409, pp. 1647–1659. DOI: [10.1111/j.1365-2966.2010.17407.x](https://doi.org/10.1111/j.1365-2966.2010.17407.x). arXiv: [1007.4135](https://arxiv.org/abs/1007.4135).
- Joardar, S. et al. (2010). “Radio Astronomy and Super-synthesis: A Survey”. In: *Progress In Electromagnetics Research B* 22.
- Jones, R. C. (1942). “A new calculus for the treatment of optical systems. IV”. In: *Journal of the Optical Society of America (1917-1983)* 32, p. 486.
- (1948). “New calculus for the treatment of optical systems. VII. Properties of the N-matrices”. In: *Journal of the Optical Society of America (1917-1983)* 38, p. 671.
- Junklewitz, H. et al. (2016). “RESOLVE: A new algorithm for aperture synthesis imaging of extended emission in radio astronomy”. In: *aap* 586, A76, A76. DOI: [10.1051/0004-6361/201323094](https://doi.org/10.1051/0004-6361/201323094). arXiv: [1311.5282 \[astro-ph.IM\]](https://arxiv.org/abs/1311.5282).
- Kim, Y. G and S. Nam (2013). “Determination of the Generalized Scattering Matrix of an Antenna From Characteristic Modes”. In: *IEEE Trans. on Antennas & Propagation* 61.9, pp. 4848–4852.

- Kiyotomo, I. (2014). “CMB foreground: A concise review”. In: *Prog. Theor. Exp. Phys.* 06.B109. URL: <https://inspirehep.net/record/1301472/files/06B109.full.pdf>.
- Knee, Lewis BG and Christopher M Brunt (2001). “A massive cloud of cold atomic hydrogen in the outer Galaxy”. In: *Nature* 412.6844, pp. 308–310.
- Kogut, A. et al. (2007). “Three-Year Wilkinson Microwave Anisotropy Probe (WMAP) Observations: Foreground Polarization”. In: *apj* 665, pp. 355–362. DOI: [10.1086/519754](https://doi.org/10.1086/519754). arXiv: [0704.3991](https://arxiv.org/abs/0704.3991).
- Krachmalnicoff, N. et al. (2016). “Characterization of foreground emission on degree angular scales for CMB B-mode observations . Thermal dust and synchrotron signal from Planck and WMAP data”. In: *A&A* 588, A65, A65. DOI: [10.1051/0004-6361/201527678](https://doi.org/10.1051/0004-6361/201527678). arXiv: [1511.00532](https://arxiv.org/abs/1511.00532).
- Kraus, J. D. (1966). *Radio Astronomy*. New York: McGraw-Hill, Inc.
- Landeck, Carl F et al. (2017). *Apparatus for manufacturing a hydrogen 21 line precision measuring device*. US Patent 9,687,939.
- Lazarian, A. and D. Finkbeiner (2003). “Microwave emission from aligned dust”. In: *nar* 47, pp. 1107–1116. DOI: [10.1016/j.newar.2003.09.037](https://doi.org/10.1016/j.newar.2003.09.037). eprint: [astro-ph/0307012](https://arxiv.org/abs/astro-ph/0307012).
- Lazarian, A. and S. Prunet (2002). “Polarized microwave emission from dust”. In: *Astrophysical Polarized Backgrounds*. Ed. by S. Cecchini et al. Vol. 609. American Institute of Physics Conference Series, pp. 32–43. DOI: [10.1063/1.1471820](https://doi.org/10.1063/1.1471820). eprint: [astro-ph/0111214](https://arxiv.org/abs/astro-ph/0111214).
- Leshem, A. and A.-J. van der Veen (2000). “Radio astronomical imaging in the presence of strong radio interference”. In: *ArXiv Astrophysics e-prints*. eprint: [astro-ph/0008239](https://arxiv.org/abs/astro-ph/0008239).
- Levanda, R. and A. Lessem (2010a). “Adaptive selective sidelobe canceller beamformer with applications in radio astronomy”. In: *ArXiv e-prints*. arXiv: [1008.5066 \[astro-ph.IM\]](https://arxiv.org/abs/1008.5066). – (2010b). “Synthetic aperture radio telescopes”. In: *IEEE Signal Processing Magazine* 27, pp. 14–29. DOI: [10.1109/MSP.2009.934719](https://doi.org/10.1109/MSP.2009.934719). arXiv: [1009.0460 \[astro-ph.IM\]](https://arxiv.org/abs/1009.0460).
- Loeb, A. and J. S. B. Wyithe (2008). “Possibility of Precise Measurement of the Cosmological Power Spectrum with a Dedicated Survey of 21cm Emission after Reionization”. In: *Physical Review Letters* 100.16, 161301, p. 161301. DOI: [10.1103/PhysRevLett.100.161301](https://doi.org/10.1103/PhysRevLett.100.161301). arXiv: [0801.1677](https://arxiv.org/abs/0801.1677).

- López, Ericson et al. (2017). “The HI Distribution Observed toward a Halo Region of the Milky Way”. In: *Galaxies* 5.3, p. 45.
- Machin, K. E., M. Ryle, and D. D. Vonberg (1952). “The Design of an Equipment for Measuring Small Radio Frequency Noise Powers”. In: *roc. IEEE* 99.
- Madau, P., A. Meiksin, and M. J. Rees (1997). “21 Centimeter Tomography of the Inter-galactic Medium at High Redshift”. In: *Astrophysical Journal* 475, pp. 429–444. eprint: [astro-ph/9608010](#).
- Maino, D. et al. (2007). “Cosmic microwave background signal in Wilkinson Microwave Anisotropy Probe three-year data with FASTICA”. In: *mnras* 374, pp. 1207–1215. DOI: [10.1111/j.1365-2966.2006.11255.x](https://doi.org/10.1111/j.1365-2966.2006.11255.x). eprint: [astro-ph/0609228](#).
- Masui, K. W. et al. (2013). “Measurement of 21 cm Brightness Fluctuations at $z \sim 0.8$ in Cross-correlation”. In: *ApJL* 763, L20, p. L20. DOI: [10.1088/2041-8205/763/1/L20](https://doi.org/10.1088/2041-8205/763/1/L20). arXiv: [1208.0331 \[astro-ph.CO\]](#).
- Miller, F. D. (1998). *Basics of Radio Astronomy for the Goldstone-Apple Valley Radio Telescope*. Pasadena, California: California Institute of Technology.
- Mitchell, D. A. and J. G. Robertson (2005). “Reference antenna techniques for canceling radio frequency interference due to moving sources”. In: *Radio Science* 40, RS5S11, RS5S11. DOI: [10.1029/2004RS003152](https://doi.org/10.1029/2004RS003152). arXiv: [1003.5997 \[astro-ph.IM\]](#).
- Miville-Deschénes, M.-A. et al. (2008). “Separation of anomalous and synchrotron emissions using WMAP polarization data”. In: *aap* 490, pp. 1093–1102. DOI: [10.1051/0004-6361:200809484](https://doi.org/10.1051/0004-6361:200809484). arXiv: [0802.3345](#).
- Mort, B. et al. (2017). “Analysing the impact of far-out sidelobes on the imaging performance of the SKA-LOW telescope”. In: *MNRAS* 465, pp. 3680–3692. DOI: [10.1093/mnras/stw2814](https://doi.org/10.1093/mnras/stw2814). arXiv: [1602.01805 \[astro-ph.IM\]](#).
- Mort, Benjamin J et al. (2010). “OSKAR: Simulating digital beamforming for the SKA aperture array”. In: *Phased Array Systems and Technology (ARRAY), 2010 IEEE International Symposium on*. IEEE, pp. 690–694.
- Mukundan, R., S. H. Ong, and P. A. Lee (2001). “Image analysis by Tchebichef moments”. In: *IEEE Transactions on Image Processing* 10, pp. 1357–1364. DOI: [10.1109/83.941859](https://doi.org/10.1109/83.941859).

- Nan, R. et al. (2011). “The Five-Hundred Aperture Spherical Radio Telescope (fast) Project”. In: *International Journal of Modern Physics D* 20, pp. 989–1024. DOI: [10.1142/S0218271811019335](https://doi.org/10.1142/S0218271811019335). arXiv: [1105.3794 \[astro-ph.IM\]](https://arxiv.org/abs/1105.3794).
- Navarro, M. V. (2014). “Diffuse Radio Foregrounds: All-Sky Polarisation and Anomalous Microwave Emission”. MA thesis. University of Manchester.
- Newburgh, L. B. et al. (2014). “Calibrating CHIME: a new radio interferometer to probe dark energy”. In: *Ground-based and Airborne Telescopes V*. Vol. 9145. procspie, p. 91454V. DOI: [10.1117/12.2056962](https://doi.org/10.1117/12.2056962). arXiv: [1406.2267 \[astro-ph.IM\]](https://arxiv.org/abs/1406.2267).
- Noll, R. J. (1976). “Zernike polynomials and atmospheric turbulence”. In: *Journal of the Optical Society of America (1917-1983)* 66, pp. 207–211.
- Pagani, L. et al. (2015). “Can we trace very cold dust from its emission alone?” In: *aap* 574, L5, p. L5. DOI: [10.1051/0004-6361/201425095](https://doi.org/10.1051/0004-6361/201425095). arXiv: [1501.00861](https://arxiv.org/abs/1501.00861).
- Percival, W. J. et al. (2010). “Baryon acoustic oscillations in the Sloan Digital Sky Survey Data Release 7 galaxy sample”. In: *MNRAS* 401, pp. 2148–2168. DOI: [10.1111/j.1365-2966.2009.15812.x](https://doi.org/10.1111/j.1365-2966.2009.15812.x). arXiv: [0907.1660 \[astro-ph.CO\]](https://arxiv.org/abs/0907.1660).
- Perley R., Sowinski K. and et al. (2015). *Optimizing VLA Antenna Performance*. EVLA Memo XXX.
- Peterson, J. B. et al. (2009). “21-cm Intensity Mapping”. In: *astro2010: The Astronomy and Astrophysics Decadal Survey*. Vol. 2010. ArXiv Astrophysics e-prints, p. 234. arXiv: [0902.3091 \[astro-ph.IM\]](https://arxiv.org/abs/0902.3091).
- Pforr, J., C. Maraston, and C. Tonini (2012). “Recovering galaxy stellar population properties from broad-band spectral energy distribution fitting”. In: *mnras* 422, pp. 3285–3326. DOI: [10.1111/j.1365-2966.2012.20848.x](https://doi.org/10.1111/j.1365-2966.2012.20848.x). arXiv: [1203.3548](https://arxiv.org/abs/1203.3548).
- Planck Collaboration et al. (2014). “Planck 2013 results. XVI. Cosmological parameters”. In: *aap* 571, A16, A16. DOI: [10.1051/0004-6361/201321591](https://doi.org/10.1051/0004-6361/201321591). arXiv: [1303.5076](https://arxiv.org/abs/1303.5076).
- Pogany, T. K. and S. Nadarajah (2009). *On the characteristic function of the generalized normal distribution*. Research Report 18. Probability and Statistics Group School of Mathematics, The University of Manchester.
- Rau, U. et al. (2009). “Advances in Calibration and Imaging Techniques in Radio Interferometry”. In: *Proc. IEEE* 97.
- Roy, J., B. Bhattacharyya, and Y. Gupta (2012). “A multi-pixel beamformer using an interferometric array and its application to the localization of newly discovered pulsars”. In:

- MNRAS* 427, pp. L90–L94. DOI: [10.1111/j.1745-3933.2012.01351.x](https://doi.org/10.1111/j.1745-3933.2012.01351.x). arXiv: [1209.3858 \[astro-ph.IM\]](https://arxiv.org/abs/1209.3858).
- Sadeh, I., L. L. Feng, and O. Lahav (2015). “Gravitational Redshift of Galaxies in Clusters from the Sloan Digital Sky Survey and the Baryon Oscillation Spectroscopic Survey”. In: *Physical Review Letters* 114.7, 071103, p. 071103. DOI: [10.1103/PhysRevLett.114.071103](https://doi.org/10.1103/PhysRevLett.114.071103). arXiv: [1410.5262](https://arxiv.org/abs/1410.5262).
- Saha, R., P. Jain, and T. Souradeep (2006). “A Blind Estimation of the Angular Power Spectrum of CMB Anisotropy from WMAP”. In: *ApJL* 645, pp. L89–L92. DOI: [10.1086/506321](https://doi.org/10.1086/506321). eprint: [astro-ph/0508383](https://arxiv.org/abs/astro-ph/0508383).
- Santiago, B. X. et al. (1995). “The Optical Redshift Survey: Sample Selection and the Galaxy Distribution”. In: *ApJ* 446, p. 457. DOI: [10.1086/175805](https://doi.org/10.1086/175805). eprint: [astro-ph/9406049](https://arxiv.org/abs/astro-ph/9406049).
- (1996). “The Optical Redshift Survey. II. Derivation of the Luminosity and Diameter Functions and of the Density Field”. In: *ApJ* 461, p. 38. DOI: [10.1086/177036](https://doi.org/10.1086/177036). eprint: [astro-ph/9511005](https://arxiv.org/abs/astro-ph/9511005).
- Santos, M. et al. (2015a). “Cosmology from a SKA HI intensity mapping survey”. In: *Advancing Astrophysics with the Square Kilometre Array (AASKA14)*, 19, p. 19. arXiv: [1501.03989](https://arxiv.org/abs/1501.03989).
- Santos, M. G. et al. (2015b). “Cosmology with a SKA HI intensity mapping survey”. In: *ArXiv e-prints*. arXiv: [1501.03989](https://arxiv.org/abs/1501.03989).
- Schneider, P. (2006). *Extragalactic Astronomy and Cosmology*. New York, US: Springer.
- Schramm, D. N. and P. Galeotti (1997). *Generation of Cosmological Large-Scale Structure*. Netherlands: Kluwer Academic.
- Shaw, J. R. et al. (2015). “Coaxing cosmic 21 cm fluctuations from the polarized sky using m-mode analysis”. In: *prd* 91.8, 083514, p. 083514. DOI: [10.1103/PhysRevD.91.083514](https://doi.org/10.1103/PhysRevD.91.083514). arXiv: [1401.2095](https://arxiv.org/abs/1401.2095).
- Shu, H. et al. (2010). “Fast Computation of Tchebichef Moments for Binary and Grayscale Images”. In: *IEEE Transactions on Image Processing* 19, pp. 3171–3180. DOI: [10.1109/TIP.2010.2052276](https://doi.org/10.1109/TIP.2010.2052276).
- Shurcliff, W. (1962). *Polarized Light*. Cambridge, MA: Harvard University Press.
- Sinclair, D. et al. (2014). “Effect of gain and phase errors on SKA1-low imaging quality from 50-600 MHz”. In: *ArXiv e-prints*. arXiv: [1408.3998 \[astro-ph.IM\]](https://arxiv.org/abs/1408.3998).

- Smirnov, O. M. (2011). “Revisiting the radio interferometer measurement equation. I. A full-sky Jones formalism”. In: *A&A* 527, A106, A106. doi: [10.1051/0004-6361/201016082](https://doi.org/10.1051/0004-6361/201016082). arXiv: [1101.1764 \[astro-ph.IM\]](https://arxiv.org/abs/1101.1764).
- Smoot, G. F. (1998). “Galactic Free-free and H-alpha Emission”. In: *ArXiv Astrophysics e-prints*. eprint: [astro-ph/9801121](https://arxiv.org/abs/astro-ph/9801121).
- Smoot, G. F. and I. Debono (2017). “21 cm intensity mapping with the Five hundred metre Aperture Spherical Telescope”. In: *A&A* 597, A136, A136. doi: [10.1051/0004-6361/201526794](https://doi.org/10.1051/0004-6361/201526794). arXiv: [1407.3583](https://arxiv.org/abs/1407.3583).
- Souradeep, T., R. Saha, and P. Jain (2006). “Angular power spectrum of CMB anisotropy from WMAP”. In: 50, pp. 854–860. doi: [10.1016/j.newar.2006.09.009](https://doi.org/10.1016/j.newar.2006.09.009). eprint: [astro-ph/0608199](https://arxiv.org/abs/astro-ph/0608199).
- Teague, M. R. (1980). “Image analysis via the general theory of moments”. In: *Journal of the Optical Society of America (1917-1983)* 70, pp. 920–930.
- Tegmark, M. and G. Efstathiou (1996). “A method for subtracting foregrounds from multi-frequency CMB sky maps”. In: *mnras* 281, pp. 1297–1314. doi: [10.1093/mnras/281.4.1297](https://doi.org/10.1093/mnras/281.4.1297). eprint: [astro-ph/9507009](https://arxiv.org/abs/astro-ph/9507009).
- The Polarbear Collaboration: P. A. R. Ade et al. (2014). “A Measurement of the Cosmic Microwave Background B-mode Polarization Power Spectrum at Sub-degree Scales with POLARBEAR”. In: *apj* 794, 171, p. 171. doi: [10.1088/0004-637X/794/2/171](https://doi.org/10.1088/0004-637X/794/2/171). arXiv: [1403.2369](https://arxiv.org/abs/1403.2369).
- Thompson, A. R. and R. N Bracewell (1974). “Interpolation and Fourier Transformation of Fringe Visibilities”. In: *Astro. J.* 79.
- Thompson, A. R., J.M Moran, and G.W Swenson (2001). *Interferometry and Synthesis in Radio Astronomy, 2nd edition*. John Wiley & Sons Inc.
- Thuong, Le-Tien et al. (2015). “Zernike Moment-Based Approach for Detecting Duplicated Image Regions by a Modified Method to Reduce Geometrical and Numerical Errors”. In: *Computational Science and Its Applications - ICCSA 2015 - 15th International Conference, Banff, AB, Canada, June 22-25, 2015, Proceedings, Part IV*, pp. 458–475. doi: [10.1007/978-3-319-21410-8_36](https://doi.org/10.1007/978-3-319-21410-8_36). URL: https://doi.org/10.1007/978-3-319-21410-8_36.

- Tucci, M. et al. (2002). “Polarization Angular Spectra of Galactic Synchrotron Emission on Arcminute Scales”. In: *apj* 579, pp. 607–615. DOI: [10.1086/342793](https://doi.org/10.1086/342793). eprint: [astro-ph/0207237](https://arxiv.org/abs/astro-ph/0207237).
- Vaate, J. G. B. de et al. (2014). “SKA Mid Frequency Aperture Arrays: Technology for the Ultimate Survey Machine”. In: *General Assembly and Scientific Symposium*, pp. 1–4.
- van Haarlem, M. P. et al. (2013). “LOFAR: The LOw-Frequency ARray”. In: *A&A* 556, A2, A2. DOI: [10.1051/0004-6361/201220873](https://doi.org/10.1051/0004-6361/201220873). arXiv: [1305.3550 \[astro-ph.IM\]](https://arxiv.org/abs/1305.3550).
- Vogel, M. et al. (2015). “Characteristic Mode Analysis: Putting Physics back into Simulation”. In: *IEEE Trans. on Antennas & Propagation* 57.2, pp. 307–317.
- Webb, S. (1999). *Measuring the Universe: The Cosmological Distance Ladder*. Chichester, UK: Springer-Praxis Publishing Ltd.
- Wei, T. (2015). “A Convergence and Asymptotic Analysis of the Generalized Symmetric FastICA Algorithm”. In: *IEEE Transactions on Signal Processing* 63, pp. 6445–6458. DOI: [10.1109/TSP.2015.2468686](https://doi.org/10.1109/TSP.2015.2468686). arXiv: [1408.0145 \[stat.ML\]](https://arxiv.org/abs/1408.0145).
- White, M. (1998). “Remark on the estimation of angular power spectra in the presence of foregrounds”. In: 57, pp. 5273–5275. DOI: [10.1103/PhysRevD.57.5273](https://doi.org/10.1103/PhysRevD.57.5273). eprint: [astro-ph/9802211](https://arxiv.org/abs/astro-ph/9802211).
- Wijnholds, S. et al. (2010). “Calibration challenges for future radio telescopes”. In: *IEEE Signal Processing Magazine* 27, pp. 30–42. DOI: [10.1109/MSP.2009.934853](https://doi.org/10.1109/MSP.2009.934853). arXiv: [1004.0156 \[astro-ph.IM\]](https://arxiv.org/abs/1004.0156).
- Wijnholds, S. J. and A.-J. van der Veen (2008). “Fundamental Imaging Limits of Radio Telescope Arrays”. In: *IEEE Journal of Selected Topics in Signal Processing* 2, pp. 613–623. DOI: [10.1109/JSTSP.2008.2004216](https://doi.org/10.1109/JSTSP.2008.2004216). arXiv: [1003.2307 \[astro-ph.IM\]](https://arxiv.org/abs/1003.2307).
- Wolz, L. et al. (2014). “The effect of foreground subtraction on cosmological measurements from intensity mapping”. In: 441, pp. 3271–3283. DOI: [10.1093/mnras/stu792](https://doi.org/10.1093/mnras/stu792). arXiv: [1310.8144](https://arxiv.org/abs/1310.8144).
- Wolz, L. et al. (2015). “Foreground Subtraction in Intensity Mapping with the SKA”. In: *Advancing Astrophysics with the Square Kilometre Array (AASKA14)*, 35, p. 35. arXiv: [1501.03823](https://arxiv.org/abs/1501.03823).
- Wood, R. W. (1988). *Physical Optics*. Washington, D.C: Optical Society of America.

- Woodburn, L. et al. (2015). “Conversion of a New Zealand 30-Metre Telecommunications Antenna into a Radio Telescope”. In: 32, e017, e017. DOI: [10.1017/pasa.2015.13](https://doi.org/10.1017/pasa.2015.13). arXiv: [1407.3346 \[astro-ph.IM\]](https://arxiv.org/abs/1407.3346).
- Wu, J. et al. (2017). “MomentsNet: a simple learning-free method for binary image recognition”. In: *ArXiv e-prints*. arXiv: [1702.06767 \[cs.CV\]](https://arxiv.org/abs/1702.06767).
- Wyant, James C and Katherine Creath (1992). “Basic wavefront aberration theory for optical metrology”. In: *Applied optics and optical engineering* 11.part 2, pp. 28–39.
- Yap, P.-T., R. Paramesran, and S.-H. Ong (2003). “Image analysis by krawtchouk moments”. In: *IEEE Transactions on Image Processing* 12, pp. 1367–1377. DOI: [10.1109/TIP.2003.818019](https://doi.org/10.1109/TIP.2003.818019).
- Yap, Pew-Thian and Paramesran Raveendran (2005). “An Efficient Method for the Computation of Legendre Moments.” In: *IEEE Trans. Pattern Anal. Mach. Intell.* 27.12, 1996–2002. URL: <http://dblp.uni-trier.de/db/journals/pami/pami27.html#YapP05>.
- Yatawatta, S. (2008). “Subspace Techniques for Radio-Astronomical Data Enhancement”. In: *ArXiv e-prints*. arXiv: [0809.0208](https://arxiv.org/abs/0809.0208).
- Yatawatta, S. et al. (2013). “Initial deep LOFAR observations of epoch of reionization windows. I. The north celestial pole”. In: *A&A* 550, A136, A136. DOI: [10.1051/0004-6361/201220874](https://doi.org/10.1051/0004-6361/201220874). arXiv: [1301.1630 \[astro-ph.IM\]](https://arxiv.org/abs/1301.1630).
- Zhang, C., J. Wu, and W. Sun (2007). “Applications of Pseudo-Polar FFT in Synthetic Aperture Radiometer Imaging”. In: *Progress In Electromagnetics Research Symposium* 3.
- Zhang, D. and G. Lu (2004). “Review of shape representation and description techniques”. In: *Pattern Recognition* 37.
- Zhang, H. et al. (2010). “Blurred Image Recognition by Legendre Moment Invariants”. In: *IEEE Transactions on Image Processing* 19, pp. 596–611. DOI: [10.1109/TIP.2009.2036702](https://doi.org/10.1109/TIP.2009.2036702).

Appendix A

Appendix A

OSKAR BEAMPATTERN AND FOREGROUND SIMULATIONS

A.1 Ray Tracing Technique

This method of producing antenna response patterns in the geometric optics approximation was developed for the JVLA and Expanded Very Large Array (EVLA¹) of antennas by Brisken 2003 (cassbeam Software for cassegrain antenna modelling, National Radio Astronomy Observatory (NRAO²)). It is used to obtain the electric field on an evenly distributed grid points on the aperture plane through a complicated process. Some iterations are needed, since the ray may not propagate along the line of sight \hat{z} from the primary to the aperture plane. Initially, the (x, y) component of the grid point to be determined is taken as the reference point on the primary. The respective z value and the surface normal are then calculated for that point on the primary. The virtual ray is then reflected off the sub-reflector. Here, the sub-reflector is never stored as a raster surface rather, recalculated each time it is needed and this is by far more efficient than searching a tabulated surface for an intersection point. The sub-reflector displacement and rotation are then considered. A ray is then projected from the feed to this point on the sub-reflector. The procedure is now reversed such that a guess for the appropriate sub-reflector point is made. A ray is traced from the feed to this point on the sub-reflector, then reflects towards the primary and finally reflects to the aperture plane. The (x', y') value of the intersection of the ray with the aperture plane is compared with the initial (x, y) . An offset is applied to the initial value and the iteration continues. About 3 to

¹<http://www.aoc.nrao.edu/evla/>

²<https://public.nrao.edu/>

7 iterations are good enough for convergence. The final ray is defined once points on both the aperture plane and the primary are known. 3 rays are shot out from a small triangular region of the aperture plane and are used to calculate the flux through the point of interest on the aperture plane. This value includes the taper of the feed, the dilution of the beam due to expansion and the effects of all the surface shapings. The magnitude of the ray is then used to obtain the phase of the field on the aperture such that, the 2 circular polarisation vectors are propagated from the feed. Finally, the electric field decomposed into a linear polarisation basis for each outgoing circular polarisation calculated on the aperture plane grid.

A.2 Modelled and measured beams

The Mueller matrix representations in Fig. A.1 show the different perturbation methods (i.e. gain, phase and orientation of dipole errors) used to corrupt the OSKAR beam model. These perturbed beams are then compared with the errors produced from “real” measured beams of the JVLA in Fig. A.2.

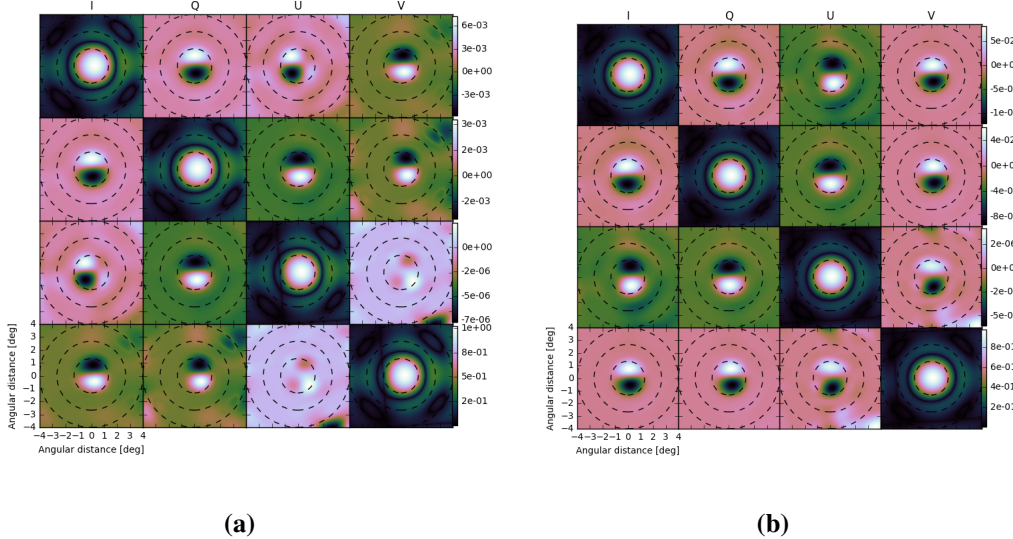


Figure A.1: Fully polarised distorted primary beams of KAT-7. (a) Due to gain and phase errors. (b) Due to dipole orientation errors.

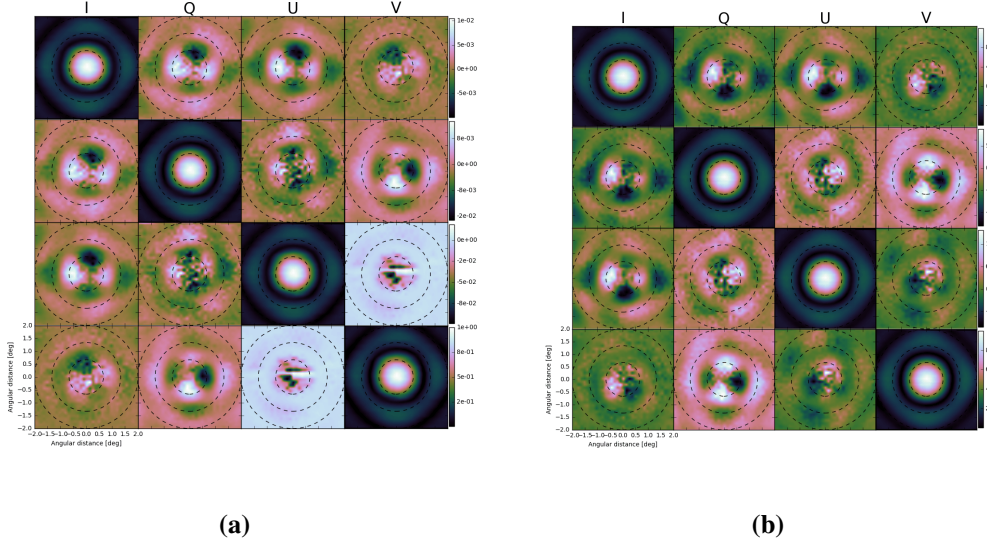


Figure A.2: 1 GHz holography measured Mueller beams of JVLA. (a) Antenna 5. (b) Antenna 6.

A.3 Measured Full-sky maps

Fig. A.3 displays the complete corrupted convolved maps generated from simulating the foregrounds in Fig. 4.5 with perturbed model beams (due gain and phase errors) in Fig. A.1a.

Figs. A.4 and A.5 represent the respective full-sky convolved maps simulated with the modelled beams (using uncorrupted and dipole orientation error beams) and holography measured beams of JVLA in Fig. A.2.

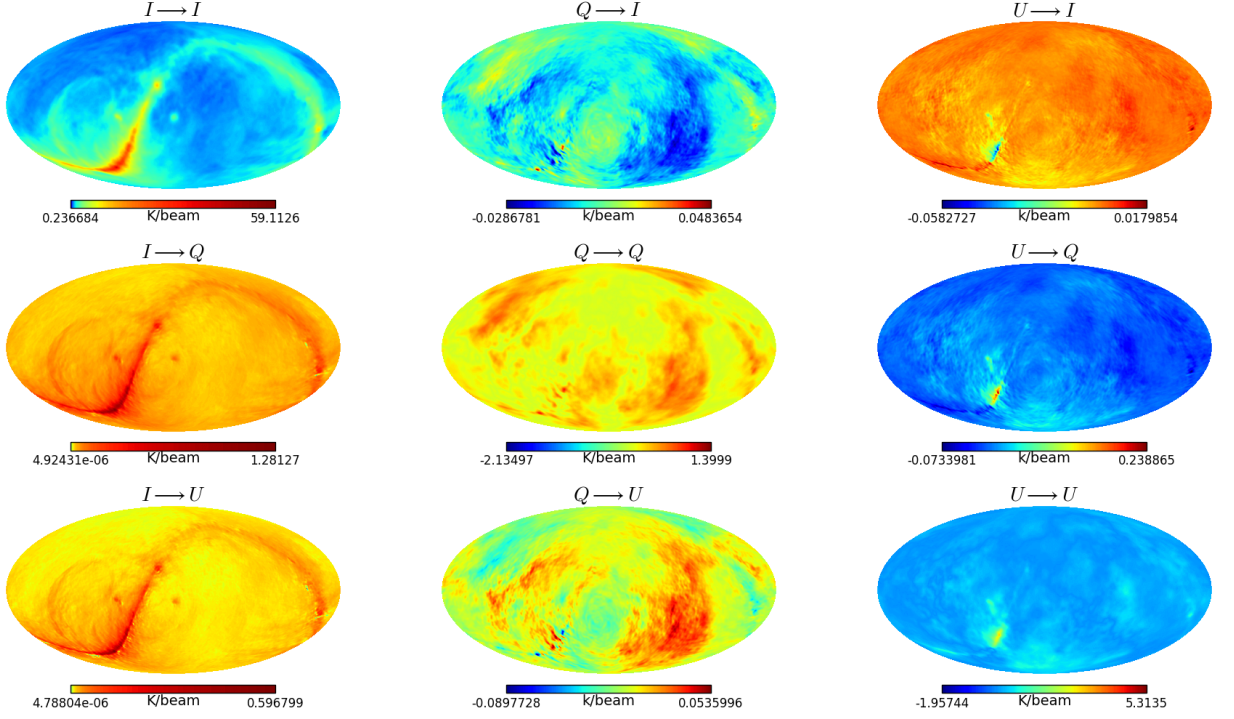
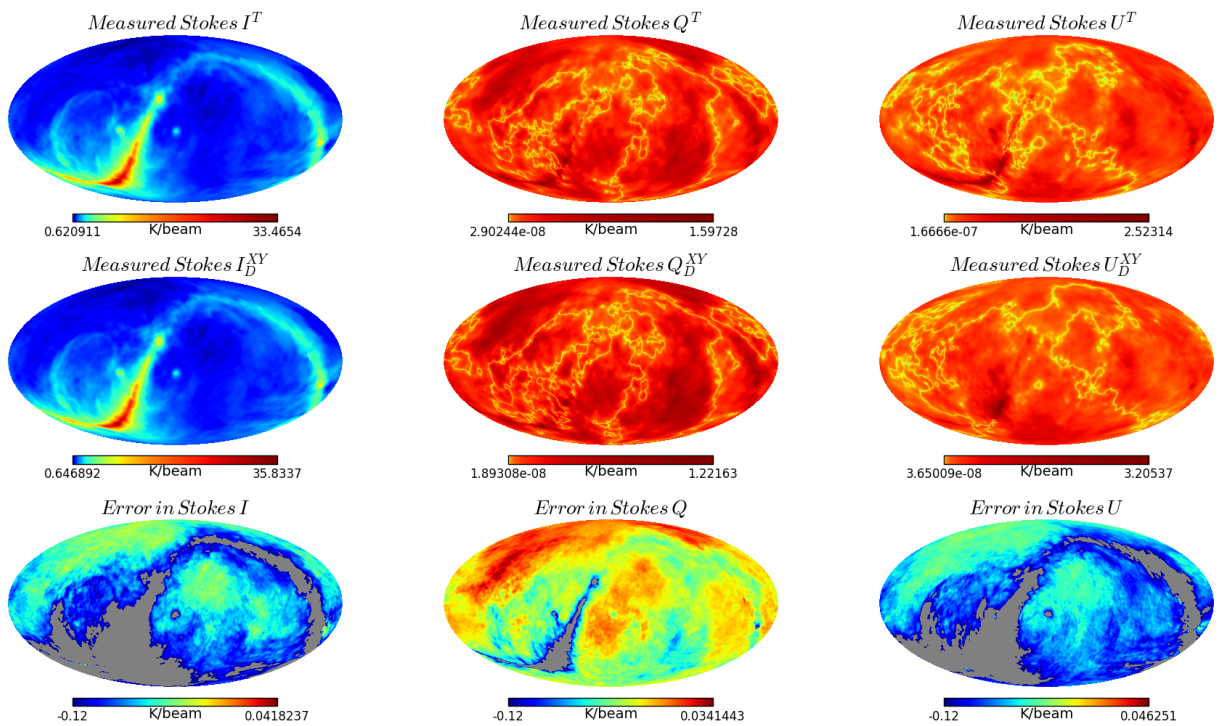


Figure A.3: Convolved full-sky polarisation maps using the corrupted primary beams in Fig. A.1a. Here also, we used the m_{II} beam in Fig. A.1a to convolve Stokes I in Fig. 4.5 and produce the convolved map $I \rightarrow I$, then we used m_{QI} beam to convolve Stokes Q to obtain the convolved map $Q \rightarrow I$, also, using the m_{UI} beam to convolve Stokes U we produce the convolved map $U \rightarrow I$. The same approach is repeated to obtain (in row 2) $I \rightarrow Q, Q \rightarrow Q, Q \rightarrow U$ and (in row 3) $I \rightarrow U, Q \rightarrow U, U \rightarrow U$ by using the corresponding beams m_{IQ}, m_{QQ}, m_{UQ} and m_{IU}, m_{QU}, m_{UU} .

Table A.1: Error introduced in the power spectrum estimation

	1.3							
	<i>I</i>		<i>Q</i>		<i>U</i>		<i>TOTAL</i>	
	<i>GP</i> [%]	<i>XY</i> [%]						
<i>I</i>	0.0640	0.0640	0.0151	0.0137	0.0050	0.0045	0.0841	0.0822
<i>Q</i>	0.0010	0.0008	0.0221	0.0224	0.0007	0.0055	0.0238	0.0287
<i>U</i>	0.0007	0.0007	0.0194	0.0341	0.0354	0.0362	0.0555	0.0710

**Figure A.4:** Measured Stokes I , Q and U for using non-distorted and distorted dipole orientation error OSKAR beams with corresponding errors terms.**Figure A.5:** Measured Stokes I , Q and U for holography measured beams of JVLA with corresponding errors terms.

A.4 Error Estimation in the Power Spectrum

Table A.1 displays the errors recorded in the angular power spectrum estimation when modelled beams are assumed, whilst the foregrounds are actually convolved with real measured beams. These errors are tabulated from the absolute differences of the standard errors reported in Fig. 4.7.

Appendix B

Zernike Polynomials Model

B.1 Settings for OSKAR applications

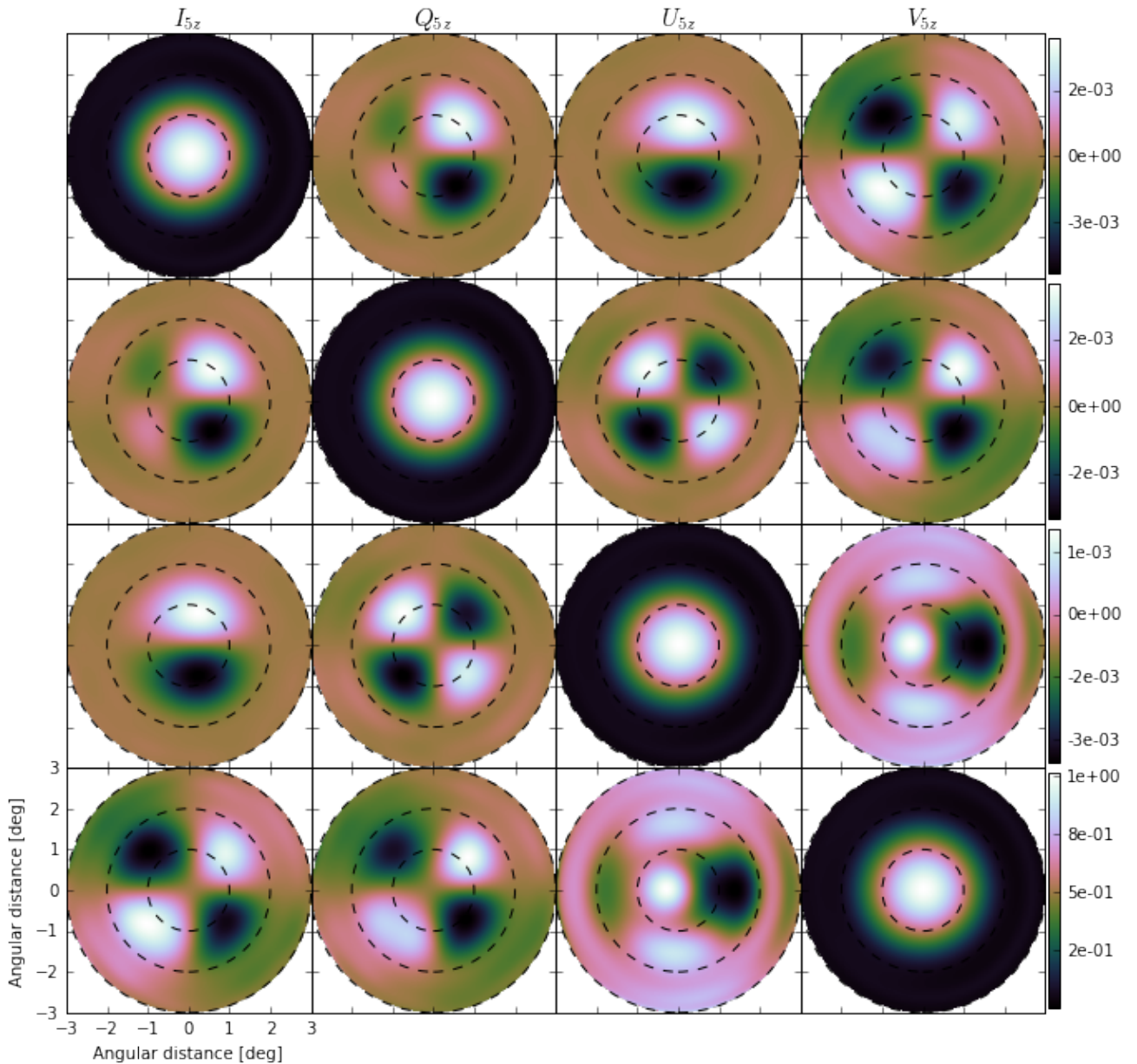


Figure B.1: Measured Stokes I , Q and U for using non-distorted and distorted dipole orientation error OSKAR beams with corresponding errors terms.

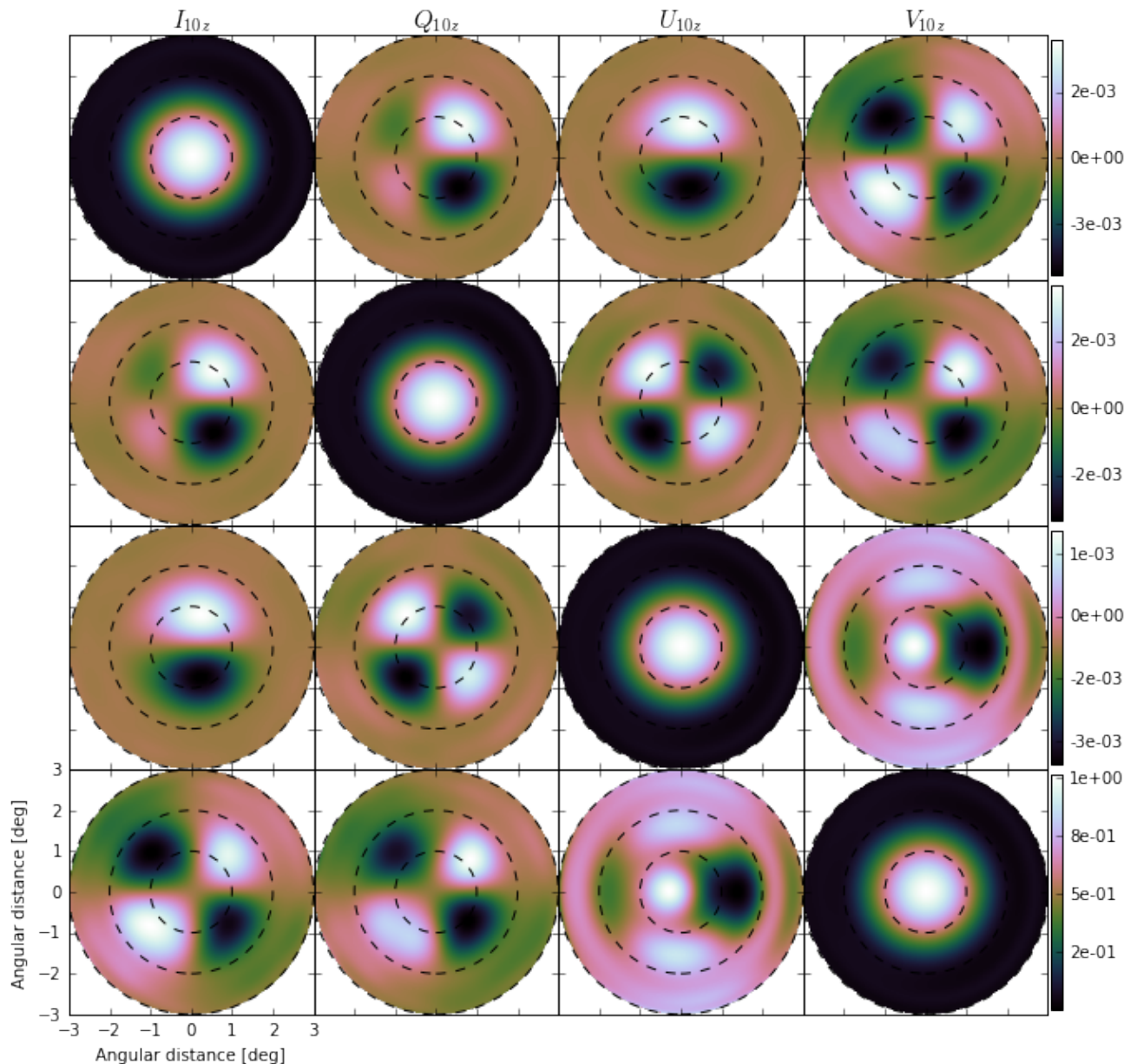


Figure B.2: Measured Stokes I , Q and U for using non-distorted and distorted dipole orientation error OSKAR beams with corresponding errors terms.

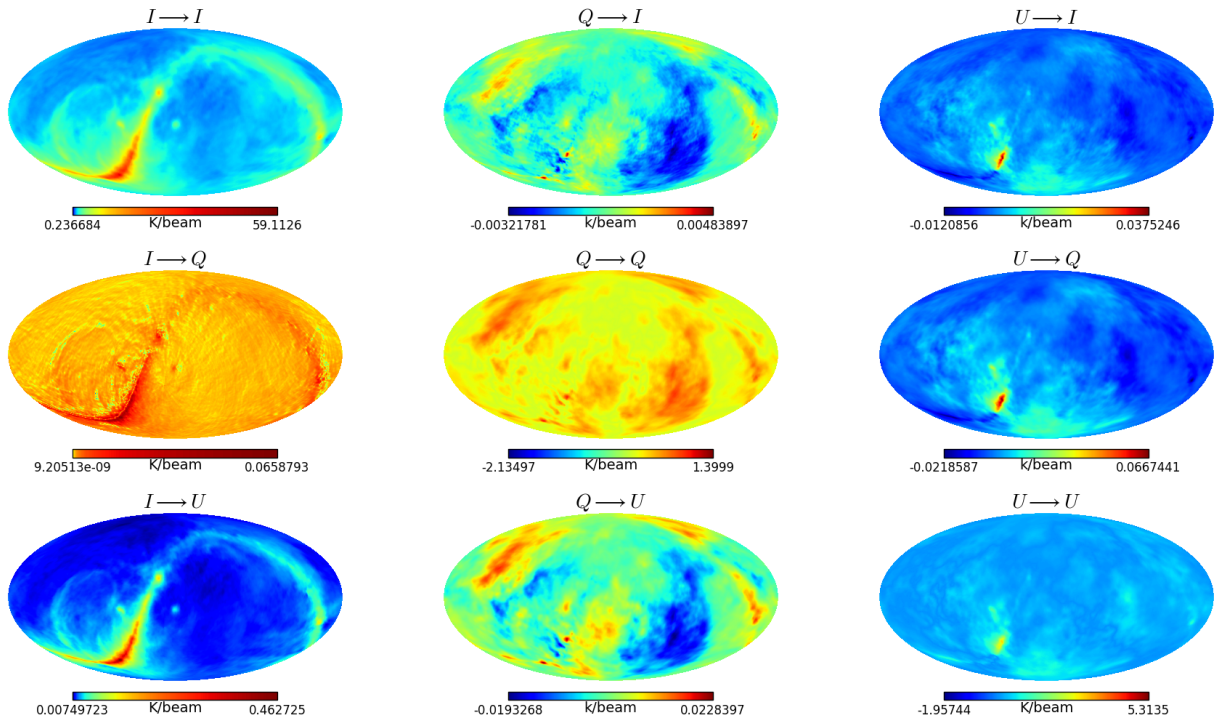


Figure B.3: Measured Stokes I , Q and U for using non-distorted and distorted dipole orientation error OSKAR beams with corresponding errors terms.